NASA/TM-2012-104606/Vol 30

Technical Report Series on Global Modeling and Data Assimilation, Volume 30

Max J. Suarez, Editor

The GEOS-iODAS: Description and Evaluation

Guillaume Vernieres, Michele M. Rienecker, Robin Kovach, and Christian L. Keppenne

National Aeronautics and
Space Administration

Goddard Space Flight Center
Greenbelt, Maryland 20771

December 2012

NASA STI Program ... in Profile

Since its founding, NASA has been dedicated to the advancement of aeronautics and space science. The NASA scientific and technical information (STI) program plays a key part in helping NASA maintain this important role.

The NASA STI program operates under the auspices of the Agency Chief Information Officer. It collects, organizes, provides for archiving, and disseminates NASA's STI. The NASA STI program provides access to the NASA Aeronautics and Space Database and its public interface, the NASA Technical Report Server, thus providing one of the largest collections of aeronautical and space science STI in the world. Results are published in both non-NASA channels and by NASA in the NASA STI Report Series, which includes the following report types:

- TECHNICAL PUBLICATION. Reports of completed research or a major significant phase of research that present the results of NASA Programs and include extensive data or theoretical analysis. Includes compilations of significant scientific and technical data and information deemed to be of continuing reference value. NASA counterpart of peer-reviewed formal professional papers but has less stringent limitations on manuscript length and extent of graphic presentations.
- TECHNICAL MEMORANDUM. Scientific and technical findings that are preliminary or of specialized interest, e.g., quick release reports, working papers, and bibliographies that contain minimal annotation. Does not contain extensive analysis.
- CONTRACTOR REPORT. Scientific and technical findings by NASA-sponsored contractors and grantees.
- CONFERENCE PUBLICATION. Collected papers from scientific and technical conferences, symposia, seminars, or other meetings sponsored or co-sponsored by NASA.
- SPECIAL PUBLICATION. Scientific, technical, or historical information from NASA programs, projects, and missions, often concerned with subjects having substantial public interest.
- TECHNICAL TRANSLATION. English-language translations of foreign scientific and technical material pertinent to NASA's mission.

Specialized services also include organizing and publishing research results, distributing specialized research announcements and feeds, providing help desk and personal search support, and enabling data exchange services. For more information about the NASA STI program, see the following:

- Access the NASA STI program home page at http://www.sti.nasa.gov
- E-mail your question via the Internet to help@sti.nasa.gov
- Fax your question to the NASA STI Help Desk at 443-757-5803
- Phone the NASA STI Help Desk at 443-757-5802
- Write to:

  NASA STI Help Desk
  NASA Center for AeroSpace Information
  7115 Standard Drive
  Hanover, MD 21076-1320

NASA/TM-2012-104606/Vol 30

Technical Report Series on Global Modeling and Data Assimilation, Volume 30

Max J. Suarez, Editor

The GEOS-iODAS: Description and Evaluation

Guillaume Vernieres
Science Systems and Applications, Inc., Greenbelt, Maryland

Michele M. Rienecker
Goddard Space Flight Center, Greenbelt, Maryland

Robin Kovach
Science Systems and Applications, Inc., Greenbelt, Maryland

Christian L. Keppenne
Science Systems and Applications, Inc., Greenbelt, Maryland

National Aeronautics and
Space Administration

Goddard Space Flight Center
Greenbelt, Maryland 20771

December 2012

Level of Review: This material has been technically reviewed by technical management.

Available from:
NASA Center for AeroSpace Information
7115 Standard Drive
Hanover, MD 21076-1320

National Technical Information Service
5285 Port Royal Road
Springfield, VA 22161 Price Code: A17

Abstract

This report documents the GMAO's Goddard Earth Observing System sea ice and ocean data assimilation systems (GEOS iODAS) and their evolution from the first reanalysis test, through the implementation that was used to initialize the GMAO decadal forecasts, and to the current system that is used to initialize the GMAO seasonal forecasts. The iODAS assimilates a wide range of observations into the ocean and sea ice components: in-situ temperature and salinity profiles, sea level anomalies from satellite altimetry, analyzed SST, and sea-ice concentration. The climatological sea surface salinity is used to constrain the surface salinity prior to the Argo years. Climatological temperature and salinity gridded data sets from the 2009 version of the World Ocean Atlas (WOA09) are used to help constrain the analysis in data sparse areas. The latest analysis, GEOS ODAS5.2, is diagnosed through detailed studies of the statistics of the innovations and analysis departures, comparisons with independent data, and integrated values such as volume transport. Finally, the climatologies of temperature and salinity fields from the Argo era, 2002-2011, are presented and compared with the WOA09.

Table of Contents

List of Figures

1 Introduction

The Goddard Earth Observing System integrated Ocean Data Assimilation System (GEOS iODAS) described in this document is a system for both ocean and sea-ice data assimilation. It is integrated within the broader GEOS model and data assimilation system using the Earth System Modeling Framework (ESMF). By using an object-oriented framework, the analysis systems are model-independent, but have been implemented and tuned for the Modular Ocean Model Version 4.1 (MOM4.1) developed by the NOAA Geophysical Fluid Dynamics Laboratory (GFDL) and the CICE model developed by Los Alamos National Laboratory.

The primary performance driver of the GEOS iODAS products (fields of temperature, salinity, currents, sea surface height, sea ice thickness and concentration) is the initialization of short-term climate forecasts. However, the analyses should also be climate-quality to support studies of climate variability and to serve as the ocean component of an Integrated Earth System Analysis (IESA). Since climate forecasts require hindcasts for forecast calibration, a byproduct of the ocean and sea-ice reanalysis is a retrospective estimate of the state of the ocean and sea-ice, and of the atmosphere when the analysis is conducted in the GEOS coupled atmosphere ocean general circulation model (AOGCM).

Satellites provide measurements of the ocean surface or an integrated column, not profiles as for the atmosphere. For altimeter data in particular, full use of the data requires the assimilation to interpret the signal as temperature, salinity and current signals below the surface. Until the advent of Argo floats early this century, most of the in-situ ocean data have been limited to temperature profiles. In order to maintain the ocean's water masses in the analysis, salinity corrections have to accompany temperature corrections. Thus most of the system development has been directed towards multivariate covariance modeling. The approach has been to rely on the statistics from ensembles, either static (ensemble optimal interpolation: EnOI) or dynamic (Ensemble Kalman Filter: EnKF), or a hybrid of static and dynamic covariances for the background covariances.

Since the role of data assimilation is to find a compromise between the simplified representation of the model physics and observations prone to instrumental errors and biases, the estimated state is only optimum relative to the *a priori* hypothesis of model and observation errors. This report describes the parameters chosen during the evolution of the system through four implementations (GEOS ODAS4.0, ODAS5.0, ODAS5.1 and ODAS5.2) as we tested and evaluated the system in preparation for climate forecasts. Due to the lack of independent validating data, the sparsity of data prior to the altimeter period and completion of the Tropical Atmosphere Ocean/Triangle Trans-Ocean Buoy Network (TAO/TRITON) moored buoy array, and because evaluation of system performance by comparing with other ocean assimilation systems required long time series, each of these implementations was used for a reanalysis of the historical data.

The report is organized as follows, section 2 describes the dynamical models used for the assimilation, section 3 presents the observations used in the assimilation, and section 4 describes aspects of the data assimilation methodology used. Section 5 discusses the assimilation set-up and its evolution, including parameters used for background and observations errors. Section 6 presents diagnostics and results of the latest analyses, GEOS ODAS5.2. The report also includes a presentation of the climatologies of several fields over the more recent Argo period, 2002-2011.

2 The GEOS-5 Coupled Model

The model used in this report has two configurations, differing from one another only by the inclusion or exclusion of the atmospheric component, the Goddard Earth Observing System Model, Version 5 (GEOS-5) Atmospheric General Circulation Model (AGCM).

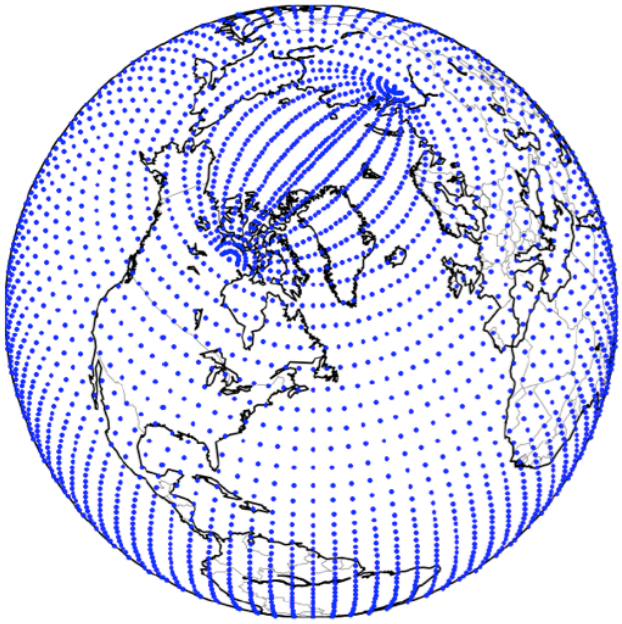

Figure 1: Northern Hemisphere view of the ocean tripolar grid. The blue dots indicate the center of the grid cell.

Configuration 1 (CM1) is a fully coupled model that integrates the Fortuna version of the GEOS-5 AGCM with the Catchment land surface model (LSM) (Rienecker et al. 2008; Molod et al. 2012), the Modular Ocean Model version 4 (MOM4, Griffies et al. 2005) and the CICE sea ice model (Hunke and Lipscomb 2008). A skin layer interface serves as a coupler between the ocean and atmosphere and mediates the exchange of momentum, heat and fresh water at every time step. The skin layer includes the parameterization of the diurnal cycle in the near-surface ocean, and the thermodynamics of CICE. The atmospheric component includes a river runoff routing scheme. All components are coupled together using ESMF and use the atmospheric time step for the coupling interval.

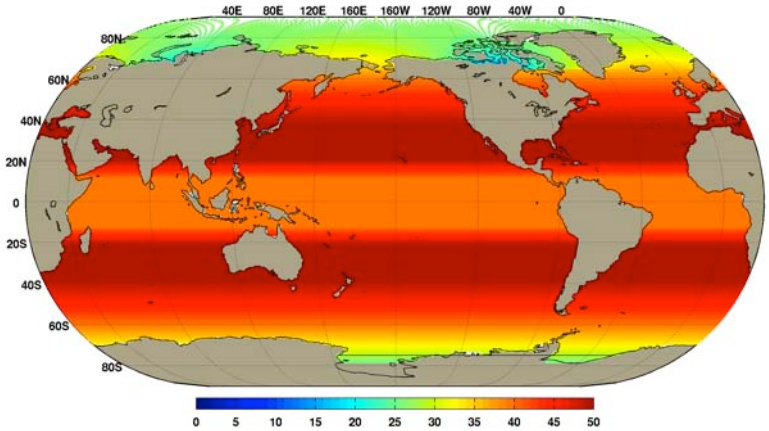

Figure 2: Ocean grid resolution (km), represented as the square root of the cell area.

For the assimilation experiments reported here, the atmospheric model uses a Cartesian grid with a 1° × 1.25° horizontal resolution and 72 hybrid vertical levels with the upper most level at 0.01 hPa. The nominal resolution of the ocean grid is ½°, with a meridional equatorial refinement to ¼°. It is a regular Cartesian grid south of 65°N, and curvilinear north of 65°N, with two poles

located on land to eliminate the problem of vanishing cell area at the geographic North Pole (Figure 1). The resolution of the resulting tripolar grid is depicted in Figure 2, which shows the square root of cell areas in units of kilometers, with a minimum and maximum resolution of 15 km and 52 km, respectively. The ocean topography, shown in Figure 3, is derived from the ETOPO5 data set.

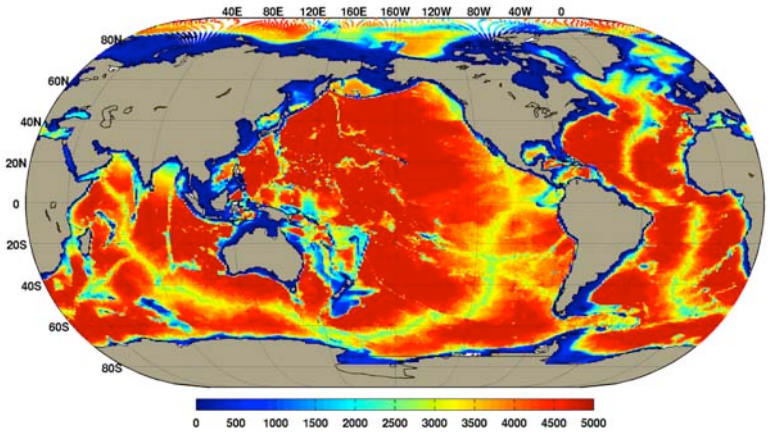

Figure 3: Ocean grid topography (m).

The CM1 framework has been used in support of the decadal prediction activities under the Coupled Model Intercomparison Project Phase 5 (CMIP5; Ham et al. 2012) as well as the GMAO seasonal forecasts that are contributed to the National Multi-Model Ensemble (NMME) project.

The second configuration (CM2) is similar to CM1, except that the data-atmosphere module of GEOS-5 is used so that surface forcing from the atmosphere is prescribed. The skin layer is provided with specified hourly fields of:

- 10-meter air temperature
- 10-meter specific humidity
- 10-meter winds
- Sea level pressure
- Surface absorbed long-wave radiation
- Surface incoming short-wave flux
- Precipitation (rain and snow)
- River run-off.

To couple the ocean and sea ice component of GEOS-5 with a realistic AGCM, a method in which the AGCM is constrained to GMAO's Modern-Era Retrospective Analysis for Research and Application (MERRA; Rienecker et al. 2011) is used. It consists of replacing some of the variables of the AGCM with the background fields from MERRA. The fields that are replaced every six hours consist of:

- Surface pressure
- Pressure thickness
- Zonal and meridional winds
- Specific humidity
- Ozone concentration
- Potential temperature

- Dry temperature.

3 The Observations

The evolution of the ocean observing system from 1950 to the present, as used in the GEOS iODAS, is depicted in Figure 4. Data assimilated consist of the following:

- Sea surface temperature (SST)
  - Reynolds (Reynolds et al. 2007) from 1982 to present,
  - CMIP5 SST (Hurrell et al. 2008) prior to 1982.
- Temperature (*T*) and salinity (*S*) profiles from
  - eXpendable Bathythermographs (XBTs) and Conductivity Temperature Depth (CTD) sensors extracted from the EN3 data base (Ingleby and Huddleston 2007) with time-varying XBT corrections applied according to Levitus et al. (2009),
  - the tropical moored buoy array (McPhaden et al. 2010) - TAO/TRITON, PIRATA, and RAMA arrays,
  - Argo, with profiles from the Argo Global Data Assembly Center (GDAC, see http://www.usgodae.org/argo/argo.html).
- Along-track sea level anomalies (SLA) from the Archiving, Validation and Interpretation of Satellite Oceanographic (AVISO) merged product from 1993 onwards.

The World Ocean Atlas 2009 (WOA09) gridded climatology (Antonov et al. 2010; Locarnini et al. 2010) is also used to correct some of the model's biases, particularly prior to the Argo era.

The ice component of the iODAS assimilates sea-ice concentration from the National Snow and Ice Data Center (NSIDC) from 1979 onwards and the CMIP5 sea ice concentration prior to 1979. The NSIDC product is based on passive microwave observations of ice concentration from the Nimbus-7 Scanning Multi-channel Microwave Radiometer (SMMR) and the Defense Meteorological Satellite Program (DMSP) Special Scanning Microwave Imager (SSM/I) and Special Scanning Microwave Imager/Sounder (SSMI/S). The products have a 25 km spatial resolution for both the north and south polar regions. Temporal resolution is every other day from October 1978 to July 1987 (SMMR), then daily from August 1987 to present (SSM/I). Ice concentrations from CMIP5 and Reynolds are used in areas that are not measured due to orbit inclination (poleward of 87.2° for SSM/I and 84.5° for SMMR).

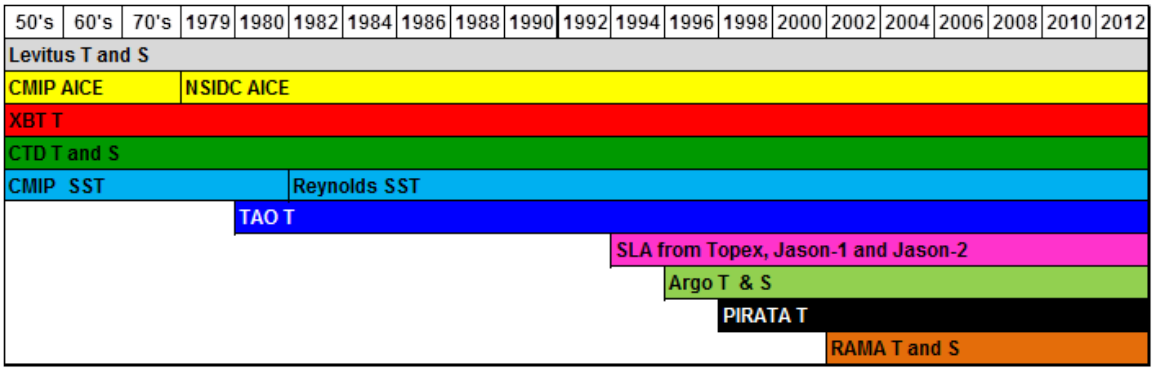

Figure 4: Evolution of the ocean observing system used in the iODAS.

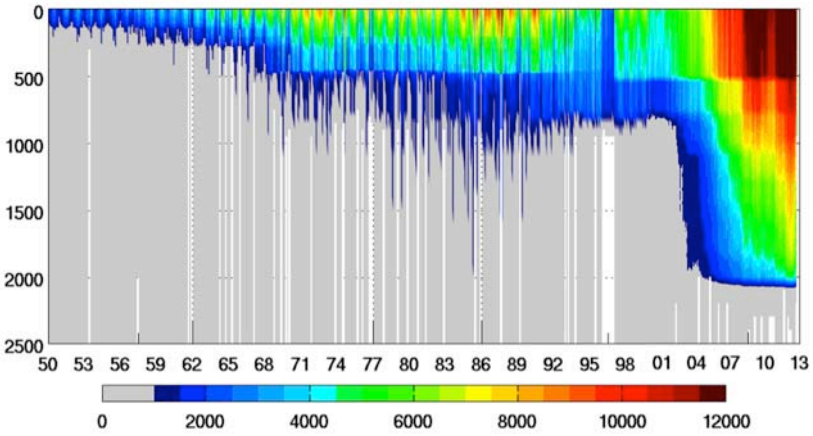

Figure 5: Time series of the number of in-situ temperature profiles per month as a function of depth.

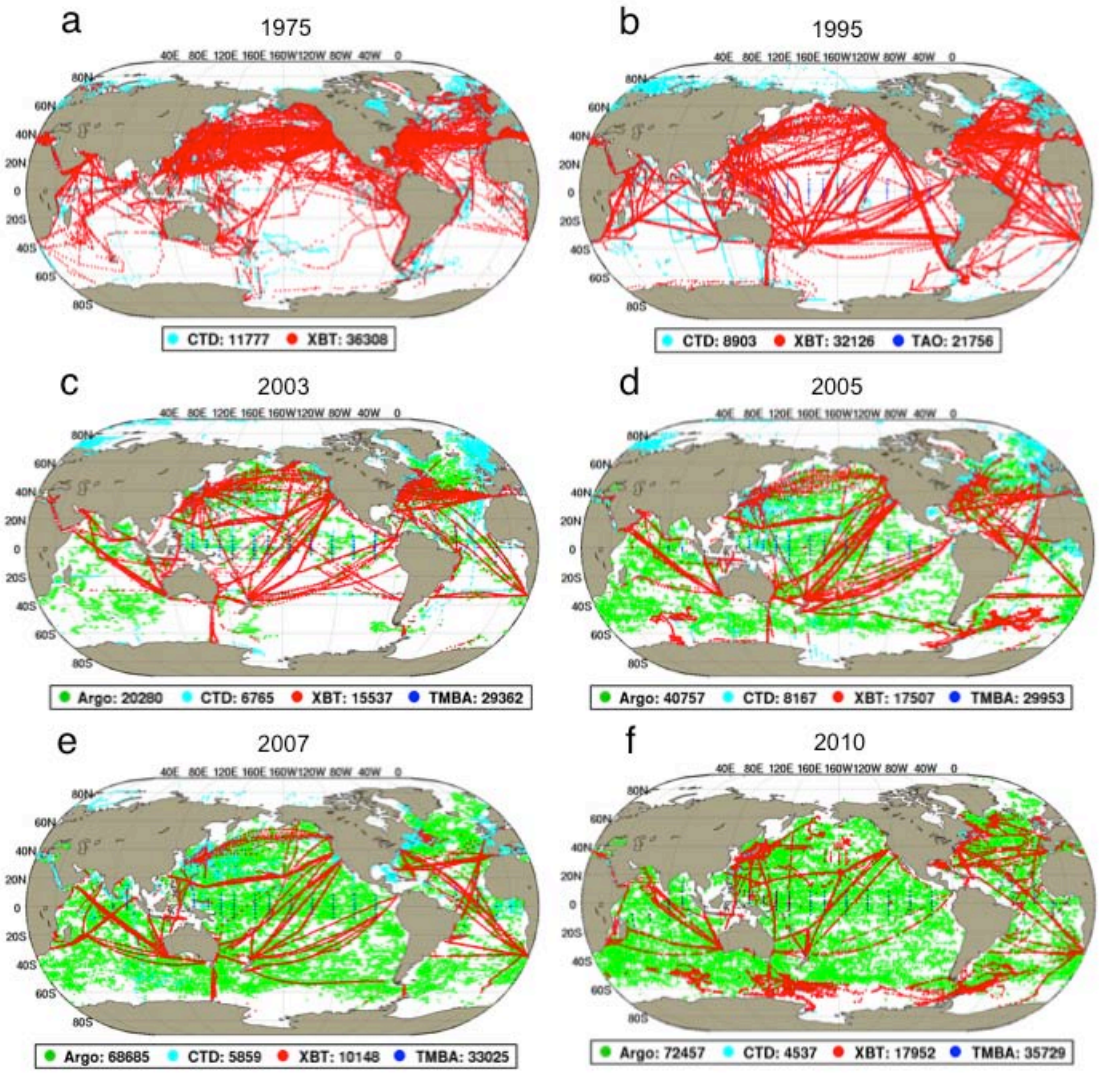

Figure 6: The horizontal distribution of in-situ observations in (a) 1975, (b) 1995, (c) 2003, (d) 2005, (e) 2007, and (f) 2010.

While the near-surface ocean temperature is relatively well observed during the period of interest, that at depth is not. This can be seen in Figure 5, which shows the evolution of the observing system for temperature from 1950 to present. While Figure 5 illustrates a significant increase in profiles to 2000 m from 2003 onwards because of Argo, Figure 6 shows that the horizontal coverage becomes global only from about 2005 onwards. These changes in the observing system can result in large changes in the analysis biases, impacting inferred climate variability. In order to alleviate some of these artifacts, the WOA09 climatology is assimilated to constrain the unobserved ocean towards realistic values.

4 The Data Assimilation Methodology

Data assimilation refers to optimization methods that seek the true state of a system by optimally combining observations with a physical representation of that system. For all methods used in this report, the analysis can be expressed as a linear regression in observation space:

$$\boldsymbol{x^a} = \boldsymbol{x^f} + \sum_{i=1}^{N_o} \beta_i \boldsymbol{r}_i, \tag{4.1}$$

where $\boldsymbol{x^a}$ is the analysis, $\boldsymbol{x^f}$ is the forecast or prior state, the $\boldsymbol{r_i}$ are covariances between the state and the observations, also referred to as the representers (Kimeldorf and Wahba 1970; Bennett 1992), N_o is the number of observations and the β_i are the representer coefficients. The β_i are determined by solving linear system

$$\left(\boldsymbol{HPH^T} + \boldsymbol{R}\right)\boldsymbol{\beta} = \boldsymbol{y} - \boldsymbol{Hx_f} = \boldsymbol{h}, \tag{4.2}$$

where $\boldsymbol{H}$ is a linear observation operator, the i-th column of $\boldsymbol{PH^T}$ is the i-th representer $\boldsymbol{r_i}$, $\boldsymbol{y}$ is the vector containing the N_o observations, $\boldsymbol{R}$ is an observation error-covariance matrix, and $\boldsymbol{h}$ is the model-data misfit.

The iODAS is a sequential ensemble assimilation software system that includes a wide range of algorithm implementations, from simple optimal interpolation (OI: Eliassen 1954) to more expensive ensemble methods such as ensemble Kalman filtering or particle filtering. The reanalysis applications presented here use the ensemble optimal interpolation (e.g., Oke et al. 2010, Wan et al. 2010) implementation where the time dependency of the covariances is neglected and $\boldsymbol{P}$ is estimated from the statistics of model run histories or from combinations of model histories. EnOI methods are often competitive with the EnKF because they make up for the performance degradation due to neglecting the forecast-error evolution by computing their statistics from a much larger ensemble. Keppenne et al. (2013) introduces an additional approach to estimating the background error covariances – the spatial approximation of forecast errors (SAFE) technique. This approach is used in the GEOS ODAS for the assimilation of surface observations such as SST and sea surface salinity (SSS) (see Table 1 below).

4.1 Covariance modeling and localization

In the Optimal Interpolation implementation, the covariances are assumed to have a Gaussian shape, approximated by the function given by $\tilde{C}_0(\tilde{z}) = C_0\left(\tilde{z}, \frac{1}{2}, \frac{1}{2}\right)$ as a special case of equation (4.10) of Gaspari and Cohn (1999). Dependencies on the background flow are obtained through the application of a localization function that uses Euclidean distance in *T, S* and density space. For example, a continuous form of the i-th representer can be written as

$$\boldsymbol{r}_i(x,y,z,t) = \lambda\alpha_i C_0\left(max\left\{\frac{|x_i - x|}{L_x} + \frac{|y_i - y|}{L_y} + \frac{|z_i - z|}{L_z}, \frac{|v_i - v|}{L_v}\right\}\right) C_0\left(\frac{|t_i - t|}{L_t}\right) C_0\left(\frac{|\varphi_i - \varphi|}{L_\varphi}\right), \tag{4.3}$$

where $\left(x_i, y_i, z_i, t_i\right)$ is the space-time position of an observation, α_i is an estimate of the background-error variance at the location of the observation, v is *T*, *S* or density, and L_x etc. are

the vanishing-correlation length scales. The parameter λ is an inflation factor that is determined by

$$\lambda = \gamma^2 \frac{\|diag(\boldsymbol{R})\|}{\|diag(\boldsymbol{HPH}^T)\|}, \tag{4.4}$$

where γ is prescribed and represents the target ratio of background error standard deviation to observational error standard deviation and where $\| \|$ represents the L_2 vector norm. Finally, φ is a smooth, horizontally varying field that imposes the constraint that a representer does not cross major land boundaries; for example, a representer corresponding to an observation in the Gulf of Mexico will not influence the western Pacific.

The SAFE implementation is similar to OI, except that the amplitude α_i of the Gaussian covariances in (4.3) and cross-covariances are estimated from the model state itself. The approach is outlined here. A more complete description can be found in Keppenne et al. (2013).

For simplicity of notation, the model state is split according as $\boldsymbol{x} = [\boldsymbol{v}, \boldsymbol{w}]$, where $\boldsymbol{v}$ is an observed model field and $\boldsymbol{w}$ is unobserved. The background error covariances are

$$\boldsymbol{P} = \begin{bmatrix} \boldsymbol{P^{vv}} & \boldsymbol{P^{vw}} \\ \boldsymbol{P^{wv}} & \boldsymbol{P^{ww}} \end{bmatrix}.$$

Then the analysis state update is split according to

$$\boldsymbol{v}^a = \boldsymbol{v}^f + \Delta\boldsymbol{v} = \boldsymbol{v}^f + \boldsymbol{P}^{vv}\boldsymbol{H}^T[\boldsymbol{H}\boldsymbol{P}^{vv}\boldsymbol{H}^T + \boldsymbol{R}]^{-1}\left[\boldsymbol{y} - \boldsymbol{H}\left(\boldsymbol{v}^f\right)\right], \tag{4.5a}$$

$$w_{ijk}^a = w_{ijk}^f + \frac{P_{ijk}^{wv}}{P_{ijk}^{vv}}\Delta v, i = 1, \ldots, I; j = 1, \ldots, J; k = 1, \ldots, K, \tag{4.5b}$$

where I, J and K denote the number of grid cells along the x, y, and z space dimensions, respectively.

The first step is to estimate the background-error variance of the observed field with

$$\boldsymbol{\sigma}_{vv}^2 = diag(\boldsymbol{P^{vv}}) = \Theta([\boldsymbol{v} - \Theta(\boldsymbol{v})]^{\boldsymbol{2}}), \tag{4.6}$$

where Θ is a 3D local averaging operator. The iODAS implementations presented here used Gaussian smoothing, which was found to give better results than simple averaging with uniform weights. The size of the regions over which the Θ smoothing operator is applied is of little consequence, except close to continental boundaries (Keppenne et al. 2013). The variance estimate is rescaled such that $\lambda = 1$ in (4.4).

The covariance, ω_{12}, of the background errors for $\boldsymbol{v}$ at locations (x_1, y_1, z_1) and (x_2, y_2, z_2) is estimated as

$$\omega_{12} = \sigma_{v_1 v_1}\sigma_{v_2 v_2} C_0 \left(max \left\{ \frac{|x_1 - x_2|}{L_x} + \frac{|y_1 - y_2|}{L_y} + \frac{|z_1 - z_2|}{L_z}, \frac{|v_1 - v_2|}{L_v} \right\} \right).$$

This formula ensures that ω_{12} is 0 if either v_1 differs significantly from v_2 or the locations are very distant from each other. After estimating the background error variances and covariances, the update (4.5a) is applied.

To update the unobserved variable, the local cross-field background error covariances of $\boldsymbol{v}$ and $\boldsymbol{w}$ in every grid cell are estimated as

$$\sigma_{vw}^2 = \Theta([\boldsymbol{v} - \Theta(\boldsymbol{v})][\boldsymbol{w} - \Theta(\boldsymbol{w})].$$

The fields of unobserved variables are then updated according to equation (4.5b).

Unlike the SAFE or OI, the EnOI uses covariances estimated from an ensemble of model states. Spurious long-range covariances are filtered using localization in space, while dependencies on the background flow are obtained in the same manner as the OI method.

The ocean and sea-ice analyses presented here from ODAS4.0 and ODAS5.0 used the EnOI while ODAS5.1 and ODAS5.2 used a configuration that combines OI, SAFE and EnOI.

5 System Evolution

5.1 GEOS ODAS4.0

The ocean retrospective analysis using GEOS ODAS4.0 spans 52 years from 1960 to 2011. The reanalysis used the CM1 model framework described in Section 2 and the EnOI method to assimilate ocean and sea-ice observations while the atmosphere was constrained to MERRA. Prior to the Argo period, the model biases were corrected by assimilating 10% of the climatological profiles of temperature and salinity, randomly selected, from WOA09 every 10 days.

The ensemble used for estimating the background error covariances consisted of the 20 leading empirical orthogonal functions (EOFs) of an ensemble of 900 ocean states. To generate the ensemble, a 20-member ensemble of freely running GEOS-5 coupled simulations was integrated over a period of 3 years. Each ensemble member was started from the same initial condition with a perturbation proportional to the vertical gradient of the local T and S added to the initial condition for T and S, respectively. The spread (measured by total variance) across this ensemble saturated after about 420 days. After this spin up period, snapshots of the deviation of the ensemble about the mean were saved every 15 days and stored in a “super ensemble” of 900 members. The 20 leading EOFs of this super ensemble were used to represent the background error covariances.

This version of the analysis contributed to the Xue et al. (2012) study that compared upper ocean heat content from several analyses and used the ensemble of analyses to estimate the uncertainty in climate signals in the recent decades. GEOS ODAS4.0 products are available online at http://dp6.nccs.nasa.gov/las/getUI.do.

5.2 GEOS ODAS5.0

The GEOS ODAS5.0 analysis used the same CM1 framework as GEOS ODAS4.0, except that the observation errors were increased substantially. This was done because of some unrealistic features that were occasionally found in the tropical Atlantic in the earlier analysis. The ODAS5.0 used the same ensemble for the EnOI as was used for ODAS4.0. The analysis was conducted in three different streams, each spun up for at least two years and started from the WOA09 climatology. Stream 1 covered December 1959 to December 1980; stream 2 covered January 1981 to December 1997; and stream 3 covered January 1998 to December 2011, at which point it was discontinued. This version of the analysis was used to initialize the GEOS-5 decadal predictions of Ham et al. (2012).

5.3 GEOS ODAS5.1 and ODAS5.2

One of the purposes of the GEOS ODAS5.1 and ODAS5.2 ocean and sea-ice analyses is to provide consistent initial conditions for all the model components present in the CM1 framework as an initialization of seasonal hindcasts and forecasts with GEOS-5, from 1980 to present. CM1, replaying MERRA and assimilating SST, SSS and sea-ice observations, was used to provide all initial conditions except for the ocean. Because of discrepancies in the climatology of the hydrological cycle in MERRA (Reichle et al. 2011), a correction to the MERRA precipitation fields was applied during the replay. The correction is based on the v2.1 product from the Global

Precipitation and Climatology Project (GPCP) prior to September 2009 and the Climate Prediction Center (CPC) Merged Analysis of Precipitation (CMAP), rescaled to be consistent with the GPCP climatology, from September 2009 to the present.

GEOS ODAS5.2 differs from ODAS5.1 in several ways: along-track altimeter data were assimilated and *no climatological profiles of T and S were assimilated during the Argo period.* ODAS5.2 was started at the beginning of the altimeter period in January 1993 from initial conditions provided by ODAS5.1. Due to time constraints, the assimilation of all ocean observations except sea-ice concentration was performed within the CM2 framework, forced with atmospheric fluxes obtained from the CM1 simulations. For ODAS5.1, the fluxes were obtained from the CM1 run described above, replaying MERRA but with a correction to the precipitation, assimilating SST, sea-ice concentration and SSS climatology. Unfortunately, one of the artifacts of the precipitation correction is the loss of the water budget closure, which resulted in the ocean component losing water. Hence, ODAS5.2 followed the same procedure, but with no correction to precipitation.

Since the ODAS5.0 analysis did not agree with other analyses as well as ODAS4.0 did, the observation errors were adjusted again for GEOS ODAS5.1. An updated static ensemble was used for both ODAS5.1 and ODAS5.2. The updated ensemble was constructed by taking the leading EOFs of an ensemble of forecast anomalies (calculated relative to the climatological drift) obtained from GEOS-5 AOGCM seasonal hindcast tests initialized from the ODAS5.0 analysis.

5.3.1 Assimilation set-up

The observations are assimilated every 5 days, with observations in a 10-day window centered at the time of the analysis. Seven sequential analyses of different types of observations are performed in sequence. While the k-th analysis uses the state from the (k-1)-th analysis for its background (first guess), the variance of the static ensemble used for the background error covariance stays the same. The sequence of analyses is as follows:

1. *T(z)* and *S(z)* from WOA09 at 1° resolution and from 0 to 4500m
2. Sea surface salinity (SSS) from WOA09
3. Sea level anomalies (SLA)
4. SST
5. *T(z)* from in-situ profiles
6. *S(z)* from in-situ profiles
7. Sea-ice concentration.

The method and parameters used for each sequence of analysis are given in Table 1 for the parameters concerning the background error covariance $\boldsymbol{P}$, and Table 2 for the observation error covariance matrix $\boldsymbol{R}$. The justification for the choice of parameters is discussed in the following sections.

Table 1: Parameters used for the representer functions of equation (4.3) in ODAS5.1 and 5.2. The first column is the analysis sequence. Lines 1, 2, 4 and 7 give the parameters for the Gaussian shaped covariances. Lines 3, 5 and 6 are the parameters for the localization function used to correct the sampled covariance obtained from the static ensemble. L_x and L_y are in degrees of longitude and latitude, respectively.

	L_x [deg]	L_y [deg]	L_z [m]	L_t [day]	L_T [°C]	L_S	γ	SAFE	EnOI	Field(s) updated
1	1	1	10	10			0.01	X		*T* and *S*
2	5	2.5	100	10		0.5	1.0	X		*S*
3	20	15	1500	10			1.0		X	SLA and *T*
4	5	2.5	500	10	2		0.2	X		*T*
5	30	15	500	10	5		0.2		X	*T* and *S*
6	30	15	500	10		0.5	0.2		X	*S*
7	8	4	25	10			1.0		X	*T* and *S*

*Table 2: Scales used for the observational covariance function, **R.** The first column is the analysis sequence. L_x and L_y are defined as in Table 1.*

	L_x [deg]	L_y [deg]	L_z [m]	L_t [day]
1	1	1	0	0
2	2	1	0	10
3	2	1	0	10
4	2	1	0	10
5	0	0	50	10
6	0	0	50	10
7	0	0	0	10

5.3.2 Climatological constraint

Sequences 1 and 2 constitute a constraint by the WOA09 climatology of *T* and *S*. The reasons for using this constraint are two-fold: (1) to force the model to a reasonable climatology, and (2) to correct for errors in fresh water fluxes and runoff by assimilating SSS.

Because of the relatively high resolution of the WOA09 climatology (1 degree horizontally and 40 levels vertically), the spatial scales imposed are quite small (line 1 of Table 1) to reduce the computing cost of the first assimilation. The inflation factor was adjusted through trial and error until a realistic climatology was obtained, while the variance of the system was still acceptable. The observational error variance was set to be 100 times the relevant diagonal element of ***P***.

The parameters for the assimilation of SSS are given in the second line of Table 1. Only 10% of the SSS climatology data points, randomly selected, are included per assimilation window. The

horizontal scales and inflation factor were also adjusted through trial and error with a similar target as for the assimilation of climatological profiles. The vertical influence of the SSS observations is limited to 100 m or the depth at which the salinity difference is 0.5 from the background at the surface, whichever is the shallowest. Figure 7 shows the observation error (the square root of the diagonal of $\boldsymbol{R}$) used for SSS. It was estimated by calculating the mean difference between WOA09 and Argo surface salinity in 1-degree bins over a period of 8 years (2003-2010). The observation error was reduced in regions of large runoff to 0.001.

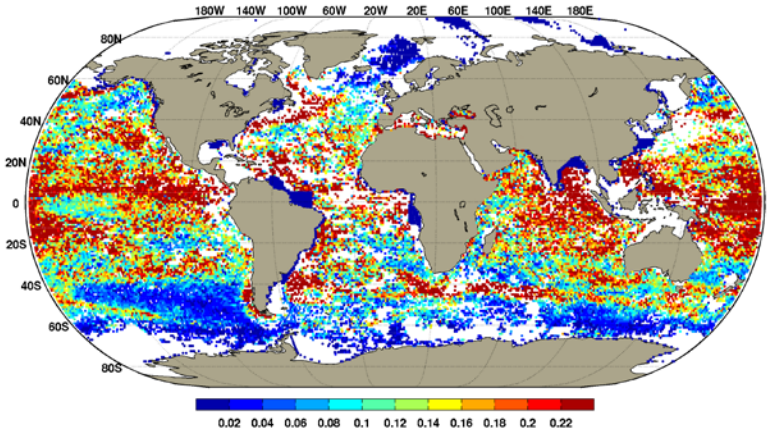

Figure 7: Estimation of the observation error for SSS.

5.3.3 Along-track sea level anomalies

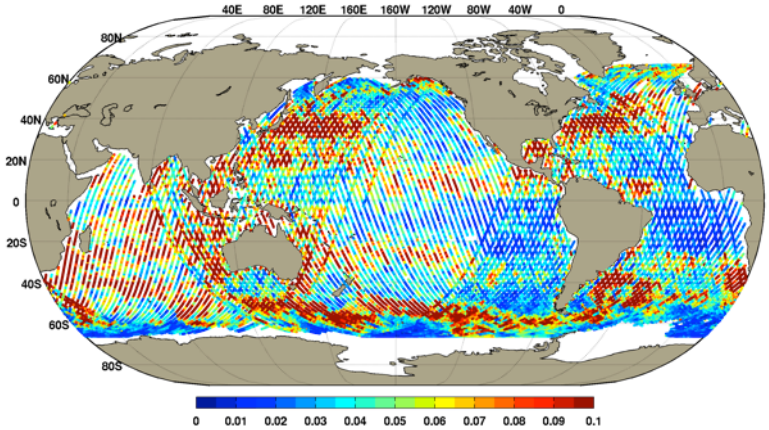

Figure 8: Example of an estimate of the observation error standard deviation for SLA (m).

The SLA observations used in GEOS ODAS5.2 are along-track merged products obtained from AVISO, referenced to a 7-year mean (January 1993 to January 1999). Because of the high resolution of the AVISO product (adjacent SLA measurements are approximately 20 km apart), the along-track observations are high-pass filtered using a Gaussian kernel with a stencil size of 21 and a decorrelation length scale of 100 km. The along-track variability over 200 km segments is used as a proxy for the errors of representativeness; a snapshot of that estimate is depicted in Figure 8. No instrument error is imposed.

The model SLA is given by $\eta' = \eta - \bar{\eta}$, where the mean sea level $\bar{\eta}$, also referred to as the mean dynamic topography (hereafter, MDT), is the 7-year mean sea level of GEOS ODAS5.1 from

January 1993 to December 1999 (see Figure 9) and η is the total sea level from the barotropic component of the ocean model.

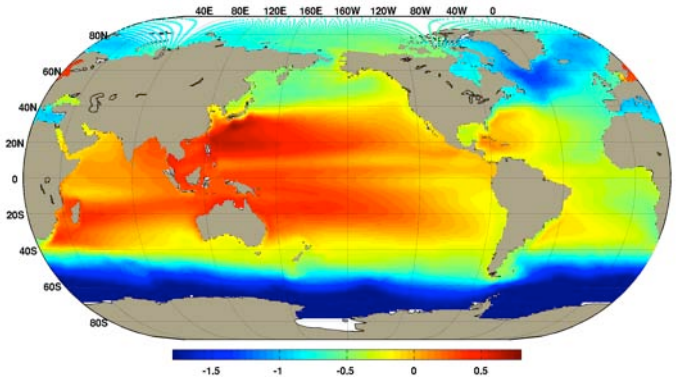

Figure 9: The model mean sea surface height (m), January 1993-December 1999.

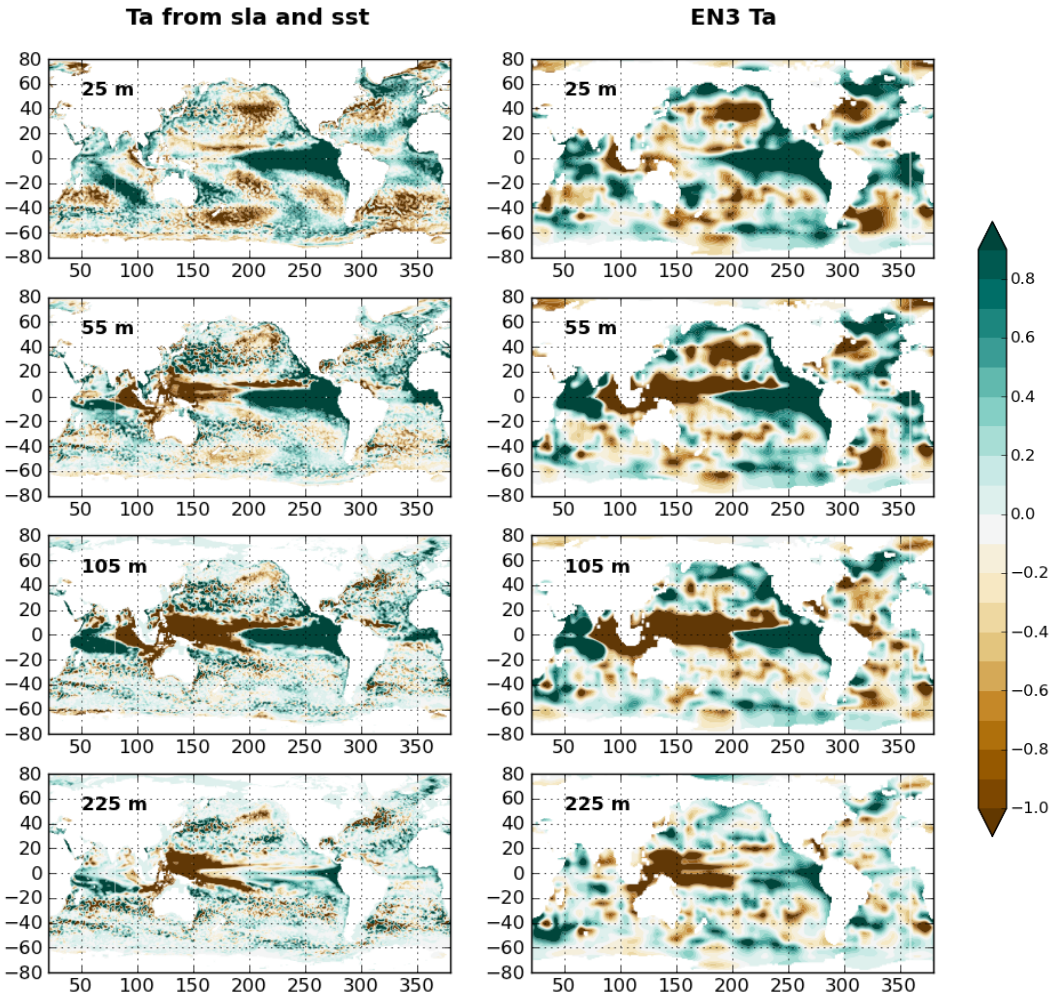

Figure 10: Upper ocean temperature anomaly (°C) at selected depths (25 m, 55 m, 105 m, and 225 m) for December 1997. Left column is the off-line analysis based only on SLA and SST; the right column is the EN3 objective analysis.

Within the EnOI framework used for the assimilation of the SLA, an increment in η is accompanied by an increment in the three-dimensional T field (see last column of line 3 of Table 1). A poor estimate of the T could be caused by the wrong choice of MDT ($\bar{\eta}$) or wrong cross-covariances between SLA and T. Whether the MDT chosen in the analysis is appropriate is still an active area of research and will not be discussed in this report. In order to separate the two sources of error, and only investigate the robustness of the cross-covariances, an objective (model-less) analysis was carried out, in which SLA are used as a predictor for T anomalies (hereafter, T') over the entire water column, therefore avoiding the need for an estimate of the MDT. To simplify the vertical projection, the daily gridded SLA from AVISO is used. Further, we assume that the errors are horizontally uncorrelated, an observation of SLA at (x, y) is only influencing a single water column of $T'(z)$ at (x, y). Using this simplification, the problem of estimating the three-dimensional T' reduces to many independent one-dimensional vertical projections (as many as there are observations). For this purpose, the entire set of EOFs are used (286) for the computation of the covariance between η and $T'(z)$ at location (x, y). Because of the relatively large size of the ensemble, localization of the vertically dependent covariance is not necessary. Figure 10 shows the monthly average of the upper ocean T' for December 1997, estimated by the vertical projection described above and compared to the EN3 objective analysis. The upper ocean structure of the El Niño phase, characterized by a large positive T' in the eastern tropical Pacific and a large negative T' in the west, is well represented in the analysis, suggesting that the static ensemble is adequate for the projection of SLA onto the three-dimensional T' in the tropical Pacific. Similarities are observed in the extratropics as well, but the off-line analysis features small scales that are clearly not present in EN3. It is doubtful that these small-scale features are realistic; rather, they are artifacts of assuming that the errors are horizontally uncorrelated.

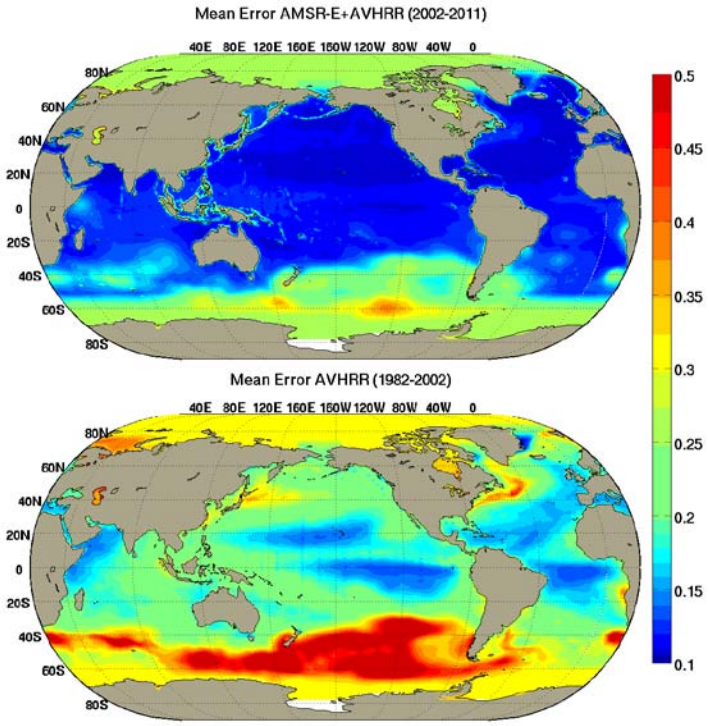

Figure 11: Average observation error for Reynolds SST (°C). The upper (lower) panel is the average for 2002-2011 (1982-2002).

5.3.4 Sea surface temperature

The assimilation of SST is fourth in the sequence depicted in Table 1, correcting the upper analyzed ocean heat content that was a result of the earlier sequence of assimilations within the same time window. When assimilating CMIP5 data (prior to 1982), the observation errors are set to 0.5°C, globally. After 1982, when assimilating Reynolds SST, the observation errors are given by the error in the optimal interpolation used in the creation of the gridded SST retrieval. The mean of the error from 1982 to 2011 is given in Figure 11. The assimilation methodology uses the SAFE algorithm with Gaussian horizontal and vertical covariances. The vertical influence of SST is limited to the minimum of 500 m and the depth at which the temperature differs by 2°C from the temperature at 5 m.

5.3.5 In-situ profiles of temperature and salinity

The assimilation of in-situ profiles of temperature and salinity correspond to sequences 5 and 6 of Table 1. The observations are assimilated twice, in a multi-scale fashion, with the second assimilation being identical to the first except for the horizontal localization scales that are 50% of the scales used in the first assimilation. While both *T* and *S* analyses use the EnOI algorithm, only step 5, consisting of the analysis of *T* profiles, is multivariate (increments in *T* have corresponding increments in *S*). Step 6 consists of the univariate assimilation of *S* profiles. Since most *S* profiles have a corresponding *T* profile, salinity is not used to correct temperature.

Prior to being assimilated, both *T* and *S* are binned according to the model's levels and any profile that contains an observation that is six or more standard deviations (where the standard deviation is taken to be the standard deviation of the interannual variability) away from the WOA09 climatology is rejected. The observation error is modeled with an exponential decay written as

$$\sigma(z) = \sigma_0 exp\left(-\frac{z}{z_0}\right) + \sigma_i, \tag{5.1}$$

where σ_i is the instrument error and the exponential decay term is a proxy for the errors of representation, parameterized with the e-folding depth scale $z_0 = 500$ m and amplitude σ_0. The parameters necessary to specify the observation error according to equation (5.1) are given in Table 3.

Table 3: The parameters used for the observational variance function of equation (5.1) for observation types used in the GEOS ODAS5.2.

	T		**S**	
	σ_0 [°C]	σ_i [°C]	σ_0	σ_i
XBT	0.5	0.1	-	-
CTD	0.5	0.03	0.1	0.02
TAO	0.5	0.02	-	-
PIRATA	0.5	0.02	0.1	0.1
RAMA	0.5	0.09	0.1	0.1
Argo	0.5	0.005	0.1	0.02
SST	0.5 prior to 1982	-	-	-
SSS	-	-	Figure 7	-

The covariances estimated from the static ensemble are localized using equation (4.3) and the parameterization given in lines 6 and 7 of Table 1. When assimilating *T* (or *S*), v in equation (4.3) is *T* (or *S*). This localization choice allows for small vertical scales above the thermocline, where the extent of vertical scales is mostly limited by the localization in *T* (or *S*), and large scales below the thermocline where the vertical influence of the observation is limited by L_z.

5.3.6 Sea-ice concentration

The last sequence consists of the assimilation of sea-ice concentration, from NSIDC or CMIP5. Sea-ice concentration is defined as the fraction of ocean area covered by sea ice and assumed to be the same variable as the sum of the five types of fractional sea ice in the CICE model where the total fractional ice coverage is

$aice = 0$ if there is no ice
$aice = 1$ if there is no open water
$0 < aice < 1$ if there is both ice and open water.

Since the total concentration, *aice*, is a diagnostic variable in CICE, one would need to project the observations onto the five types of ice concentrations. An implementation in which the observed ice fraction was decomposed into the five prognostic types of ice fraction using the same ratios as the background was found to be numerically unstable most of the time. Instead, *T* and *S* increments are computed using the covariances between *aice*, *T* and *S* from the static ensemble. Again, to account for the small size of the ensemble, and the resulting errors in the estimation of distant correlations, a localization procedure is used. The parameters of the localization are given in line 8 of Table 1. The observation error is prescribed as 0.05.

6 Results and diagnostics

6.1 Active tracers

The advent of the Argo observing system has had a large impact on ocean analyses, so much so that the sharp changes in the climatology of the analysis post and prior to the Argo period is most often largely attributed to the higher resolution of these observations, rather than a real change in the climate of the ocean. This is illustrated in Figures 12a and b, which show the root mean square (RMS) observation-minus-forecast (OMF) for *T* and *S*, respectively. For both *T* and *S*, the most striking change occurs below 300 m, where the ocean was largely unobserved prior to Argo, while the improvement in the upper 300 m is more subtle and localized to areas of relatively small variability.

When looking at the time series of *T* averaged over the upper 300 m, a useful proxy for the heat content in the upper 300 m, a similar artifact is observed, where the analysis (red line in the upper panel of Figure 13) converges to the EN3 objective analysis, suggesting a reduction of the uncertainty for the state of the global *T* during the period of maturity of the Argo deployment. However, this is not true when looking at *T* averaged over the upper ocean in the tropical band, 30°S-30°N (left-hand panel of Figure 14), where the difference between the two analyses remains similar throughout the period shown. This is due to the availability of data from the tropical Pacific moorings, especially the TAO/TRITON array, which constrains both the analysis and EN3 and reduces the uncertainty in *T*. The global mean salinity from the GEOS analysis is closer to the WOA09 climatology than to the salinity in EN3. The difference from EN3 is about 0.02. The agreement between the GEOS analysis and EN3 is much closer in the tropical band (Figure 14). Interestingly after 1999, there is an offset between the two of about 0.01.

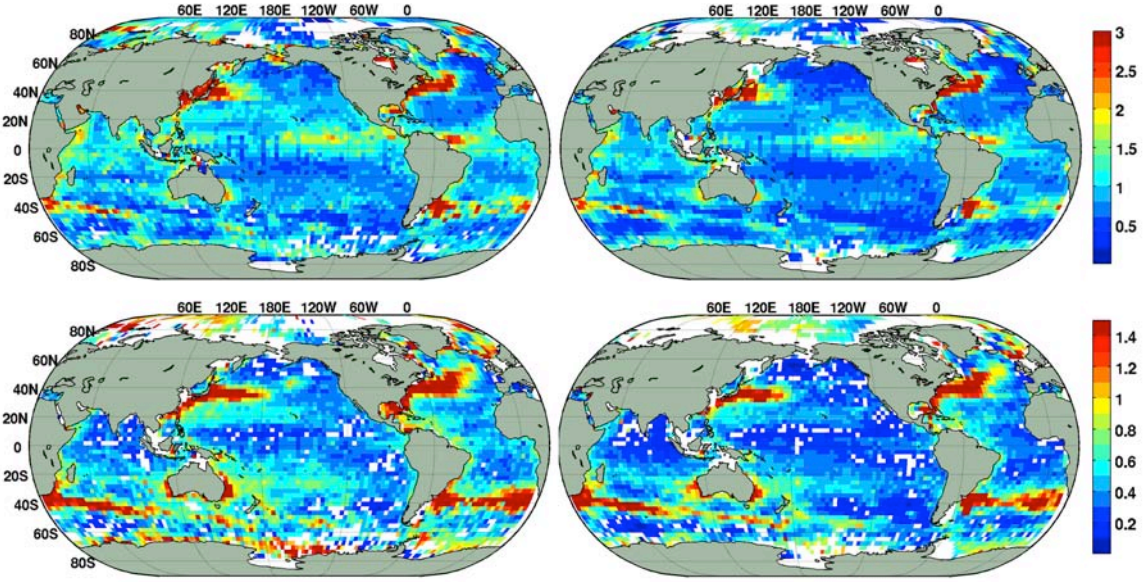

Figure 12a: The RMS of OMF for temperature (°C). The left columns are for the 1993-2005 period, the right columns for 2006-2011. The upper panels are for the upper 300 m; the lower panels for 300-1000 m depths.

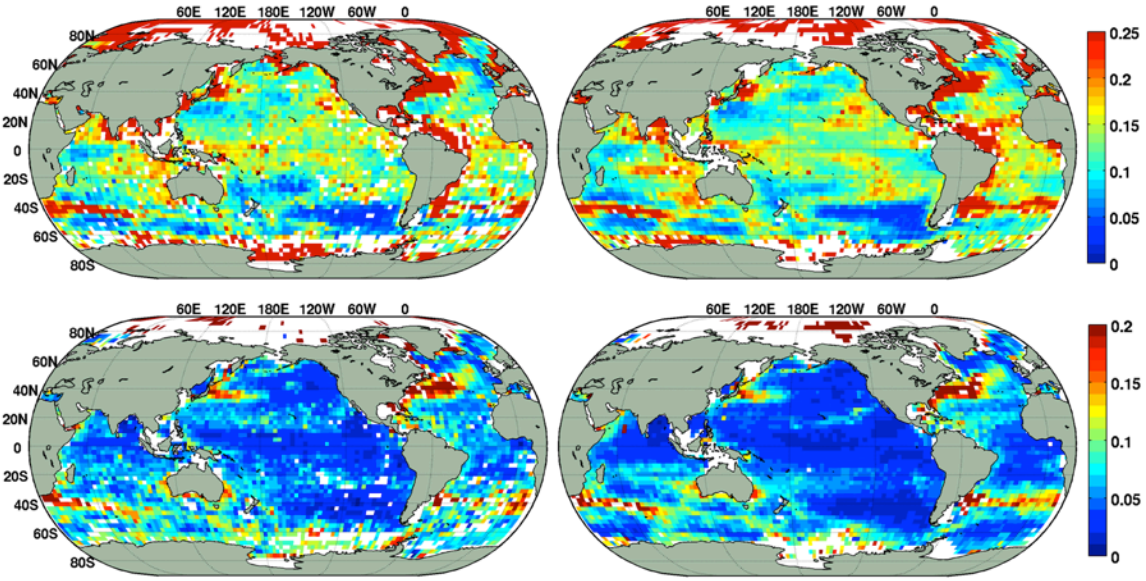

Figure 12b: As for Figure 12a, but for salinity.

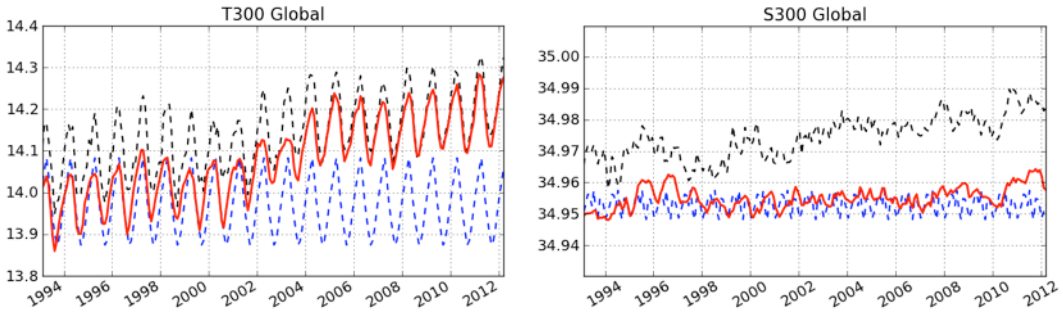

Figure 13: Left: Global mean temperature (°C) averaged over the upper 300 m. The red line is for the GEOS ODAS5.2; the dashed grey line is for EN3, the dashed blue line is from WOA09. Right: Salinity averaged over the upper 300 m.

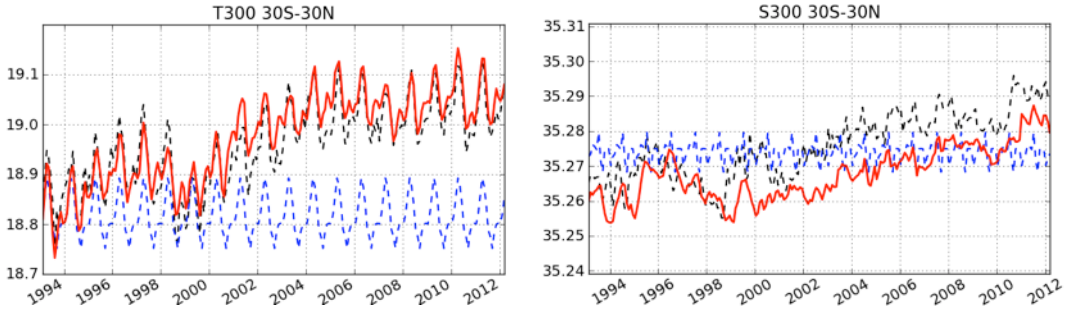

Figure 14: As for Figure 13, but for the tropical band, 30°S-30°N.

6.2 Statistics from the assimilation process

To interpret the fit of the analysis to the observations, we first look at the global statistics of the reduced penalty functional (see equation 6.1 below). Following Bennett et al. (1998) we can use our data assimilation system to test an hypothesis, in which the null hypothesis is based mainly of estimates of observation errors, errors of representation and model errors. The residuals, or the posterior value of the cost function, from the linear regression in equation 4.1, are written as

$$\hat{J} = \boldsymbol{h}^T(\boldsymbol{HPH}^T + \boldsymbol{R})^{-1}\boldsymbol{h}, \tag{6.1}$$

where $\boldsymbol{h}$ is the innovation (or OMF). $\hat{J}$ follows a χ^2 distribution with the number of degrees of freedom equal to the number of observations processed in the assimilation. In the limit of large N_0, the χ^2 distribution is approximated with a normal distribution with first moment $E\left(\chi^2_{N_0}\right) = N_0$ and second moment $var\left(\chi^2_{N_0}\right) = 2N_0$. The test is summarized as follows:

If $\hat{J} < N_0$, then the value chosen for γ in equation (4.4) was too large and the model over-fits the observation.
If $\hat{J} > N_0$, then γ should have been larger.

Time series of the normalized value of $\hat{J}$ for each observation type are shown in Figure 15. Because of the normalization, the expected value of $\hat{J}$ is 1.

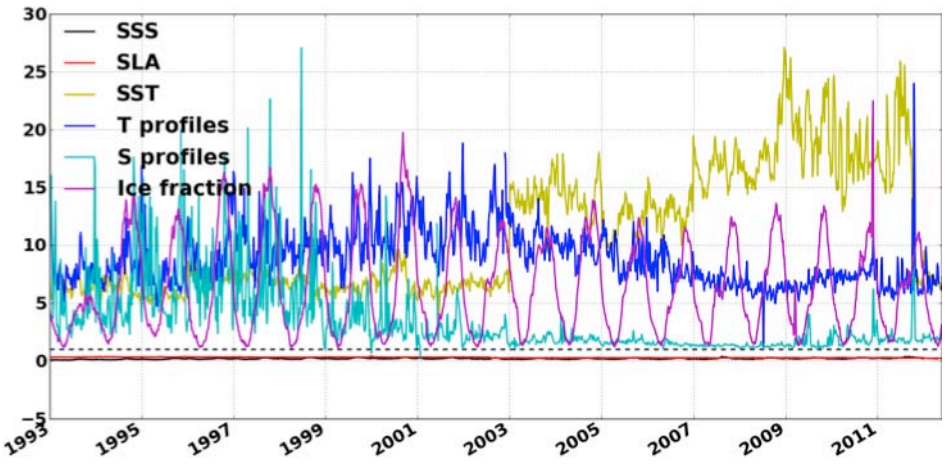

Figure 15: Normalized cost function, $\hat{J}$, for each sequence of assimilation.

The black line in Figure 15 is the $\hat{J}$ corresponding to the assimilation of WOA09 SSS, it has a mean of 0.19, indicating that the observation errors are too small or the background error variance estimated from SAFE is too large. The same is true for the assimilation of SLA (red line), which has a mean value of 0.29 for $\hat{J}$, indicating that the estimated observation and representation errors are too small, or the variance of the static ensemble is too large. The yellow line of Figure 15, corresponding to the assimilation of SST, has a mean well above 1 and sharp changes in 2003 and 2011, corresponding to a significant change in the observing system and the instrument error associated with it (see Figure 11). The total error estimate for the SST observations do not include errors of representation, but rather the error of the OI algorithm used to grid the Reynolds SST field, providing a lower bound estimate for the diagonal of $\boldsymbol{R}$. This implies that the model error for SST was underestimated, and the surface variance of T in the static ensemble underestimates the background error variance. The purple line of Figure 15 corresponds to the evolution of $\hat{J}$ for the assimilation of ice fraction over both polar regions. It includes a strong seasonal cycle with a minimum close to 1 in April and a maximum between 10 and 15 in September, indicating that the observational error and the covariance model should have included a seasonal component.

The χ^2 statistic for the in-situ profiles of T, depicted as the blue line in Figure 15, is well over unity for the entire analysis period, suggesting that our background covariance model has too little amplitude and our estimate of representation error was possibly too large. Finally, the cyan line of Figure 15, representing the evolution of $\hat{J}$ for the assimilation of in-situ S profiles, starts off significantly larger than 1 but slowly converges to its expected value during the Argo period, indicating that our models for the representation error and background error are adequate during the more recent years.

No attempt was made to adjust γ so that the normalized $\hat{J}$ would be close to its expected value of 1; instead, the ratio of observation error to background error was adjusted so that the forecast would be numerically stable.

The temporal evolution of the global RMS of OMFs and OMAs (observation minus analysis, also referred to as analysis departures) for the surface observations, SST, SSS, SLA and *aice*, is shown in Figure 16. The global RMS of OMFs corresponding to the in-situ observations of T and S are analyzed in the time-depth plane and shown in Figure 17. As expected, the larger errors for T and S are found within the thermocline.

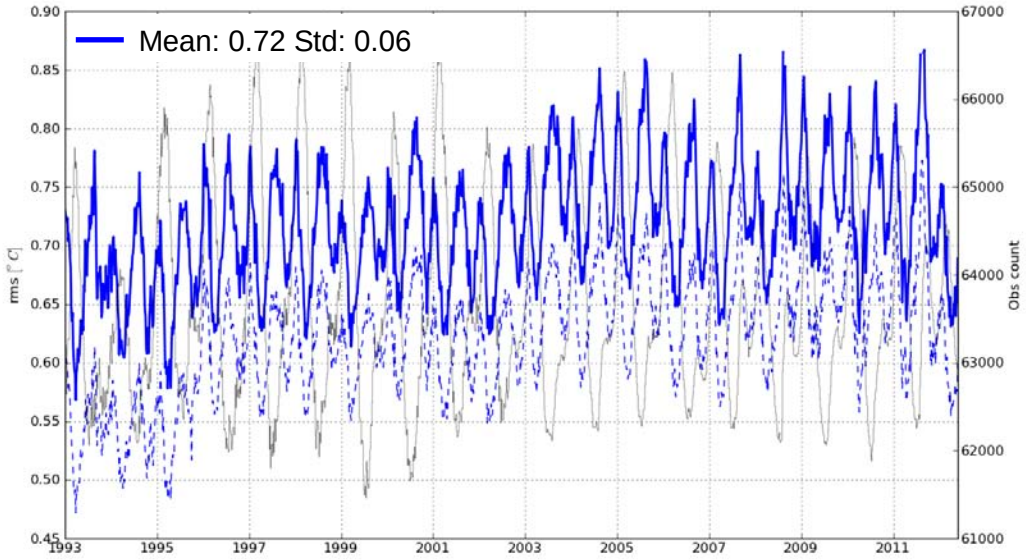

Figure 16a: The solid blue line is the global RMS of OMFs for SST (°C). The mean RMS is 0.72°C and the standard deviation is 0.06°C. The dashed blue line is the RMS of OMA. The grey line is the observation count per assimilation window (right-hand ordinate).

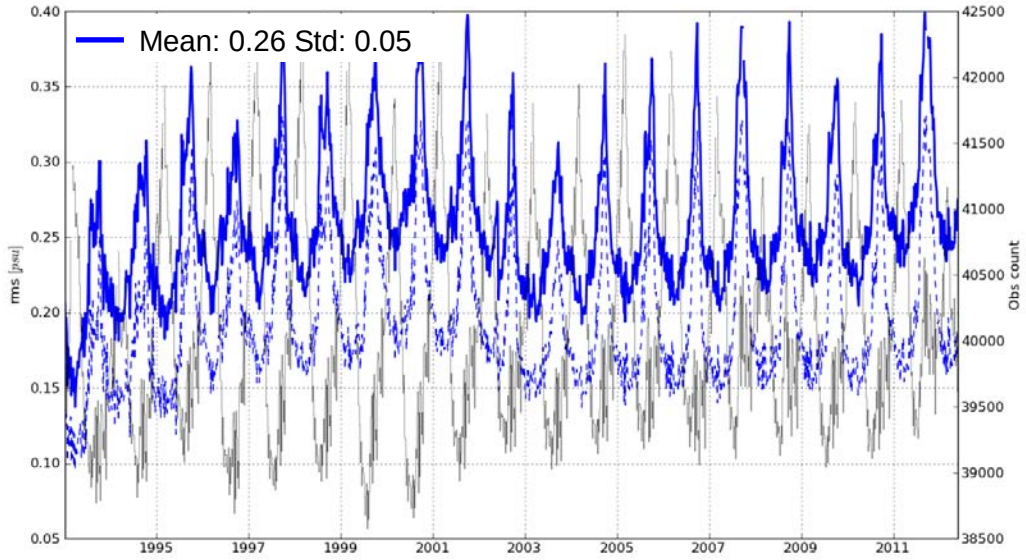

Figure 16b: As for figure 16a, but for SSS. The mean RMS is 0.26 and the standard deviation is 0.05.

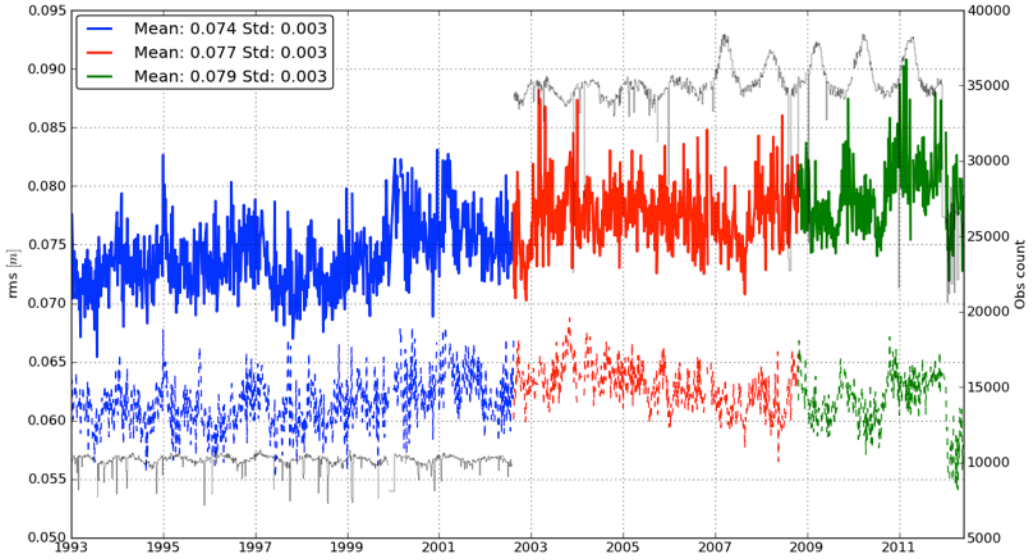

Figure 16c: As for figure 16a, but for SLA (m). The blue lines correspond to the TOPEX/Poseidon period; the red lines are for the Jason-1 period and green for Jason-2.

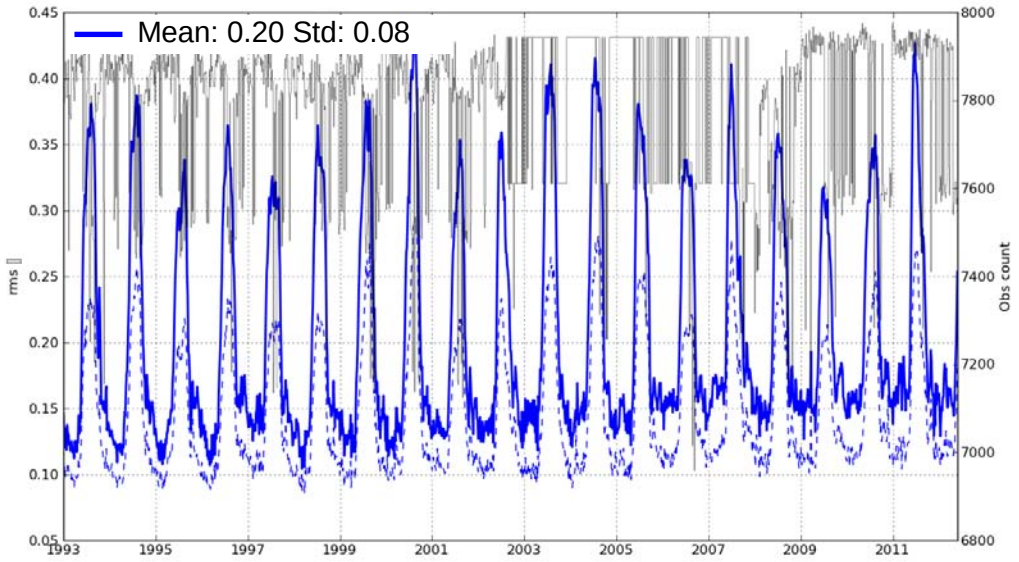

Figure 16d: As for figure 16a, but ice fraction over the Arctic.

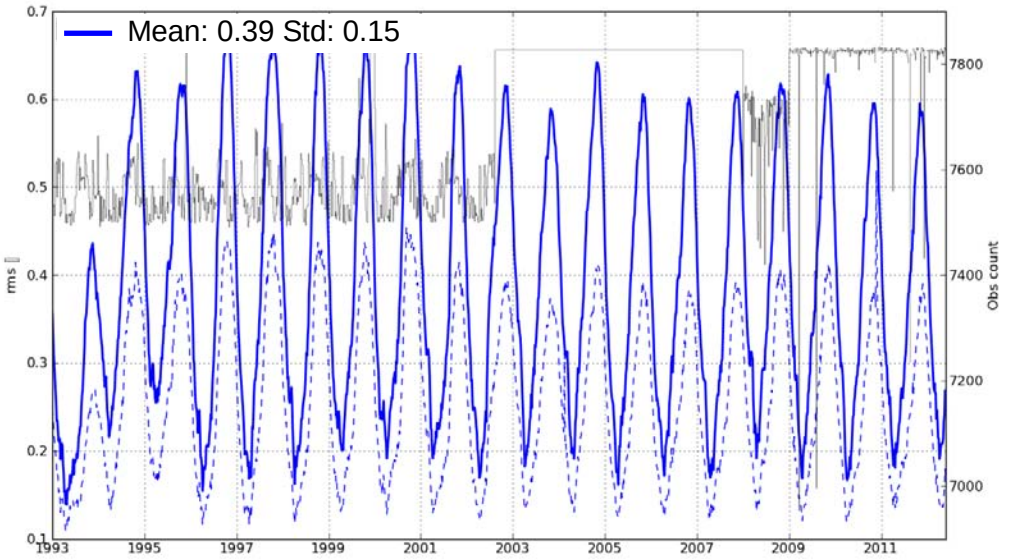

Figure 16e: As for figure 16a, but ice fraction over the Antarctic.

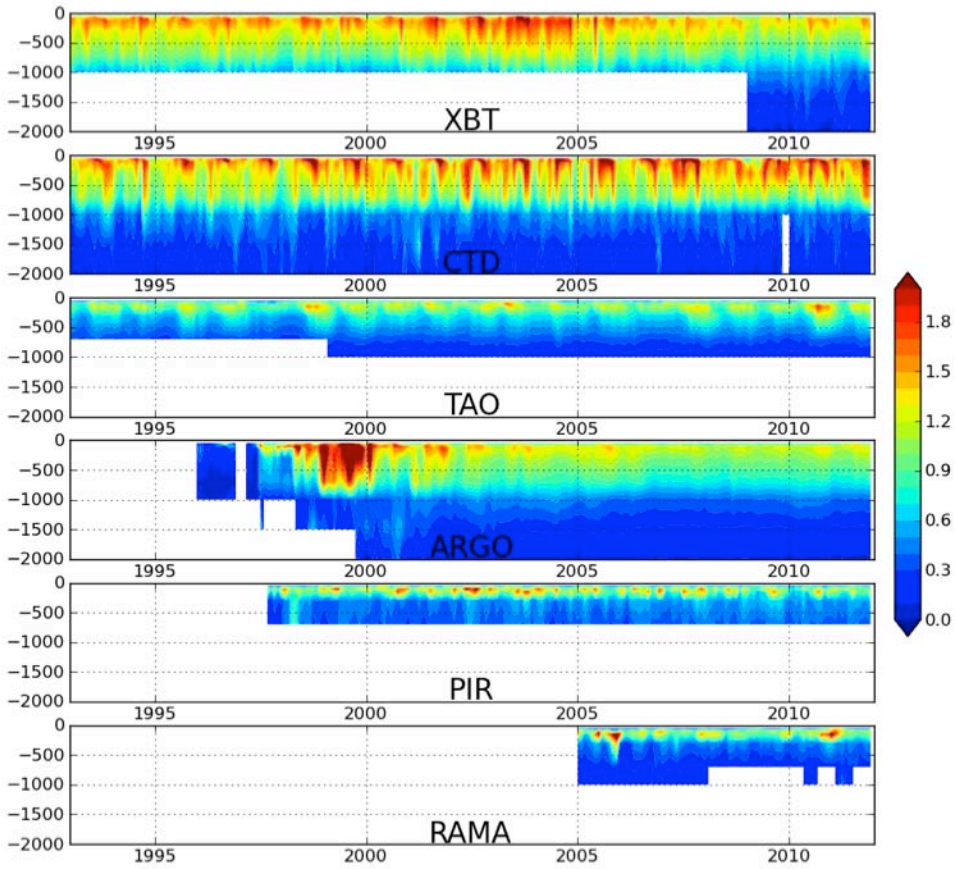

Figure 17a: Time series of global RMS of OMF for temperature (°C) as a function of depth.

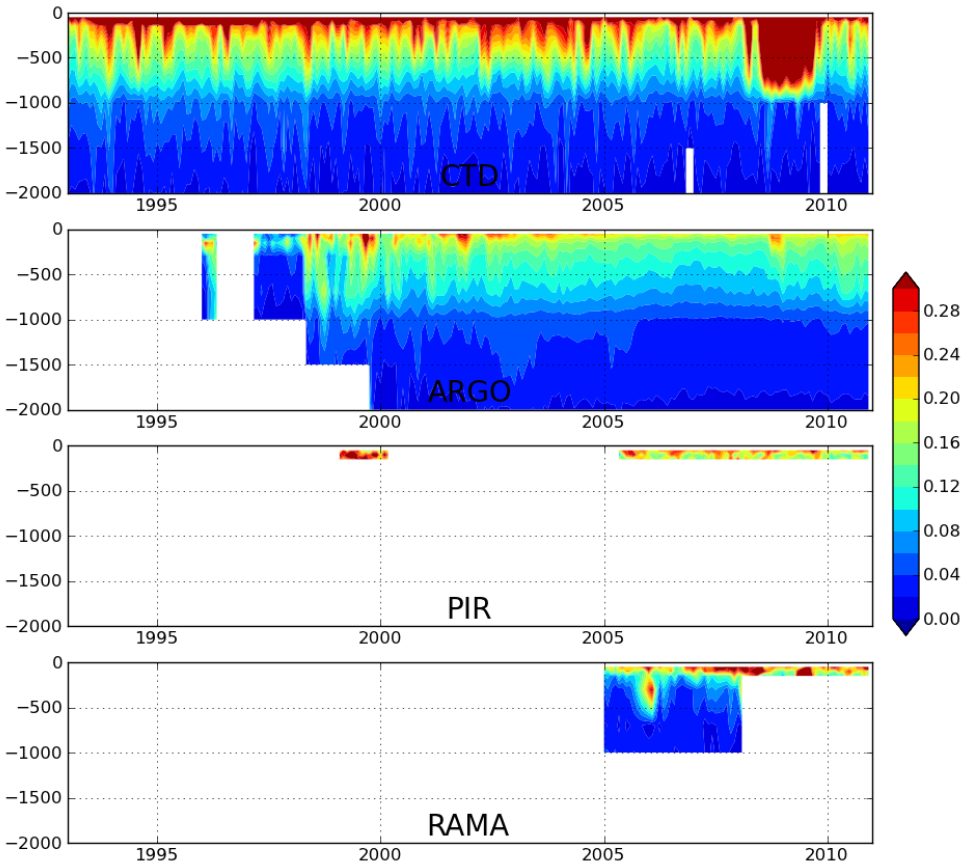

Figure 17b: Time series of global RMS of OMF for salinity as a function of depth.

Summaries of the mean and RMS statistics from the innovations and analysis departures averaged as a function of depth for 2002 to 2011 are presented in Figures 18 and 19 for the tropics (30°S to 30°N) and extratropics (60°S to 30°S and 30°N to 50°N) for CTDs and Argo.

For CTDs and Argo, the RMS departures are largest in the northern extratropics for both *T* and *S*, with the background and analysis being biased warm relative to the CTD observations throughout the upper 1800 m. This is also the case over most of the upper 1800 m in the southern extratropics. The RMS errors for temperature relative to Argo in the upper 1000 m and salinity in the upper 200 m in the northern extratropics are smaller than those relative to CTD observations. This is most likely due to the much larger number of Argo observations that are then more effective in constraining the analysis. The structure and magnitude of the RMS errors in the tropics and southern extratropics are similar relative to both CTD and Argo observations. In general, both background and analysis have a very low bias relative to Argo.

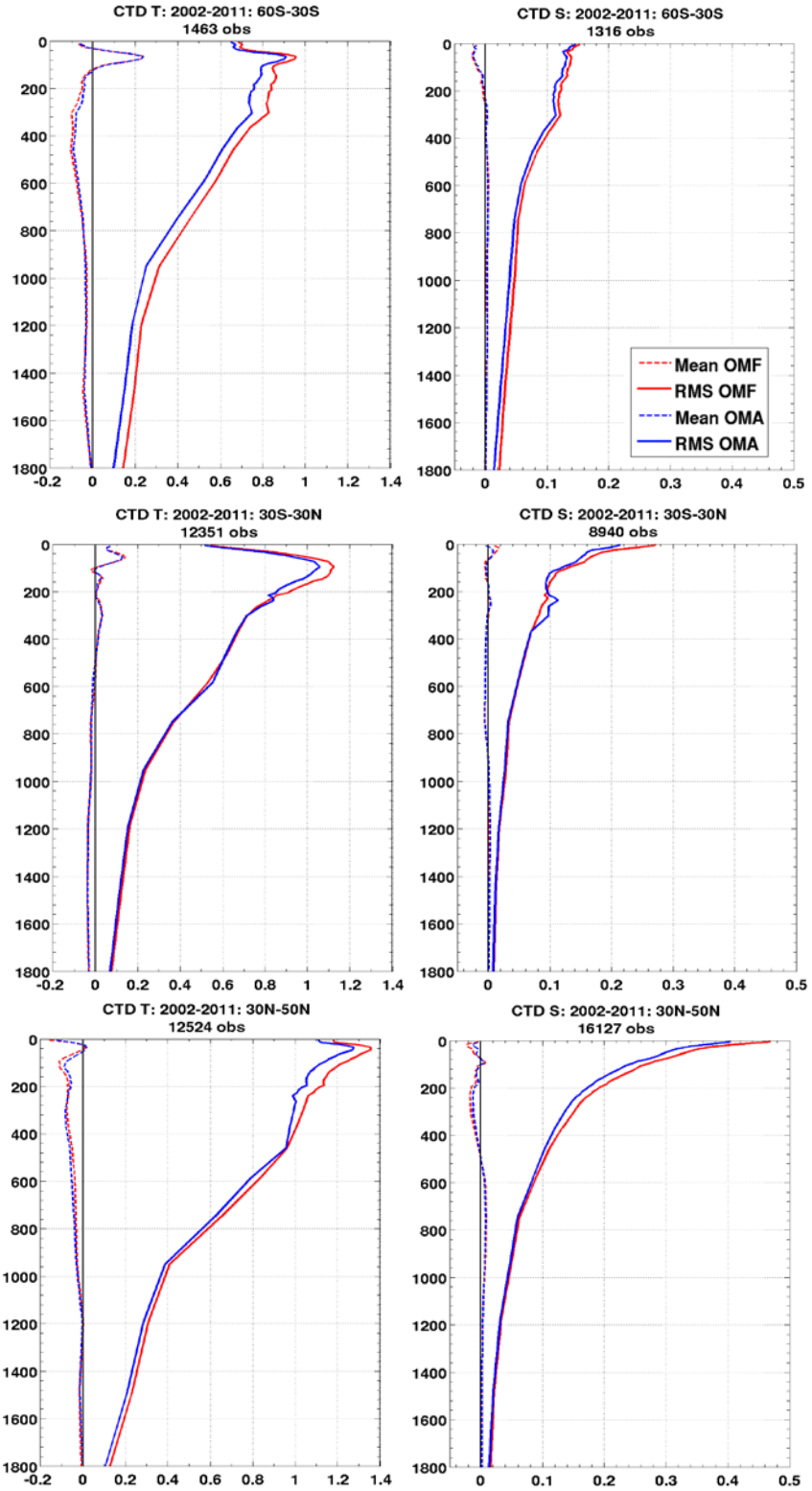

Figure 18: Mean (dashed line) and RMS (solid line) of the OMF (red) and OMA (blue) for CTD temperature (left) and salinity (right), in the southern extratropics (upper), tropics (middle) and northern extratropics (lower). The statistics are calculated for 2002-2011 as a function of depth.

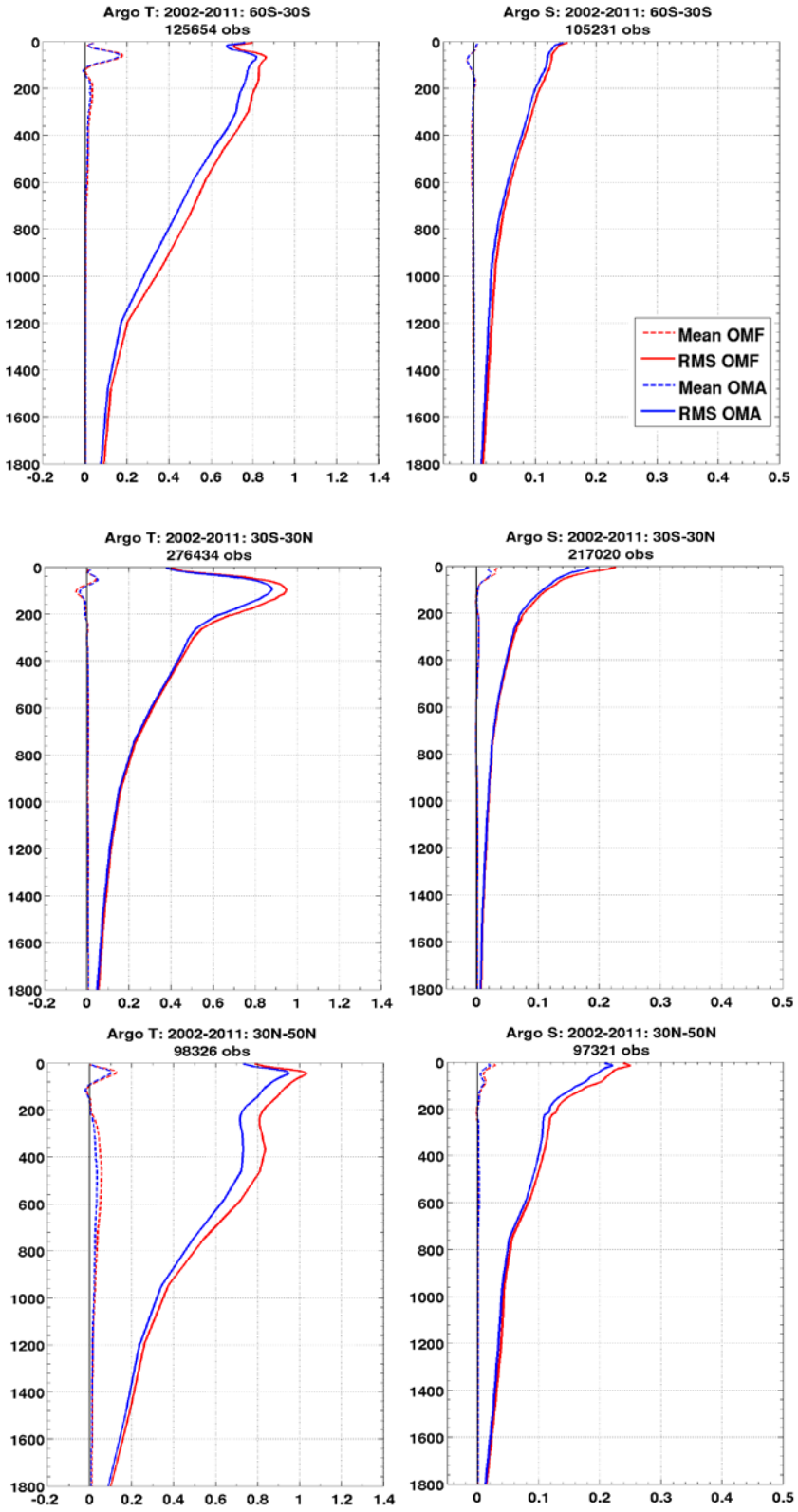

Figure 19: As for Figure 18, but for Argo.

6.3 Sea-level

6.3.1 Comparison with altimeter and tide gauge data

Not surprisingly, the comparison of sea level from the analyses with observations (Figure 20) indicates that the assimilation of along-track SLA data improves the analysis agreement with the gridded AVISO product. Even with assimilation, there are large discrepancies in regions of strong currents and large variability. The high agreement of ODAS5.1 with the altimeter data in the equatorial Pacific comes from the high quality of data from the TAO moorings. Interestingly, the ODAS5.1 agrees with the altimeter data better in the Indian Ocean than the Atlantic Ocean, presumably because of the strong seasonal cycle in that basin and the good distribution of Argo data late in the observing period.

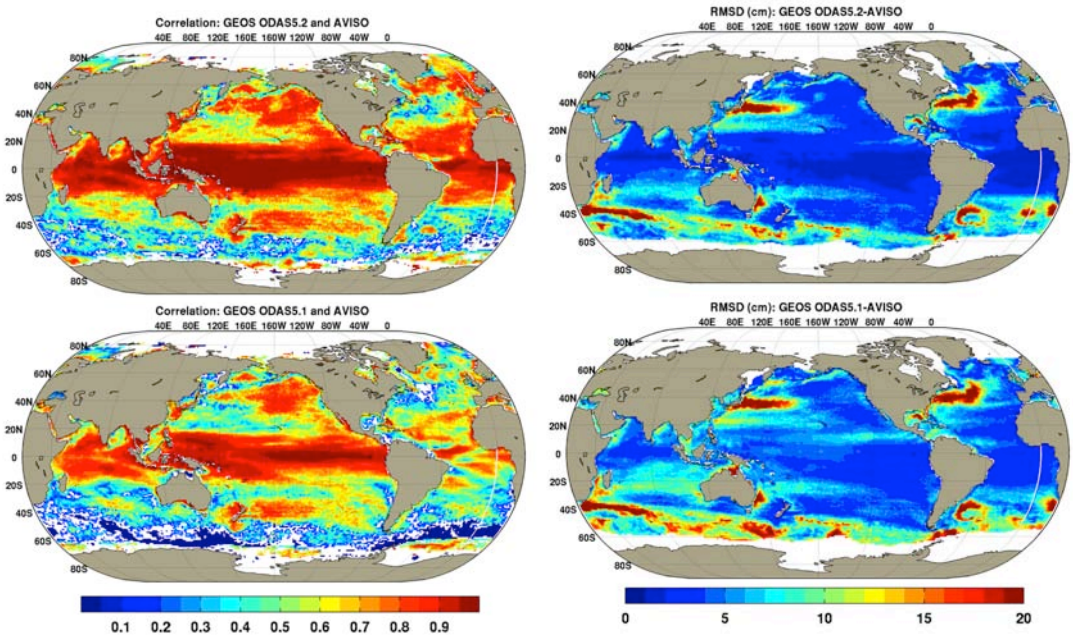

Figure 20: The left-hand panels show the correlation of SLA from the GEOS analyses from 1993 to 2011 with gridded SLA from AVISO. The upper plot is for the GEOS analysis that assimilates the SLA data; the lower plot is from the analysis that does not assimilate SLA data. The right-hand panels are the RMS difference (cm) between the analyses and the AVISO data.

The quality of the analysis with altimeter data assimilated can also be evaluated by comparing with the independent data from tide gauges, with the caveat that many tide gauges are not representative of open ocean conditions. Figure 21 shows the difference between the RMS of analysis departures from tide gauge data – the RMS from the analysis with SLA data minus the RMS from the analysis without SLA data. The predominance of negative values, the blue-green colors, show the analysis with SLA data assimilated compares better with the tide gauge data than that with no SLA assimilation. The time series of differences from tide gauge data and from AVISO SLA are shown for a few gauges in the equatorial waveguide. The comparison shows that the differences from the tide gauge data are consistent with the differences between the tide gauges and the AVISO product.

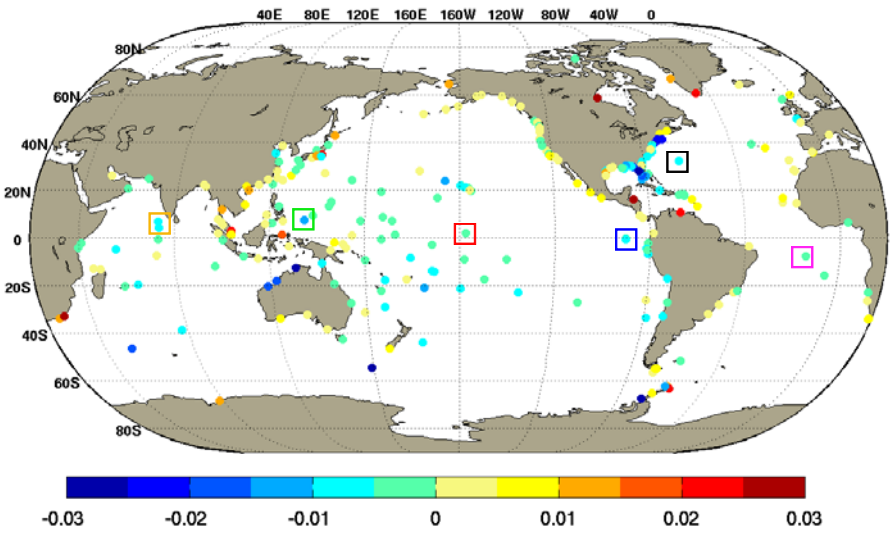

Figure 21: RMS of OMF for tide gauge data (passive): analysis with SLA data minus analysis without SLA data. Negative values indicate that SLA assimilation has a positive impact.

2°N, 157.5°W Central equatorial Pacific Ocean (the red square in Figure 21)	Tide gauge	AVISO SLA
Tide gauge		0.054
GEOS ODAS5.1	0.056	0.047
GEOS ODAS5.2	0.052	0.029

7.3°N, 134.5°E Western equatorial Pacific Ocean (the green square in Figure 21)	Tide gauge	AVISO SLA
Tide gauge		0.062
GEOS ODAS5.1	0.082	0.076
GEOS ODAS5.2	0.072	0.056

0.8°S, 90.3°W Eastern equatorial Pacific Ocean (the blue square in Figure 21)	Tide gauge	AVISO SLA
Tide gauge		0.034
GEOS ODAS5.1	0.040	0.034
GEOS ODAS5.2	0.032	0.026

32.4°N, 64.7°W Western tropical Atlantic Ocean (the black square in Figure 21)	Tide gauge	AVISO SLA
Tide gauge		0.100
GEOS ODAS5.1	0.105	0.112
GEOS ODAS5.2	0.094	0.084

32.4°N, 64.7°W Central equatorial Indian Ocean (the orange square in Figure 21)	Tide gauge	AVISO SLA
Tide gauge		0.069
GEOS ODAS5.1	0.093	0.044
GEOS ODAS5.2	0.085	0.036

7.9°S, 14.4°W Central equatorial Atlantic Ocean (the pink square in Figure 21)	Tide gauge	AVISO SLA
Tide gauge		0.031
GEOS ODAS5.1	0.038	0.024
GEOS ODAS5.2	0.035	0.022

6.3.2 Global sea level variations

In this section, the impact of the assimilation on global sea level and water volume budget is presented. When integrated globally, the two constituents of the mean sea level are steric height, that can be further decomposed into halosteric and thermosteric height, and volume input from outside sources. In the case of the CM2 configuration, the outside source of water mass to the ocean is the imbalance between run-off water and atmospheric fresh water fluxes. The steric height anomaly η^{ST} is defined as

$$\eta^{ST}(x,y,t) = -\frac{1}{\rho_0}\int_{-H}^{0}\left[\rho\big(T(x,y,z,t),S(x,y,z,t)\big) - \rho\big(T_0(x,y,z,t),S_0(x,y,z,t)\big)\right],$$

where $\rho_0, T_0,$ and S_0 are climatological values. It represents the contraction or expansion of seawater due to thermal and haline variability. The haline contribution, η^{HST}, is defined as

$$\eta^{HST}(x,y,t) = -\frac{1}{\rho_0}\int_{-H}^{0}\left[\rho\big(T_0(x,y,z,t),S(x,y,z,t)\big) - \rho\big(T_0(x,y,z,t),S_0(x,y,z,t)\big)\right].$$

The thermal contribution, η^{TST}, is defined as

$$\eta^{TST}(x,y,t) = -\frac{1}{\rho_0}\int_{-H}^{0}\left[\rho\big(T(x,y,z,t),S_0(x,y,z,t)\big) - \rho\big(T_0(x,y,z,t),S_0(x,y,z,t)\big)\right].$$

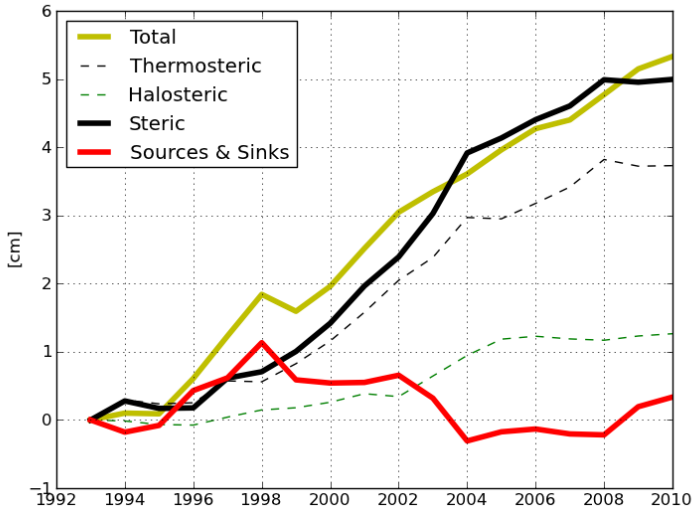

Figure 22: Area-weighted average of the contributions (haline is dashed green and thermal is dashed black) to changes in steric height (solid black line) and sea-level anomalies (yellow line) in cm, referenced to 1993.

Figure 22 shows the global area-weighted yearly mean steric height η^{ST}, its haline and thermal components and the sea level, all referenced to 1993. The overall increase in sea level over this period is consistent with that inferred from altimeter and Argo data (Leuliette and Willis 2011). The major contribution to steric height changes during the period of the analysis is from the thermal component, η^{TST}. From the slope of the solid black line and the yellow line of Figure 22 one can infer that the sea level rise from 1993 to 1999 is of both thermal and external origin (land ice melt and changes in precipitation, evaporation, and run-off). After 2004, the analyzed steric height change has a significant contribution from the halosteric component, η^{HST}. This change, which must arise from the "sudden" availability of new global information on the salinity distribution, is artificial and highlights the issues that can arise in inferring climate variability with a changing observing system. In contrast, Leuliette and Willis (2011) find that after 2005,

the sea level rise has a greater contribution from an increase in the ocean mass due to the input from melting glaciers and ice sheets than from thermosteric effects.

6.4 Thermohaline circulation

The Atlantic meridional overturning circulation (AMOC) is a major component of the thermohaline circulation and an indication of the state of the climate system since it quantifies the meridional transport of heat. Several of its constituents are depicted in Figure 23, showing the meridional transports at 26.5°N. Positive transports correspond to northward flow. The solid red line is the analysis estimate of the Florida Strait transport, while the dashed red line is the cable transport estimate. The analysis transport is slightly weaker than observed, possibly due to the relatively low resolution of the ocean model. The solid green line is the GEOS Ekman transport. The dashed green line is the Ekman transport estimated from the Cross Calibrated Multi-Platform (CCMP) wind product (see http://www.noc.soton.ac.uk/rapidmoc/) and is in reasonable agreement with the GEOS analysis. The mid-ocean transport, calculated as the vertical integral of the transport per unit depth down to the deepest northward velocity (~1100 m) on each day, closes the transport budget. The sold gold line is the GEOS ocean analysis estimate, which agrees well with the RAPID-MOC estimate (e.g., Rayner et al. 2011). The overturning transport is then the sum of the Florida Straits, Ekman, and upper mid-ocean transports and represents the maximum northward transport of upper-layer waters on each day. The mean GEOS ocean analysis estimate for the maximum AMOC is 14.0 Sv with a standard deviation of 3.2 Sv over the period of the analysis; this is weaker that the RAPID estimate of 17.4 Sv with a standard deviation of 4.9 Sv. It is likely that a major contribution to the weak estimate is the underestimation of precipitation or the overestimation of evaporation over the Atlantic between 5°N and 32°N, as inferred from Figure 24 which shows the overturning stream function is significantly weaker in this region. The total transport, calculated top to bottom and across the Atlantic section from Florida to Africa, is the black line of Figure 23; the apparent non-closure reflects the transport leakage through the Bering Strait and the fresh water flux from the forcing.

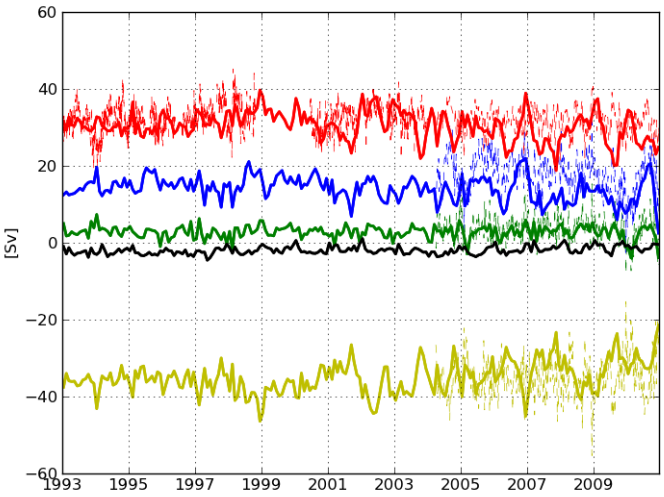

Figure 23: Contributions to the AMOC transport (Sv) at 26.5°N. Black line: total transport from the GEOS ODAS5.2 analysis; solid red line: analysis estimate of Florida Strait transport; dashed red line: cable measurement of Florida Strait transport; solid green line: analysis Ekman transport; dashed green line: Ekman transport estimated using CCMP winds; solid gold line: analysis estimate of mid-ocean transport; dashed gold line: mid-ocean transport from the RAPID array. The blue lines show the maximum AMOC transport, with the solid line from the analysis and the dashed line from the RAPID array.

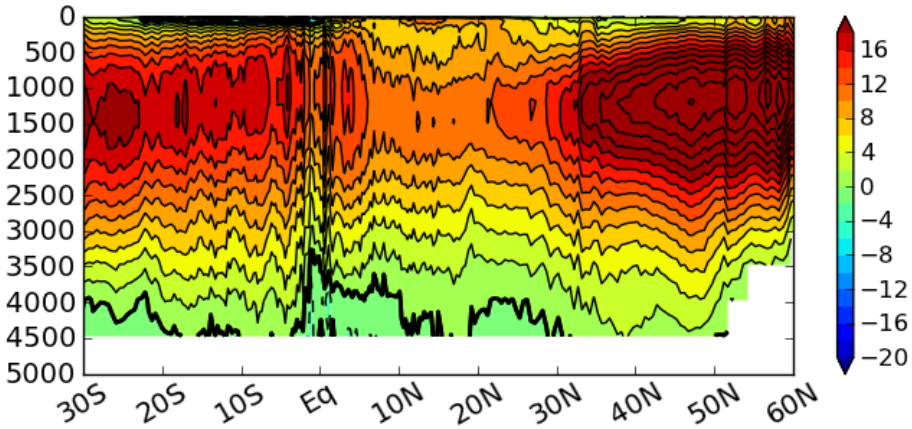

Figure 24: The Eulerian mean meridional overturning circulation in the Atlantic (in Sv). The contour interval is 2 Sv.

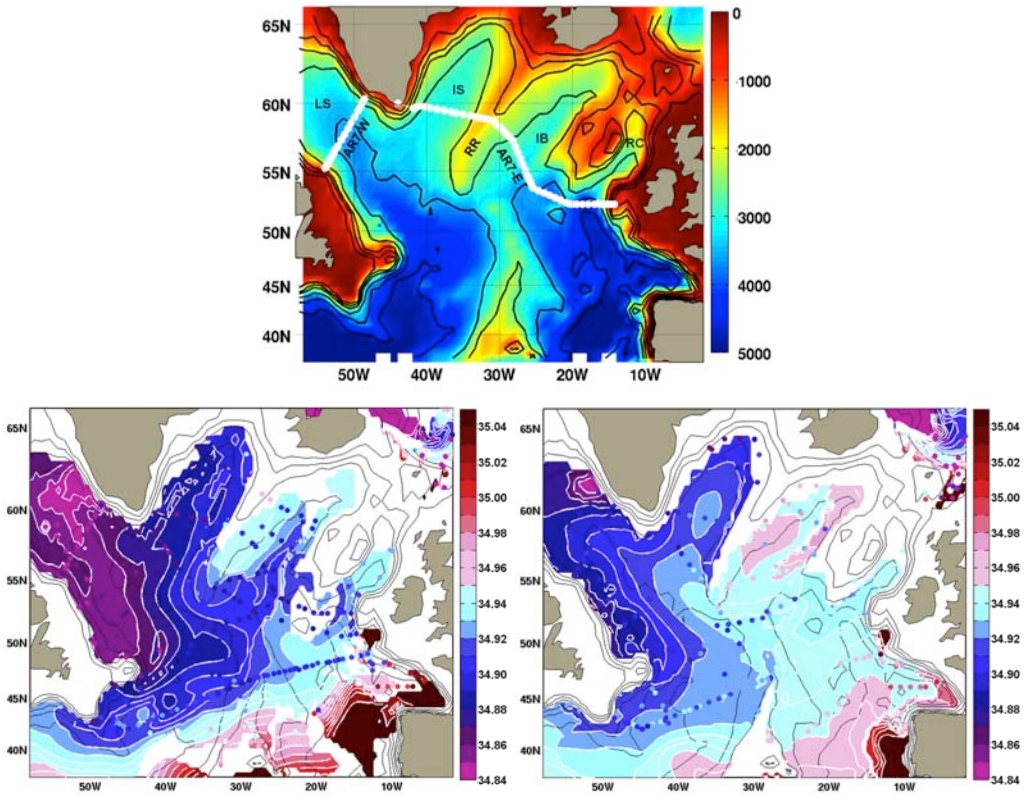

Figure 25: Upper panel: Bottom topography in the subpolar North Atlantic, showing the Labrador Sea (LS), the Irminger Sea (IS), the Icelandic Basin (IB), and the Reykjanes Ridge (RR). Lower panels: The GEOS ODAS5.2 analysis of mean May-June salinity, 1995-1997, in the subpolar North Atlantic. The left panel shows salinity averaged over 36.92 < σ_2 <36.94, the density range for LSW following Yashayaev (2007). The right panel shows salinity on the σ_2 = 37.00 kg m^{-3} surface associated with the NEADW. Salinity observations are over plotted on the GEOS ODAS5.2 analysis.

One of the driving forces of the thermohaline circulation is the formation of deep cold water in the North Atlantic, commonly referred to as North Atlantic Deep Water (NADW). The most

prominent physical process for the formation of the NADW is evaporative cooling of surface water when heat is lost through latent cooling and salt concentration increases through evaporation. The resulting dense water sinks and forms the NADW. Another, less common, process for the formation of NADW is deep convective cooling, which only occurs in places of weak stratification, such as the Greenland and Labrador seas. The representation of Labrador Sea Water (LSW) in the GEOS ocean analyses is of particular importance because it is a principal contributor to the lower limb of the AMOC, which is of interest because of its potential predictability.

Figure 25 shows the mean salinity over the subpolar North Atlantic for May-June 1995-1997 on isopycnal surfaces $36.92 < \sigma_2 < 36.94$ and $\sigma_2 = 37.00$ kg m^{-3}. The former is associated with LSW (potential temperatures < 2.8°C and $S < 34.84$), typically seen at depths of 500-2000 m; the latter represents the high-salinity core of the Northeast Atlantic Deep Water (NEADW), typically seen at 2700-2900 m. During this period the Labrador Sea reached an extreme cold and fresh state and LSW filled the entire central part of the Labrador Sea basin from 500 to 2400 m (Yashayaev 2007).

The salinity analysis within the $36.92 < \sigma_2 < 36.94$ kg m^{-3} volume captures the very fresh water in the Labrador Sea basin, its advection around the southern limb of the subpolar gyre and also into the Deep Western Boundary Current. The freshest water is transported towards the Irminger Sea through the cyclonic recirculation gyre of the central Labrador Basin (Pickart and Spall 2007); however, the analysis is not as fresh as observed.

The analysis at $\sigma_2 = 37.00$ kg m^{-3} is too fresh in the Iceland Basin, but it captures the NEADW fresh water plume that spreads around Reykjanes Ridge and into the Irminger Sea. The NEADW continues to freshen as it continues south along the western boundary of the Labrador Sea. The analysis also captures the strong salinity maximum of the Mediterranean water that spreads north the Iberian Peninsula.

This direct comparison with the observations revealed that, through a technical glitch, not all of the observations in the Irminger Sea were assimilated. This problem has now been rectified in a new (ongoing) analysis.

Deep convective cooling in the Labrador Sea was also observed in 2008 when observations were available from Argo. The resulting ocean structure is illustrated in Figure 26, which shows the horizontal distribution of temperature and salinity of the intermediate water (750 m). The major convection area (central Labrador Sea) is associated with the lowest temperatures and salinities, while the minor convection area (central Irminger Sea) has the highest values. The GEOS ODAS5.2 analysis captures both major and minor convection areas seen in the observations.

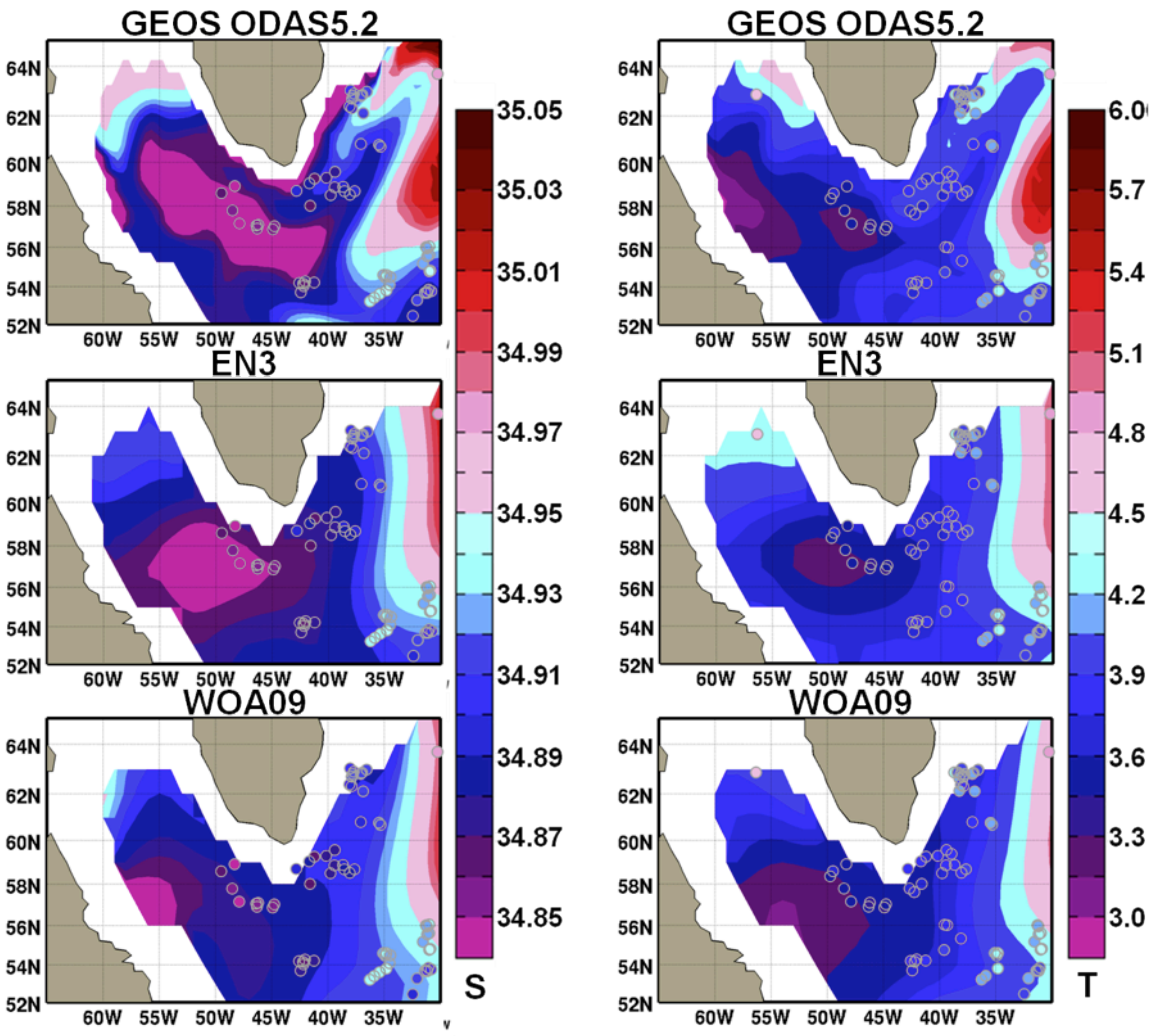

Figure 26: Salinity (left) and potential temperature (right) at 750 m, averaged from February to April 2008, in the subpolar North Atlantic. Observations of T and S from Argo floats are over plotted on the GEOS ODAS analysis in the upper panels.

6.5 Zonal currents along the equatorial Pacific

Comparisons of the analyzed zonal currents with those from the Acoustic Doppler Current Profiler (ADCP) on the TAO moorings along the equatorial Pacific are shown in Figure 27. The climatologies are calculated from 1997 to 2005.

Although no current data are assimilated in the system, the analyses represent the vertical structure and the annual cycle of the currents across the equatorial Pacific very well. The largest discrepancies are in the western Pacific where the Equatorial Undercurrent (EUC) core is too shallow, the analyzed zonal current is too diffuse below the core of the EUC and the intensity is too weak in the boreal winter. The RMS differences reach 0.4 m/s near the surface at 165°E primarily because the analyzed undercurrent does not surface in boreal spring as observed. The structure of the mean bias is similar at all mooring locations, having a westward flow that is too weak near the surface in the South Equatorial Current and eastward flow that is too weak in the EUC. The RMS error in the central and eastern Pacific is about 0.2 m/s.

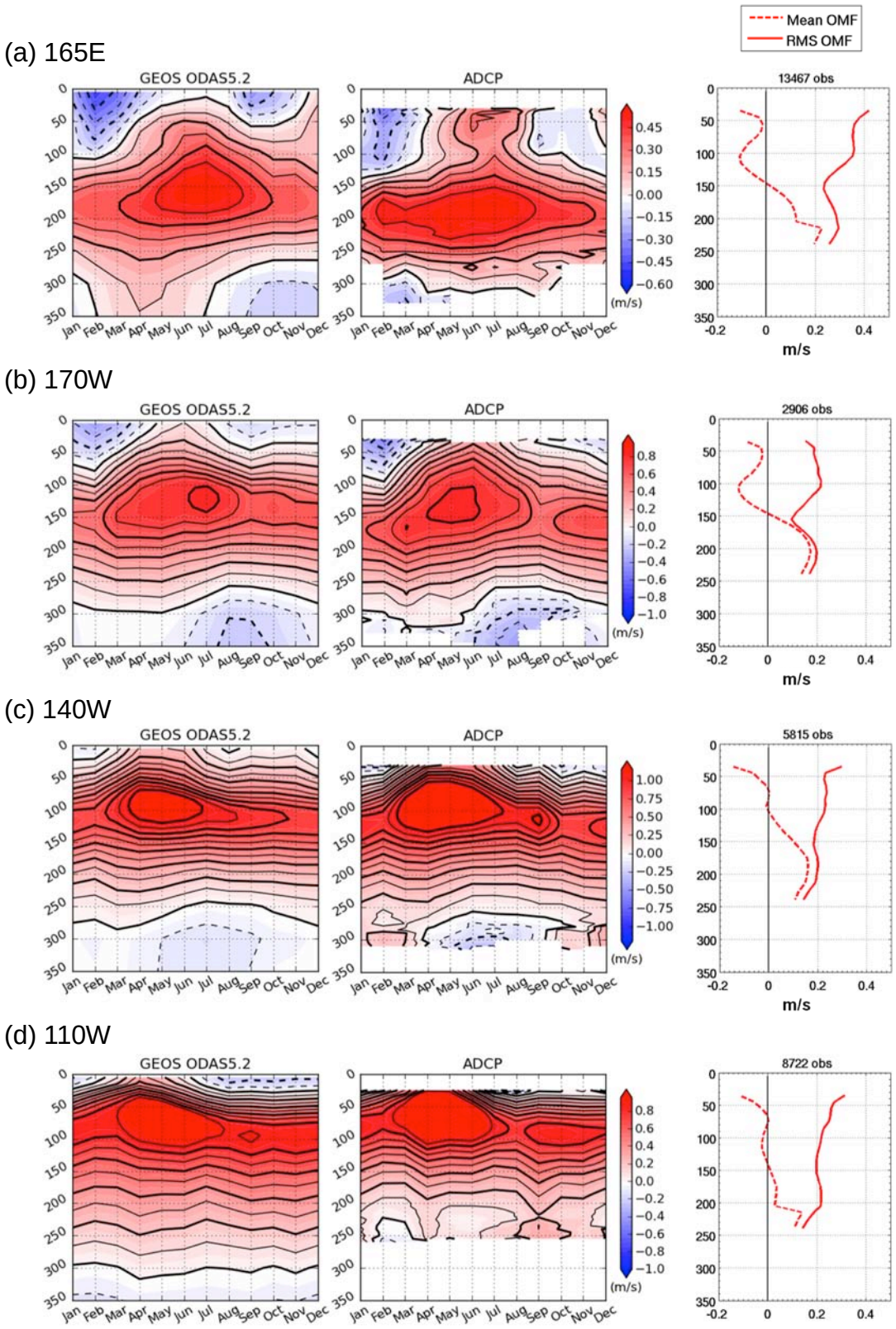

Figure 27: The climatology of zonal currents (m/s) from ODAS5.2 and the ADCP on the TAO moorings on the equator. The climatology is calculated for the period of 1997-2005. The rightmost panels show the mean and RMS of OMFs for each mooring.

6.6 Water masses

The assimilation procedure, using a sequential approach that has a weak constraint to the WOA09 climatology prior to the Argo period and assimilates *T* and *S* profile information last in the cycle, appears to be effective in maintaining the observed water mass distributions. The *T-S* relationships are tighter in the Argo period; and prior to the Argo period, the analysis has a tendency to include slightly fresher waters than in the WOA09 climatology, especially in the Equatorial Pacific and Indian Oceans (Figures 28a and b). At higher latitudes (Figures 29 and 30), the analysis, well constrained by Argo, preserves the water masses in the WOA09 climatology and in the observations plotted in Talley (2008).

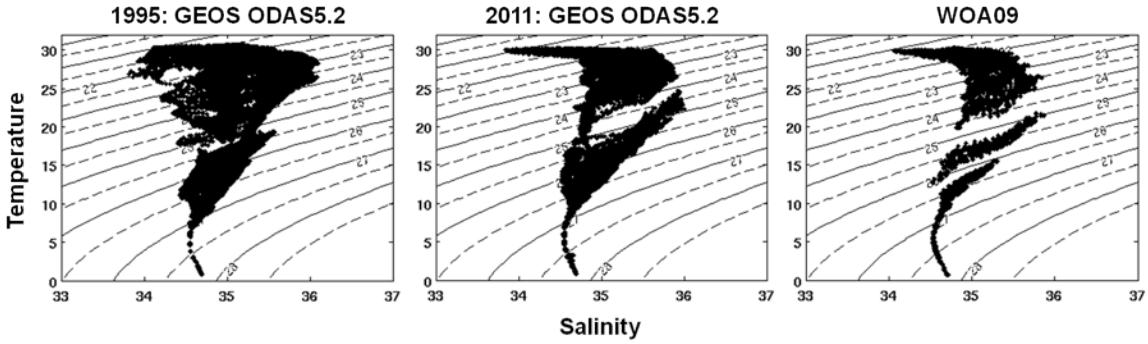

Figure 28a: The T-S pairs in the western equatorial Pacific, 165-170°E, 5°S-5°N, from a pre-Argo year (1995), a post-Argo year (2011) and the WOA09. Profiles are over laid on contours of σ_0 (kg m^{-3}). Monthly mean analysis output is subsampled to the same vertical grid as WOA09.

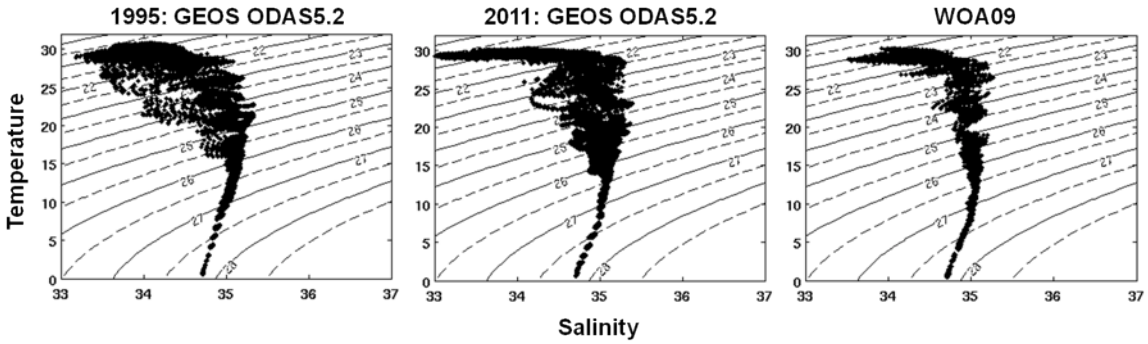

Figure 28b: As for Figure 22a, but for the equatorial Indian Ocean, 88.5-92.5°E, 0-5°N.

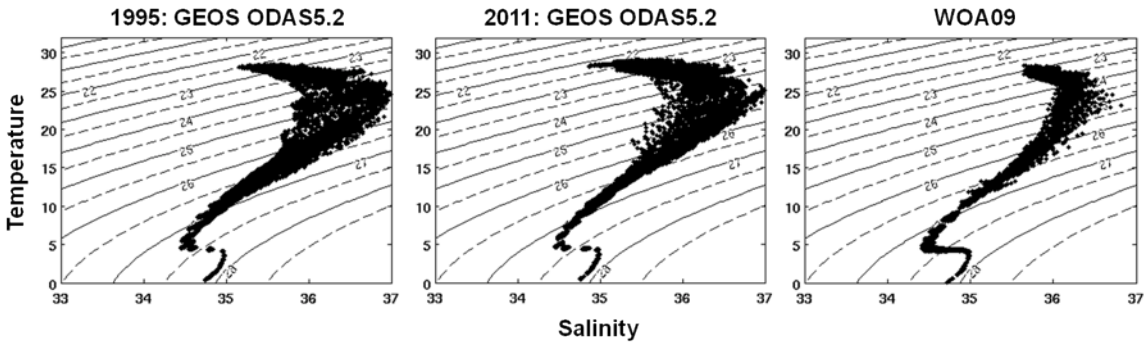

Figure 28c: As for Figure 22a, but for the equatorial Atlantic Ocean, 37.5-33.5°W, 2.5°S-2.5°N.

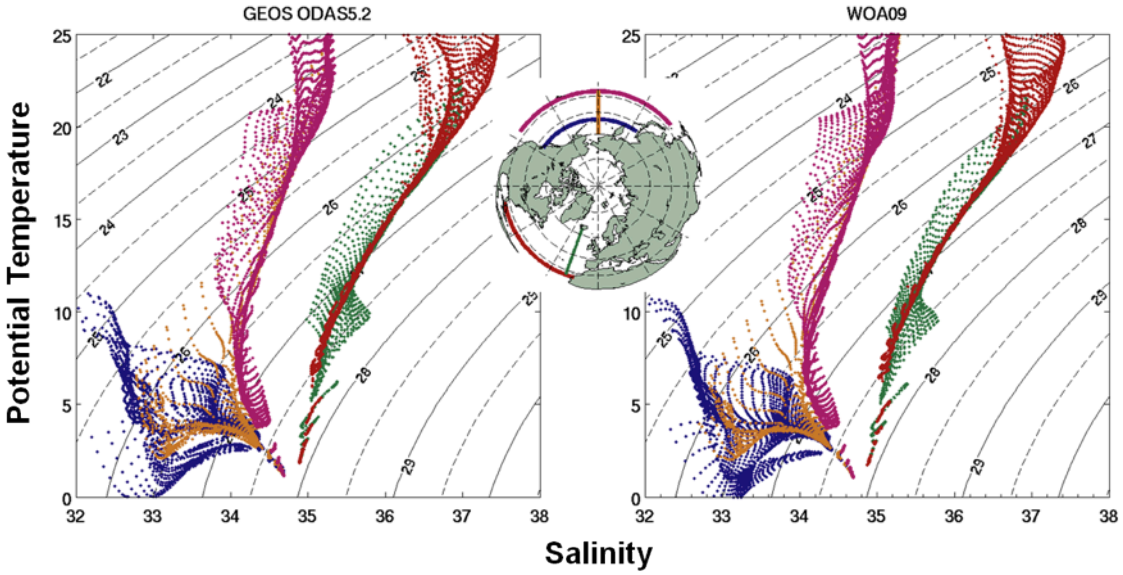

Figure 29: The T-S pairs from profiles at 24°N, for zonal sections bracketing the Arctic in the Pacific sector, and for meridional sections through the northern subtropics and subpolar regions, following Talley (2008). Profiles are over laid on contours of σ_0 (kg m^{-3}). Monthly mean analysis output is subsampled to the same vertical grid as WOA09.

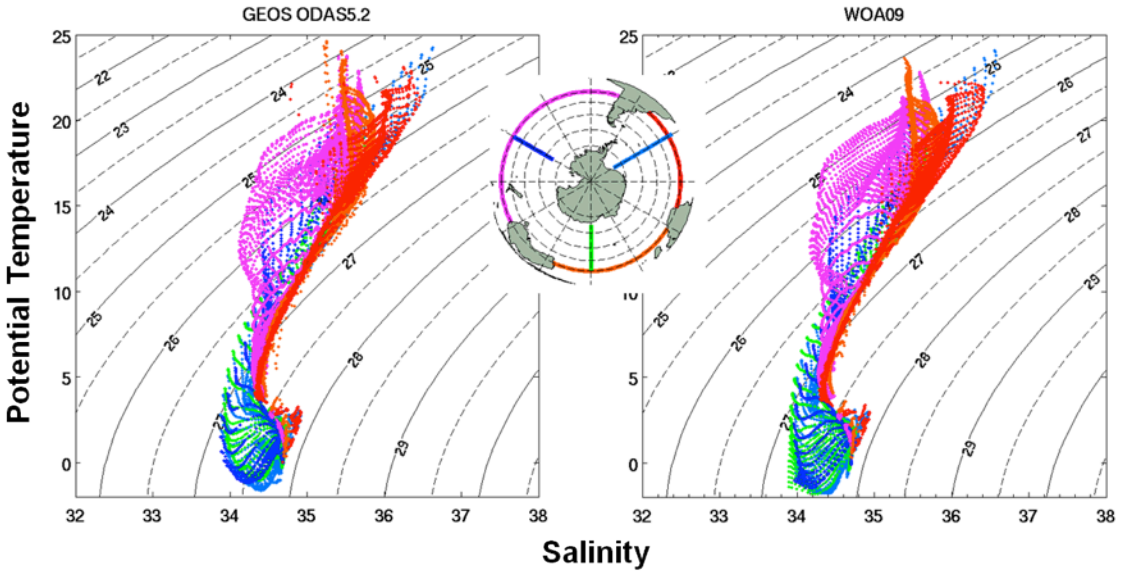

Figure 30: As for Figure 29, except for profiles at 30°S, and for meridional sections southward from that section, following Talley (2008).

7 Summary

We have presented the technical setup, the system evolution, and some results from the GEOS iODAS that uses MOM4 and is constrained by atmospheric forcing from MERRA. Comparisons of the upper ocean heat content from the ocean reanalysis with other ocean analyses (e.g., Xue et al. 2012) has helped to verify the quality of the analysis. Other, more comprehensive, comparisons are underway under the auspices of the Global Ocean Data Assimilation Experiment (GODAE) and the CLIVAR Global Synthesis and Observations Panel (GSOP).

The Appendix presents an atlas of the 2002-2011 *T* and *S* climatologies from GEOS ODAS5.2 and their comparison with WOA09. This analysis, also referred to as MERRA-Ocean, is currently being used to initialize an ensemble of CM1 models for the GMAO's seasonal forecasting efforts.

Acknowledgements

Development of the iODAS was supported by the NASA Modeling, Analysis and Prediction program under WBS 802678.02.17.01.25. Computing resources were provided by the NASA Center for Climate Simulation at the Goddard Space Flight Center. Support from the ocean modeling group at NOAA's Geophysical Fluid Dynamics Laboratory in the setup of MOM4 is gratefully acknowledged. Argo data were collected and made freely available by the International Argo Program and the national programs that contribute to it. (http://www.argo.ucsd.edu, http://argo.jcommops.org). The Argo Program is part of the Global Ocean Observing System. The altimeter products were produced by Ssalto/Duacs and distributed by AVISO, with support from CNES (http://www.aviso.oceanobs.com/duacs/). TAO/TRITON, PIRATA and RAMA data were made available from the TAO Project Office of NOAA/PMEL. Data from the RAPID-WATCH MOC monitoring project are funded by the Natural Environment Research Council and are freely available from www.noc.soton.ac.uk/rapidmoc. The Florida Current cable data are made freely available by NOAA's Atlantic Oceanographic and Meteorological Laboratory (http://www.aoml.noaa.gov/phod/floridacurrent/) and are funded by the NOAA Office of Climate Observations. ETOPO5 data was made available through the Data Announcement 88-MGG-02, Digital relief of the Surface of the Earth from NOAA, National Geophysical Data Center, Boulder, Colorado, 1988. Finally, we gratefully acknowledge the support from GMAO colleagues – Max Suarez, Jossy Jacob, Yury Vikhliaev, Bin Zhao, and Atanas Trayanov – in configuration of the GEOS-5 AOGCM, implementation of ESMF interfaces, and tests and modifications of the system.

References

Antonov, J.I. and coauthors, 2010: World Ocean Atlas 2009, Volume 2: Salinity., S. Levitus, Ed. NOAA Atlas NESDIS 69, U.S. Government Printing Office, Washington, D.C., 184 pp.

Bennett, A.F., 1992: Inverse Methods in Physical Oceanography, Cambridge University Press, New York, NY, 1992.

Bennett, A.F., B.S. Chua, D.E. Harrison, and M.J. McPhaden, 1998: Generalized Inversion of Tropical Atmosphere–Ocean Data and a Coupled Model of the Tropical Pacific. *J. Climate*, **11**, 1768-1792.

Eliassen, A., 1954: Provisional report on calculation of spatial covariance and autocorrelation of the pressure field. Report 5. Videnskaps Akademiet Institut for Vaer Og Klimaforskning, Oslo, Norway, 12pp.

Gaspari, G., and S.E. Cohn, 1999: Construction of correlation functions in two and three dimensions. *Quart. J. Roy. Meteor. Soc.*, **125B**, 723-757.

Griffies, S.M. and coauthors, 2005: Formulation of an ocean model for global climate simulations. *Ocean Science*, **1**, 45-79.

Ham, Y.-G., M.M. Rienecker, M.J. Suarez, Y. Vikhliaev, B. Zhao, J. Marshak, G. Vernieres, and S.D. Schubert, 2012: Decadal prediction skill in the GEOS-5 forecast system. *Clim. Dyn. (in revision).*

Hunke, E.C., and W.H. Lipscomb, 2008: CICE: The Los Alamos Sea Ice Model, Documentation and Software Manual, Version 4.0. Technical Report, Los Alamos National Laboratory.

Hurrell, J.W., J.J. Hack, D. Shea, J.M. Caron, and J. Rosinski, 2008: A new sea surface temperature and sea ice boundary dataset for the Community Atmosphere Model. *J. Climate*, **21**, 5145–5153. doi: http://dx.doi.org/10.1175/2008JCLI2292.1.

Ingleby, B., and M. Huddleston, 2007: Quality control of ocean temperature and salinity profiles - historical and real-time data. *J. Mar. Syst.*, **65**, 158-175 10.1016/j.jmarsys.2005.11.019.

Keppenne, C.L., R. Kovach, M.M. Rienecker, and G. Vernieres, 2013: Ensemble Data Assimilation without Ensembles: Methodology and Application to Ocean Data Assimilation. (*draft ms).*

Kimeldorf, G.S., and G. Wahba, 1970: A correspondence between Bayesian estimation on stochastic processes and smoothing by splines. *Ann. Math. Stat.*, **41** (2), 495–502.

Leuliette, E.W., and J.K. Willis, 2011: Balancing the sea level budget. *Oceanography,* **24**(2), 122–129, doi:10.5670/oceanog.2011.32.

Levitus, S., J. I. Antonov, T. P. Boyer, R. A. Locarnini, H. E. Garcia, and A. V. Mishonov, 2009: Global ocean heat content 1955–2008 in light of recently revealed instrumentation problems. *Geophys. Res. Lett.*, **36**, L07608, doi:10.1029/2008GL037155.

Locarnini, R.A., A.V. Mishonov, J.I. Antonov, T.P. Boyer, H.E. Garcia, O.K. Baranova, M.M. Zweng, and D.R. Johnson, 2010: World Ocean Atlas 2009, Volume 1: Temperature. S. Levitus, Ed. NOAA Atlas NESDIS 68, U.S. Government Printing Office, Washington, D.C., 184 pp.

McPhaden, M. and coauthors, 2010: The Global Tropical Moored Buoy Array *in* Proceedings of OceanObs'09: Sustained Ocean Observations and Information for Society (Vol. 2), Venice, Italy, 21-25 September 2009, Hall, J., Harrison, D.E. & Stammer, D., Eds., ESA Publication WPP-306, doi:10.5270/OceanObs09.cwp.61.

Molod, A., L. Takacs, M. Suarez, J. Bacmeister, I.-S. Song, and A. Eichmann, 2012: The GEOS-5 Atmospheric general circulation model: Mean climate and development from MERRA to Fortuna. *NASA Technical Report Series on Global Modeling and Data Assimilation*, NASA/TM-2012-104606, Vol. **28**, 117 pp.

Oke, P.R., G.B. Brassington, D.A. Griffin, and A. Schiller, 2010: Ocean data assimilation: a case for ensemble optimal interpolation. *Aust. Meteorolog. & Oceanogr. J.*, **59**, 67-76.

Pickart, R.S., and M.A. Spall, 2007: Impact of Labrador Sea convection on the North Atlantic meridional overturning circulation. *J. Phys. Oceanogr.*, **37**, 2207-2227.

Rayner, D., and co-authors, 2011: Monitoring the Atlantic meridional overturning circulation. *Deep-Sea Research II*, **58**, 1744-1753, doi:10.1016/j.dsr2.2010.10.056.

Reichle, R.H., R.D. Koster, G.J.M. De Lannoy, B.A. Forman, Q. Liu, S. Mahanama, and A. Toure, 2011. Assessment and enhancement of MERRA land surface hydrology estimates. *J. Climate*, **24**, 6322-6338. doi:10.1175/JCLI-D-10-05033.

Reynolds R.W., T.M. Smith, C. Liu, D.B. Chelton, K.S. Casey, and M.G. Schlax, 2007: Daily high-resolution blended analyses for sea surface temperature. *J. Climate*, **20**, 5473-5496.

Rienecker, M.M. and coauthors, 2008: The GEOS-5 Data Assimilation System – Documentation of Versions 5.0.1, 5.1.0, and 5.2.0. *NASA Technical Report Series on Global Modeling and Data Assimilation*, NASA/TM-2008-104606, Vol. **28**, 101 pp.

Rienecker, M.M., and coauthors, 2011: MERRA - NASA's Modern-Era Retrospective Analysis for Research and Applications. *J. Climate*, **24**, 3624-3648. doi: 10.1175/JCLI-D-11-00015.1.

Talley, L.D., 2008: Freshwater transport estimates and the global overturning circulation: Shallow, deep and throughflow components. *Prog. Oceanogr.*, **78**, 257–303.

Xue, Y., M. A. Balmaseda , T. Boyer, N. Ferry, S. Good, I. Ishikawa, A. Kumar, M. Rienecker, A. J. Rosati, Y. Yin, 2012: A Comparative Analysis of Upper Ocean Heat Content Variability from an Ensemble of Operational Ocean Reanalyses. *J. Climate*, **25**, 6905-6929.

Yashayaev, I., 2007: Hydrographic changes in the Labrador Sea, 1960–2005. *Prog. Oceanogr.*, **73**, 242-276.

Wan, L., L. Bertino, and J. Zhu, 2010: Assimilating Altimetry Data into a HYCOM Model of the Pacific: Ensemble Optimal Interpolation versus Ensemble Kalman Filter. *J. Atmos. Ocean. Tech.*, **27**, 753-765.

Acronyms

ADCP	Acoustic Doppler Current Profiler
AGCM	Atmospheric General Circulation Model
AMOC	Atlantic Meridional Overturning Circulation
AOGCM	Atmosphere-Ocean General Circulation Model
AVISO	Archiving, Validation and Interpretation of Satellite Oceanographic
CCMP	Cross Calibrated Multi-Platform (winds)
CICE	Sea-ice model developed at Los Alamos National Laboratory
CLIVAR	CLImate VARiability and predictability
CM1(2)	Model Configuration 1 (2)
CMAP	CPC Merged Analysis of Precipitation
CMIP5	Coupled Model Intercomparison Project, Phase 5
CNES	Centre National d'Etudes Spatiales
CPC	Climate Prediction Center (NOAA)
CTD	Conductivity Temperature Depth
DMSP	Defense Meteorological Satellite Program
EN3	U.K. Met Office ocean observations data base
EnKF	Ensemble Kalman Filter
EnOI	Ensemble Optimal Interpolation
ESMF	Earth System Modeling Framework
EUC	Equatorial Undercurrent
GDAC	Global Data Assembly Center
GEOS	Goddard Earth Observing System (model)
GFDL	Geophysical Fluid Dynamics Laboratory
GMAO	Global Modeling and Assimilation Office, Code 610.1, NASA/GSFC
GODAE	Global Ocean Data Assimilation Experiment
GPCP	Global Precipitation Climatology Project
GSFC	Goddard Space Flight Center
GSOP	Global Synthesis and Observations Panel
IB	Icelandic Basin
IESA	Integrated Earth System Analysis
iODAS	integrated Ocean Data Assimilation System
IS	Irminger Sea
LANL	Los Alamos National Laboratory
LS	Labrador Sea
LSM	Land Surface Model
LSW	Labrador Sea Water
MAP	NASA Modeling, Analysis, and Prediction (program)
MDT	Mean Dynamic Topography
MERRA	Modern-Era Retrospective analysis for Research and Applications
MOC	Meridional Overturning Circulation
MOM4	Modular Ocean Model, version 4
NADW	North Atlantic Deep Water
NASA	National Aeronautics and Space Administration
NCCS	NASA Center for Climate Simulation (at NASA/GSFC)
NEADW	Northeast Atlantic Deep Water
NMME	National Multi-Model Ensemble
NOAA	National Oceanographic and Atmospheric Administration
NSIDC	National Snow and Ice Data Center
ODAS	Ocean Data Assimilation System

OI	Optimal Interpolation
OMA	Observation Minus Analysis
OMF	Observation Minus Forecast
PIRATA	Prediction Research moored Array in the Tropical Atlantic
PMEL	Pacific Marine Environmental Laboratory (NOAA)
RAMA	Research moored Array for African–Asian–Australian Monsoon Analysis and prediction
RAPID	Rapid Climate Change programme
RMS	Root Mean Square
RR	Reykjanes Ridge
SAFE	Spatial approximation of Forecast Error
SEC	South Equatorial Current
SLA	Sea Level Anomaly
SMMR	Scanning Multi-channel Microwave Radiometer
SSM/I	Special Sensor Microwave/Imager
SSMI/S	Special Sensor Microwave Imager/Sounder
SST	Sea Surface Temperature
TAO	Tropical Atmosphere Ocean (moored buoy array)
WOA09	World Ocean Atlas 2009
XBT	eXpendable Bathythermograph

Atlas of Climatologies of Selected Fields
from
GEOS ODAS5.2
2002-2011

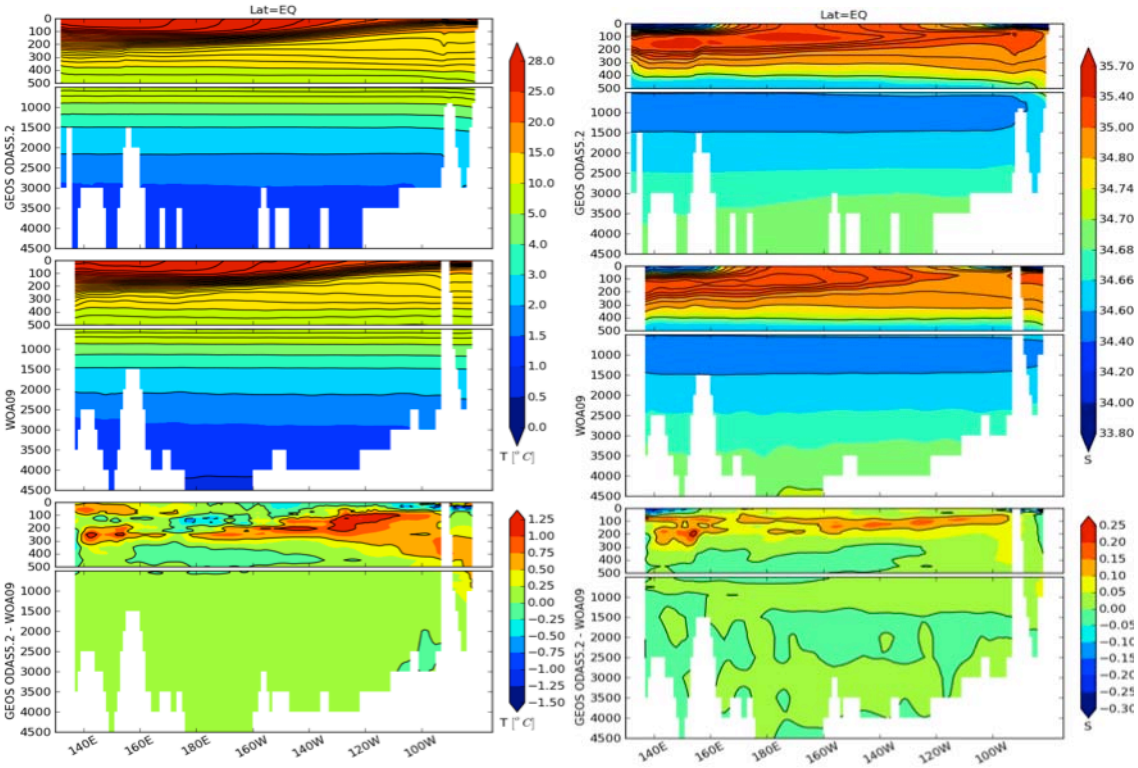

Figure 31: Potential temperature (°C) (left) and salinity (right) sections across the equatorial Pacific. The uppermost panels are from the GEOS ODAS5.2 analysis; the middle panels are from WOA09 and the bottom panels show the differences (ODAS minus WOA09).

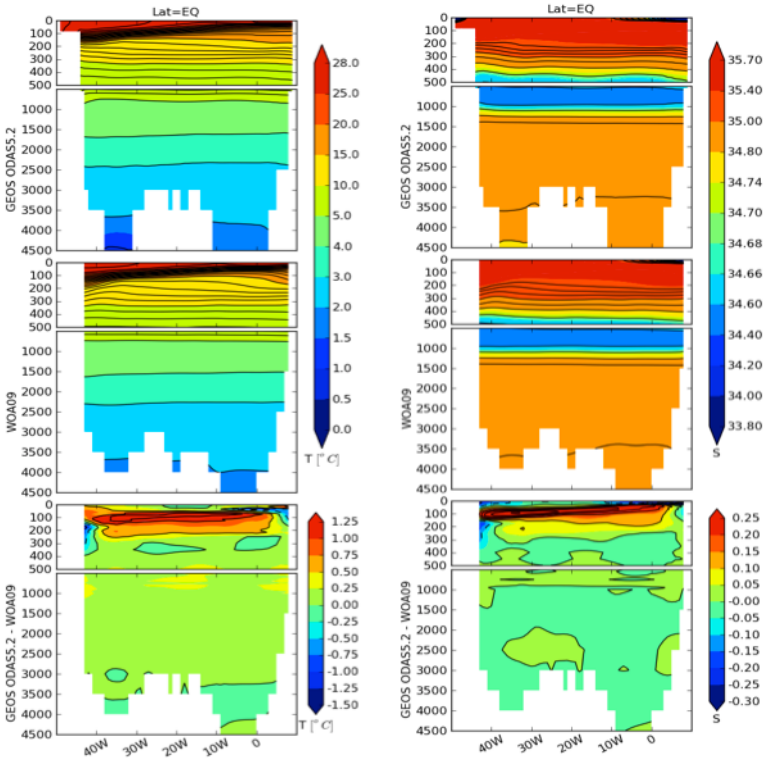

Figure 32: As for Figure 31, but for the equatorial Atlantic Ocean.

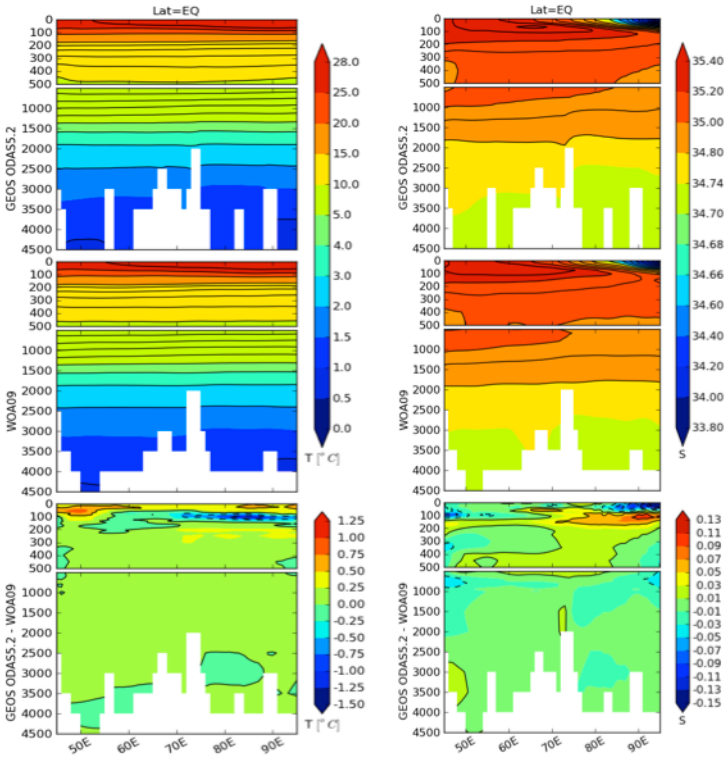

Figure 33: As for Figure 31, but for the equatorial Indian Ocean.

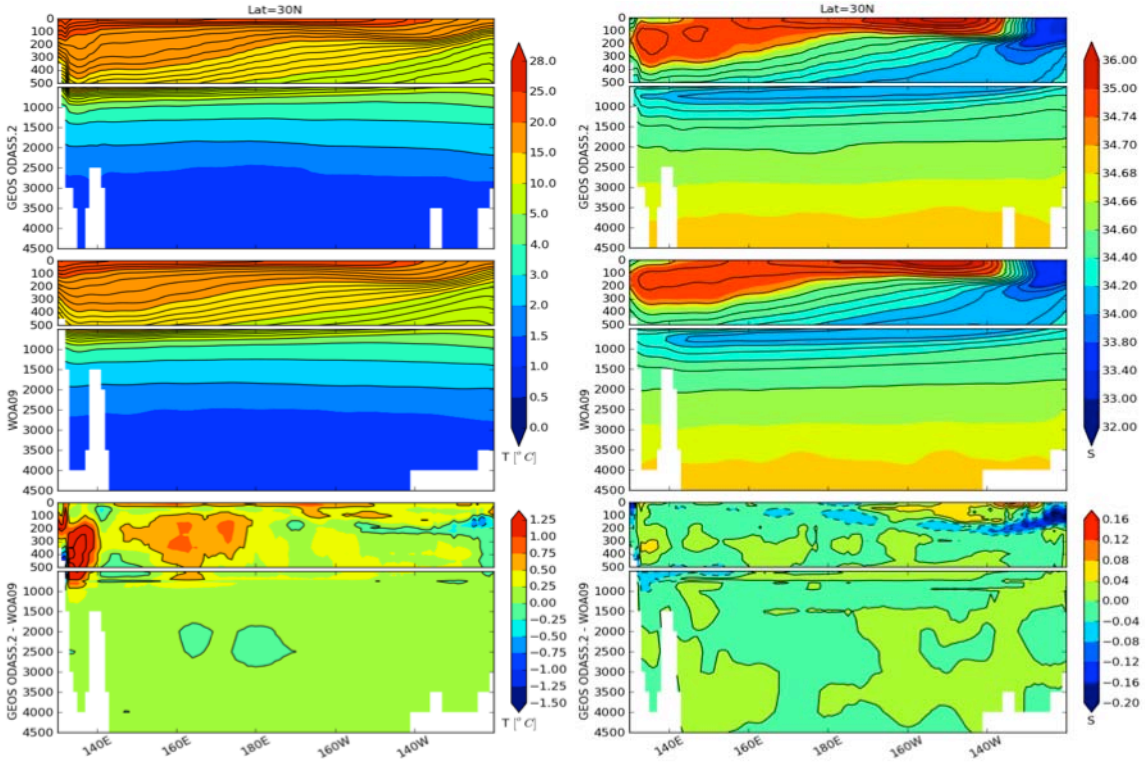

Figure 34: As for Figure 31, but for the 30°N across the Pacific Ocean.

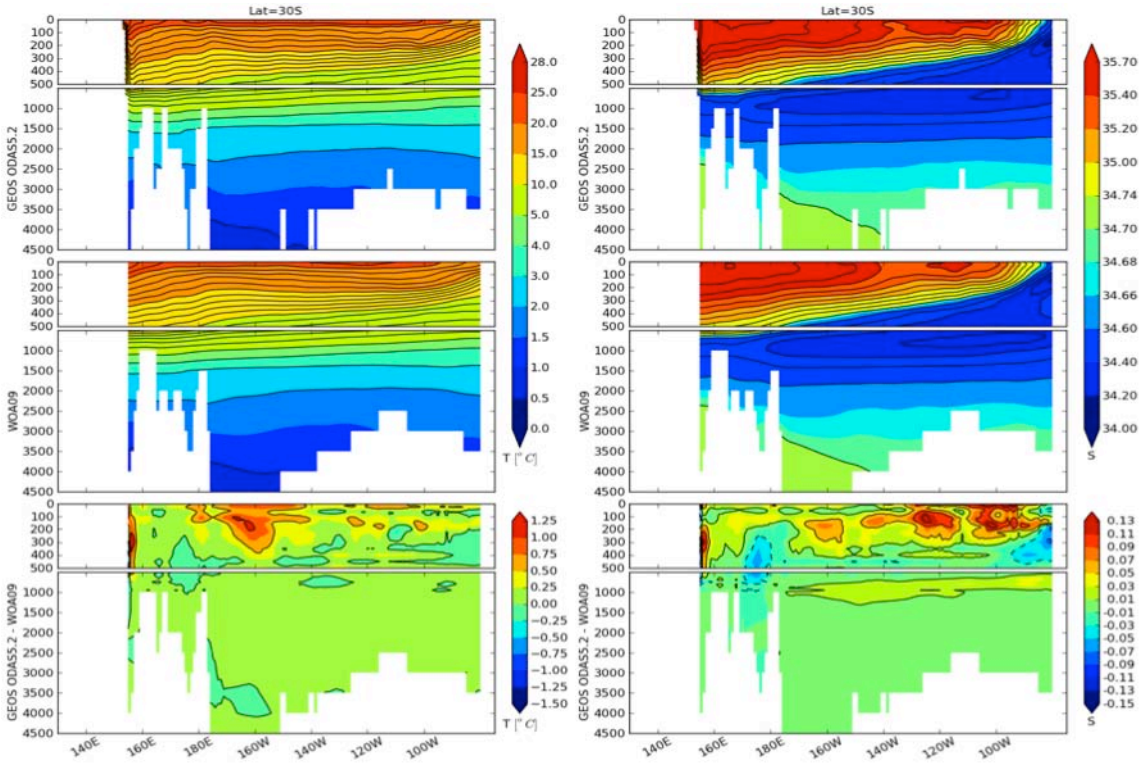

Figure 35: As for Figure 31, but for the 30°S across the Pacific Ocean.

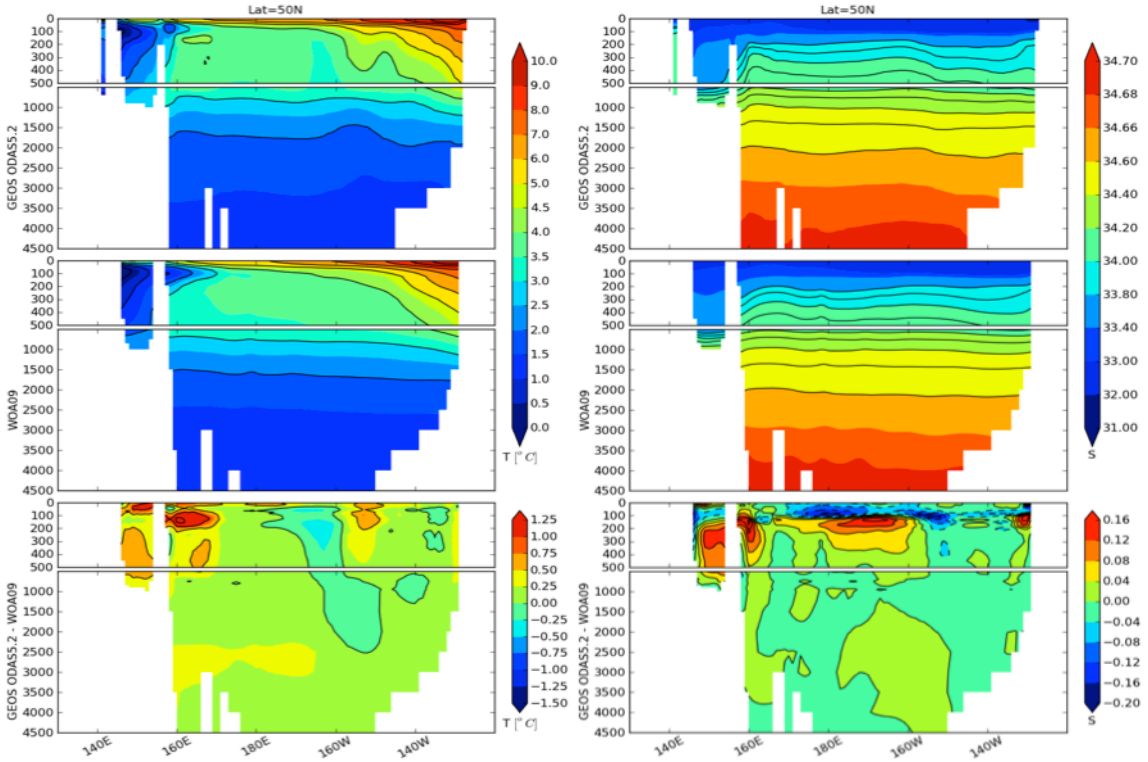

Figure 36: As for Figure 31, but for the 50°N across the Pacific Ocean.

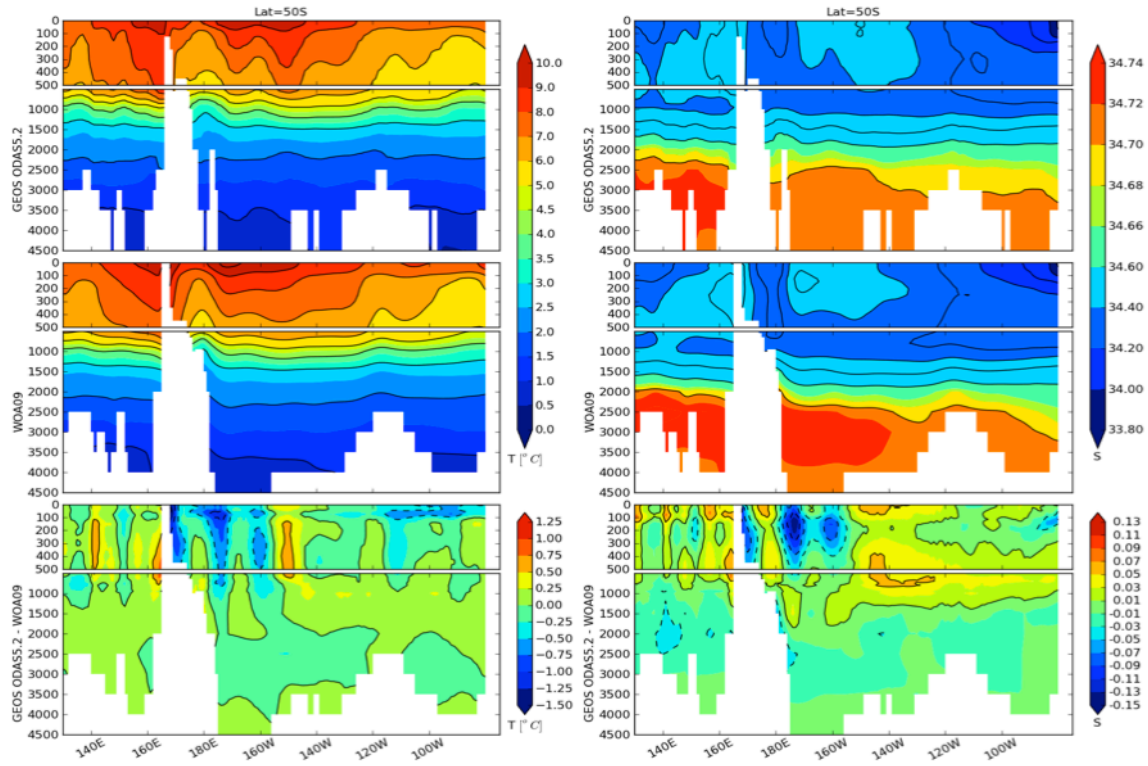

Figure 37: As for Figure 31, but for the 50°S across the Pacific Ocean.

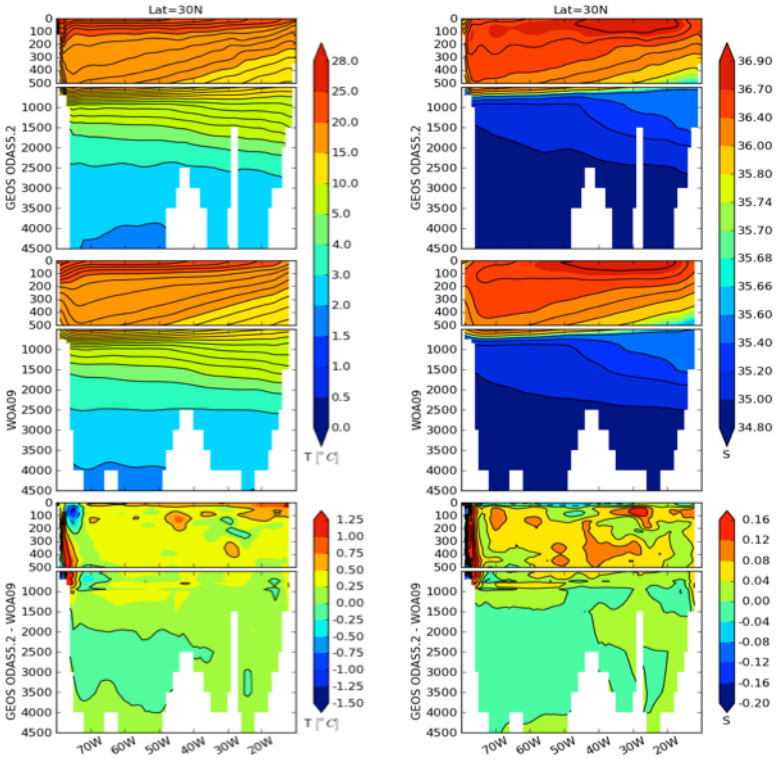

Figure 38: As for Figure 31, but for the 30°N across the Atlantic Ocean.

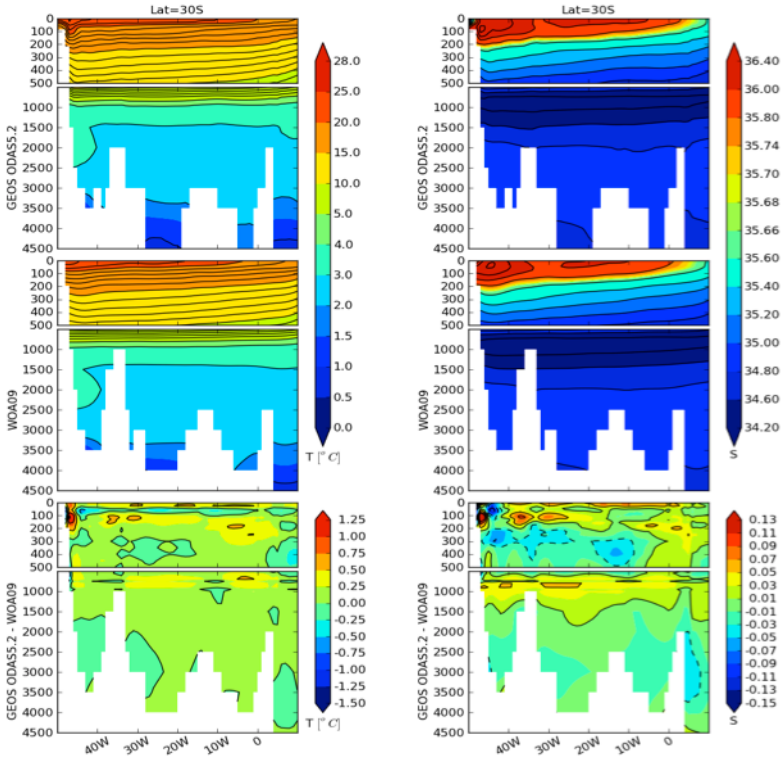

Figure 39: As for Figure 31, but for the 30°S across the Atlantic Ocean.

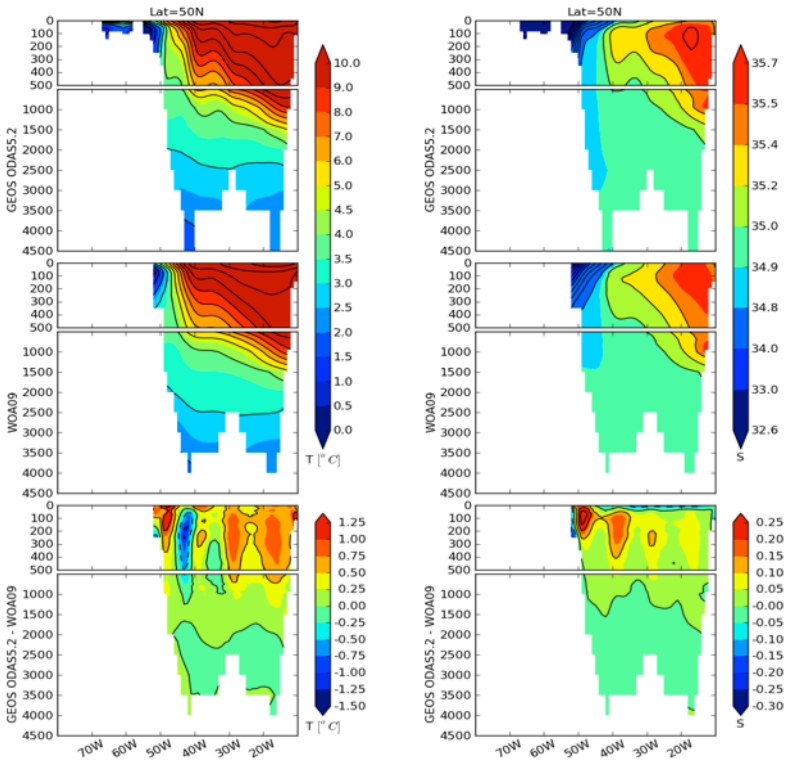

Figure 40: As for Figure 31, but for the 50°N across the Atlantic Ocean.

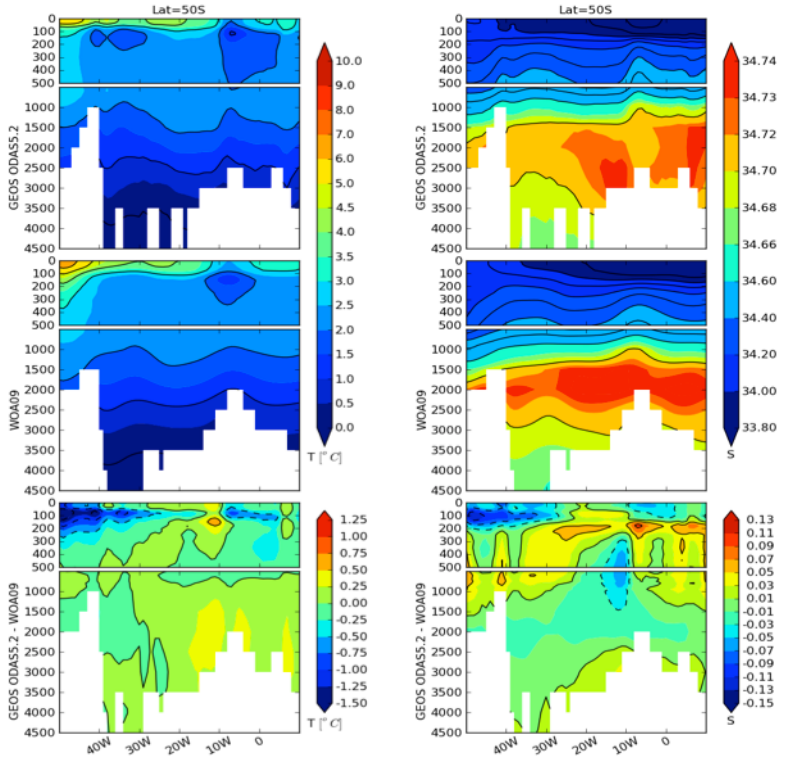

Figure 41: As for Figure 31, but for the 50°S across the Atlantic Ocean.

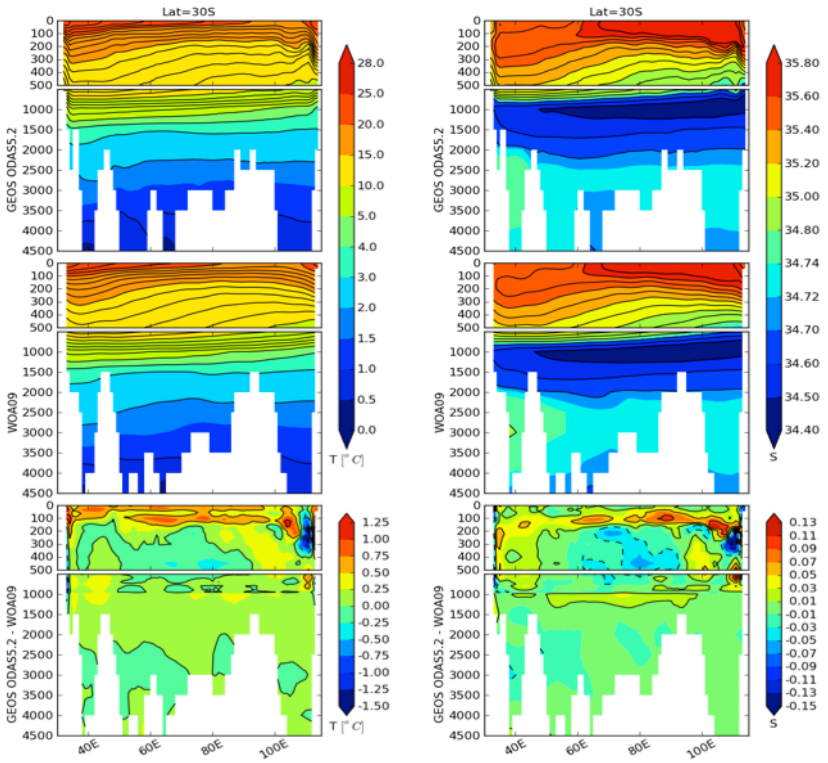

Figure 42: As for Figure 31, but for the 30°S across the Indian Ocean.

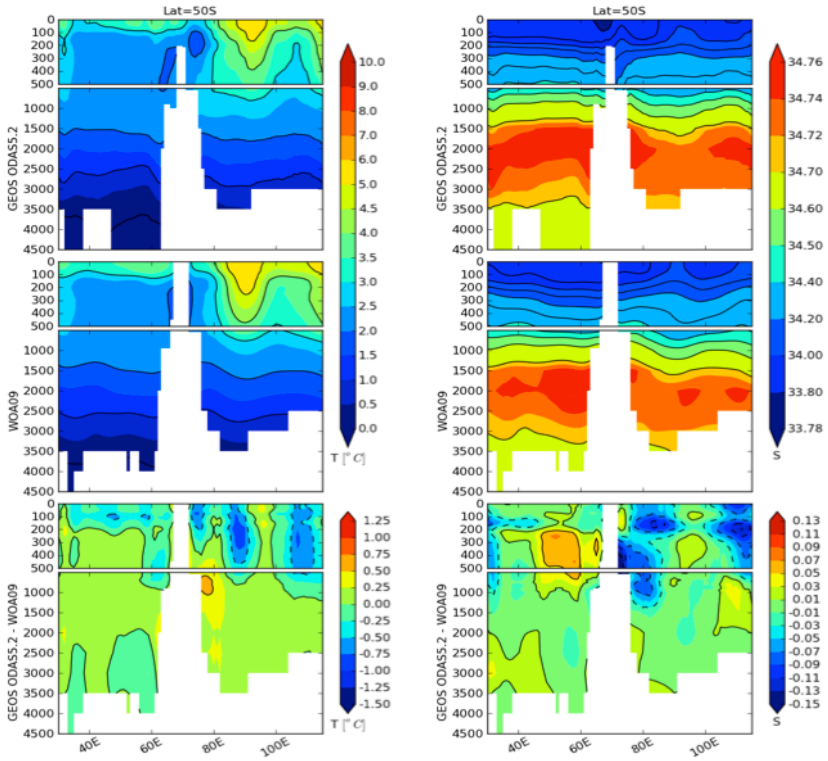

Figure 43: As for Figure 31, but for the 50°S across the Indian Ocean.

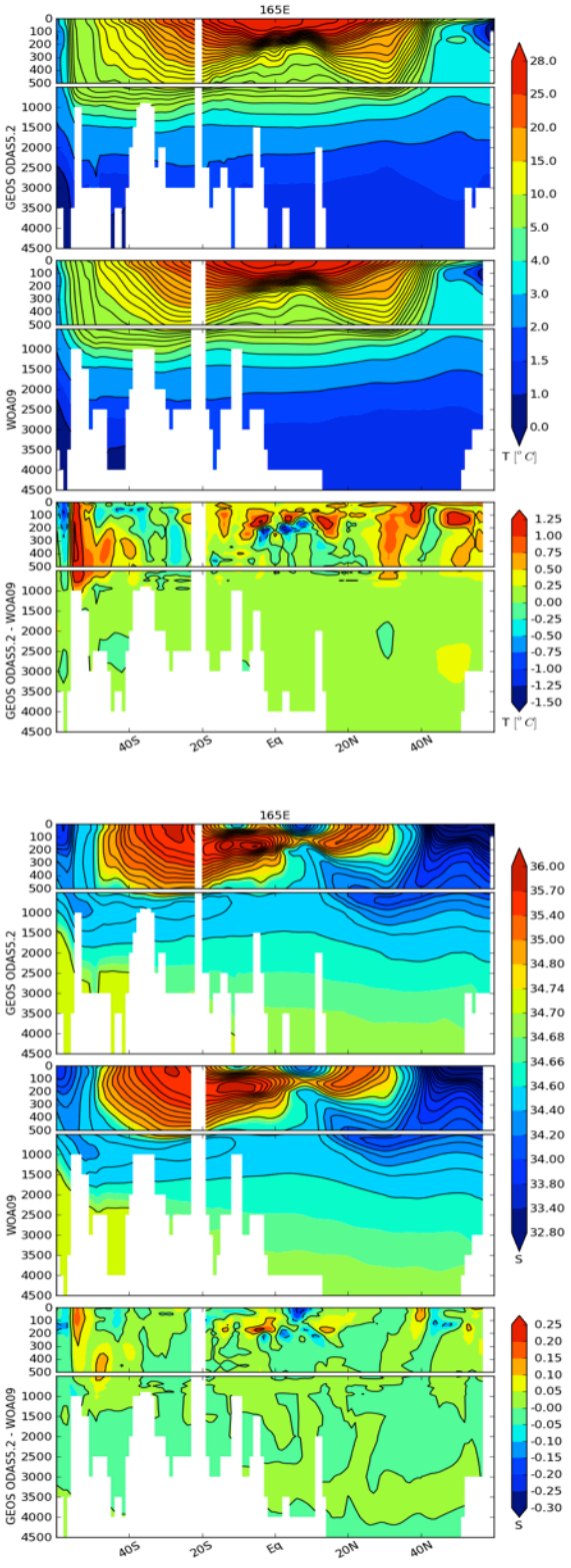

Figure 44: Potential temperature (°C) (upper set) and salinity (lower set) sections along 165°E. The uppermost panel in each set is from the GEOS ODAS5.2 analysis; the middle panel is from WOA09 and the bottom panel shows the difference (ODAS minus WOA09).

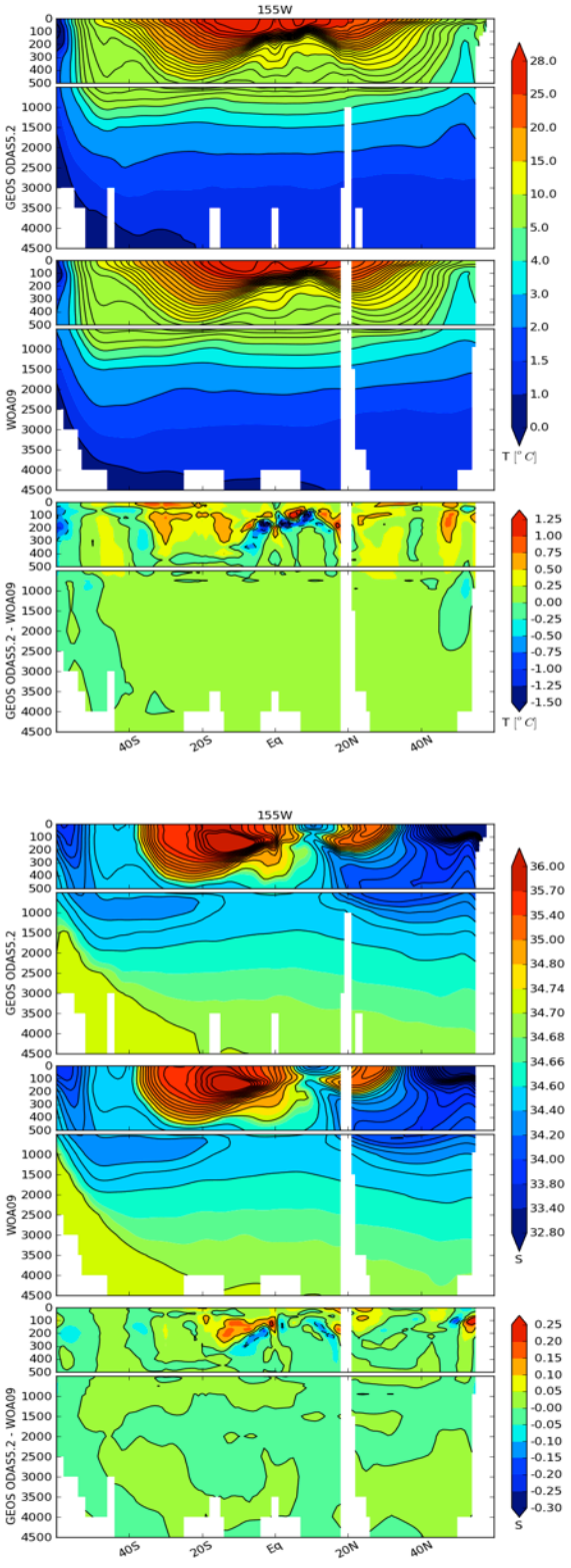

Figure 45: As for Figure 44, but for 155°W.

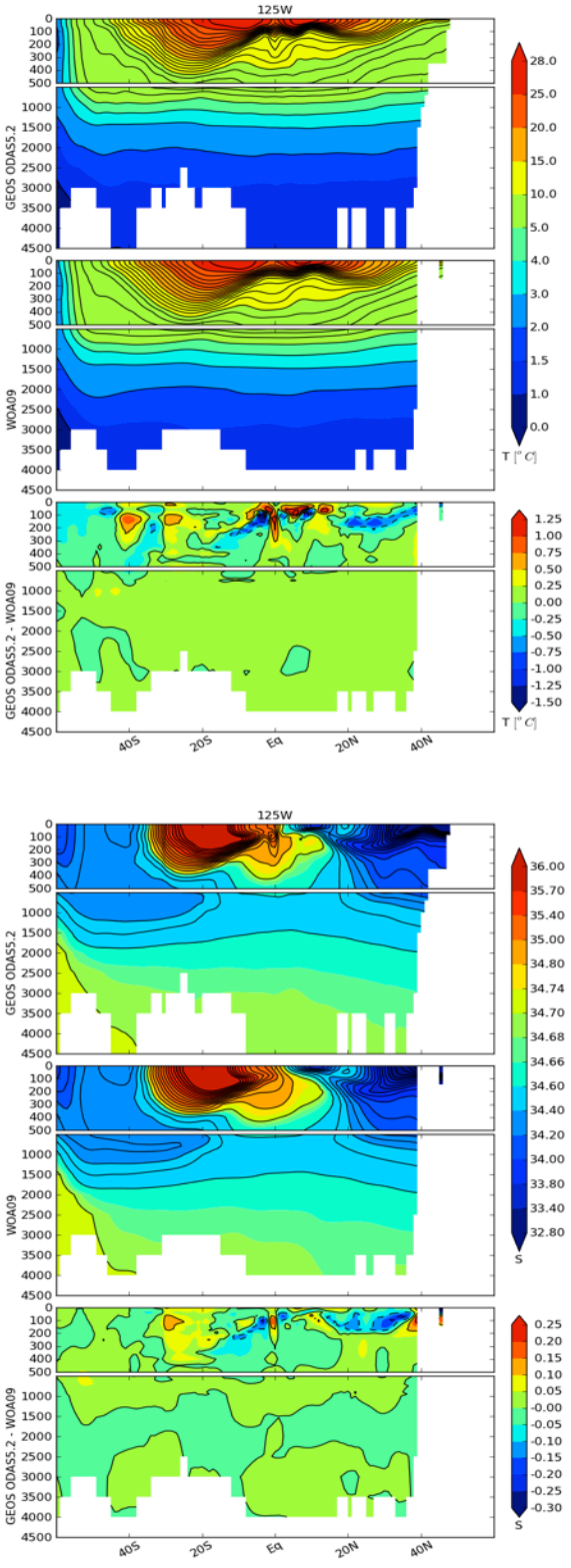

Figure 46: As for Figure 44, but for 125°W.

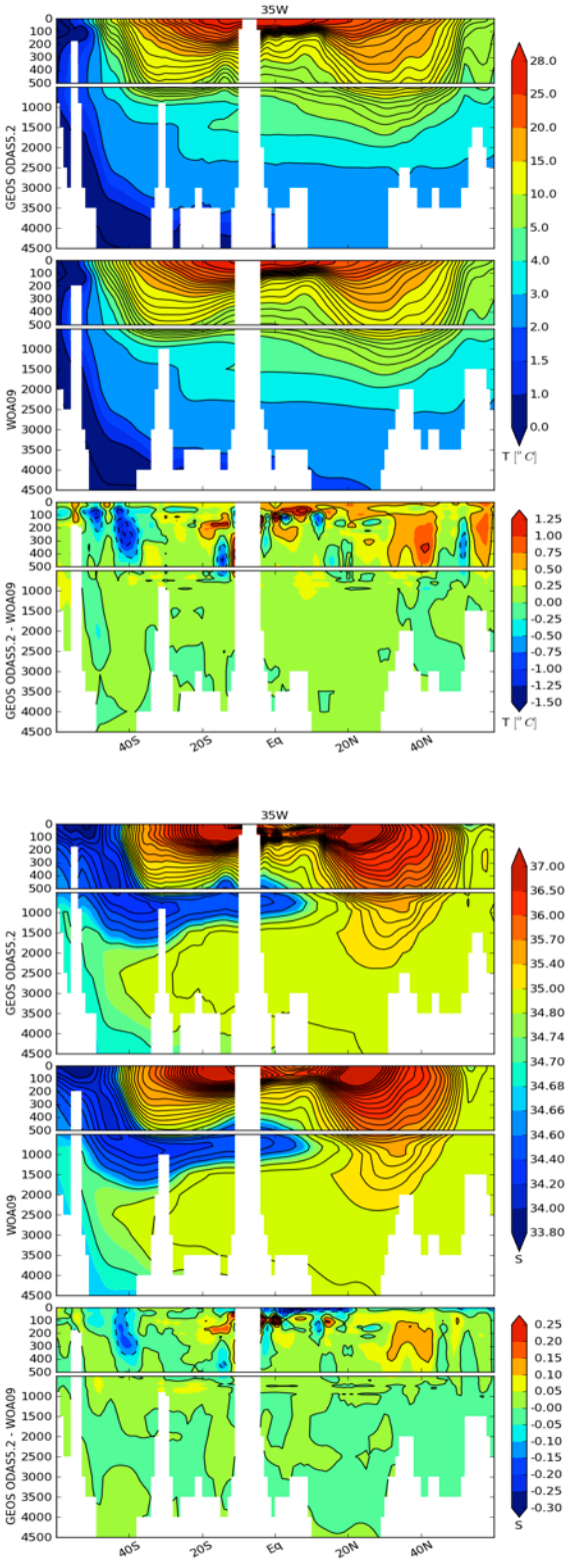

Figure 47: As for Figure 44, but for 35°W.

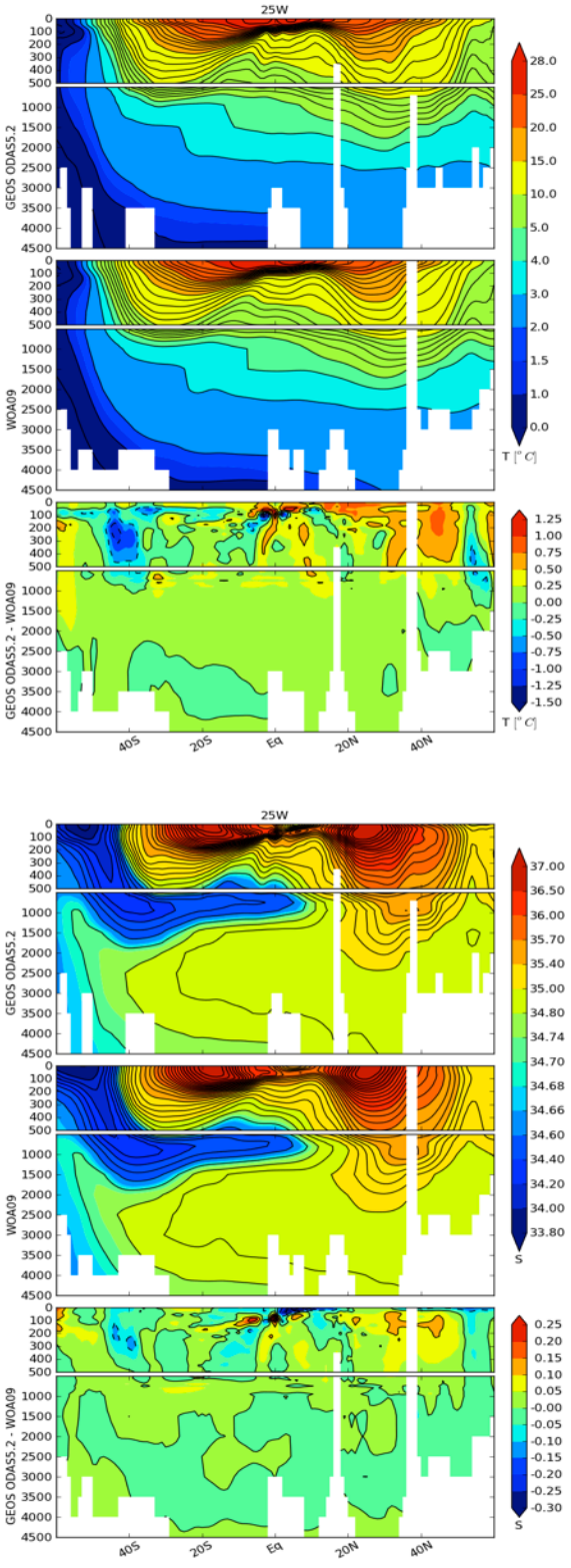

Figure 48: As for Figure 44, but for 25°W.

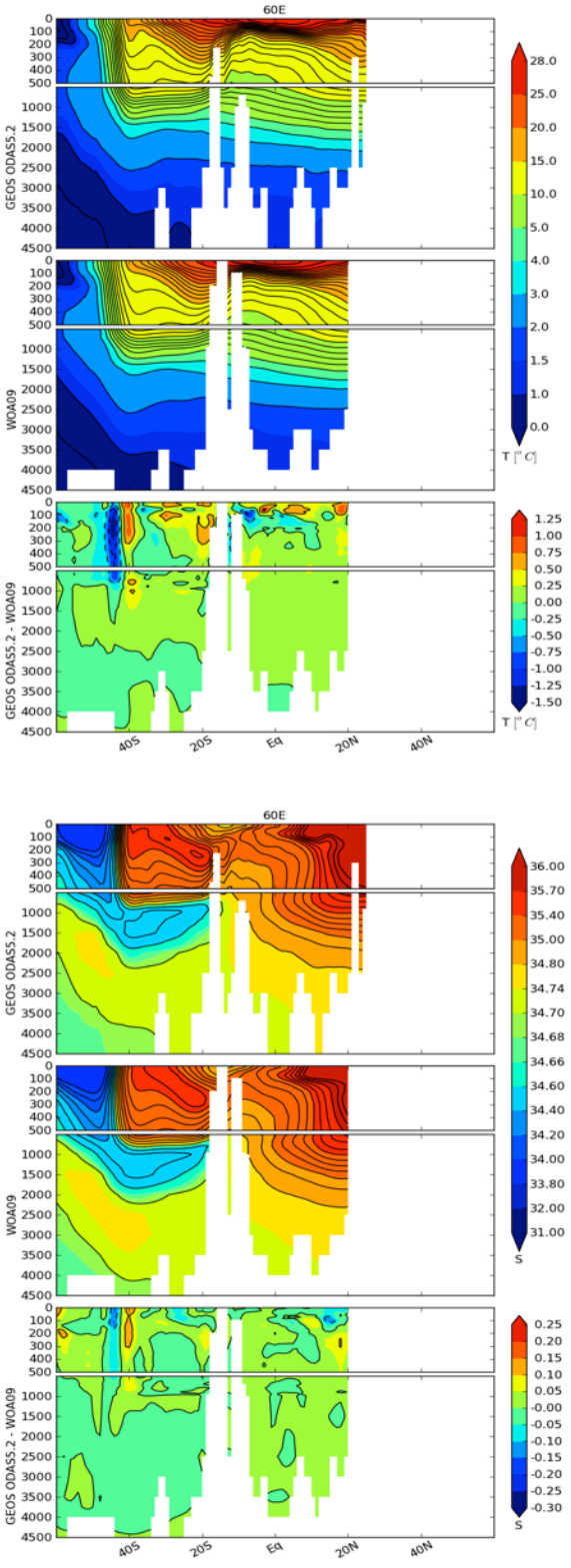

Figure 49: As for Figure 44, but for 60°E.

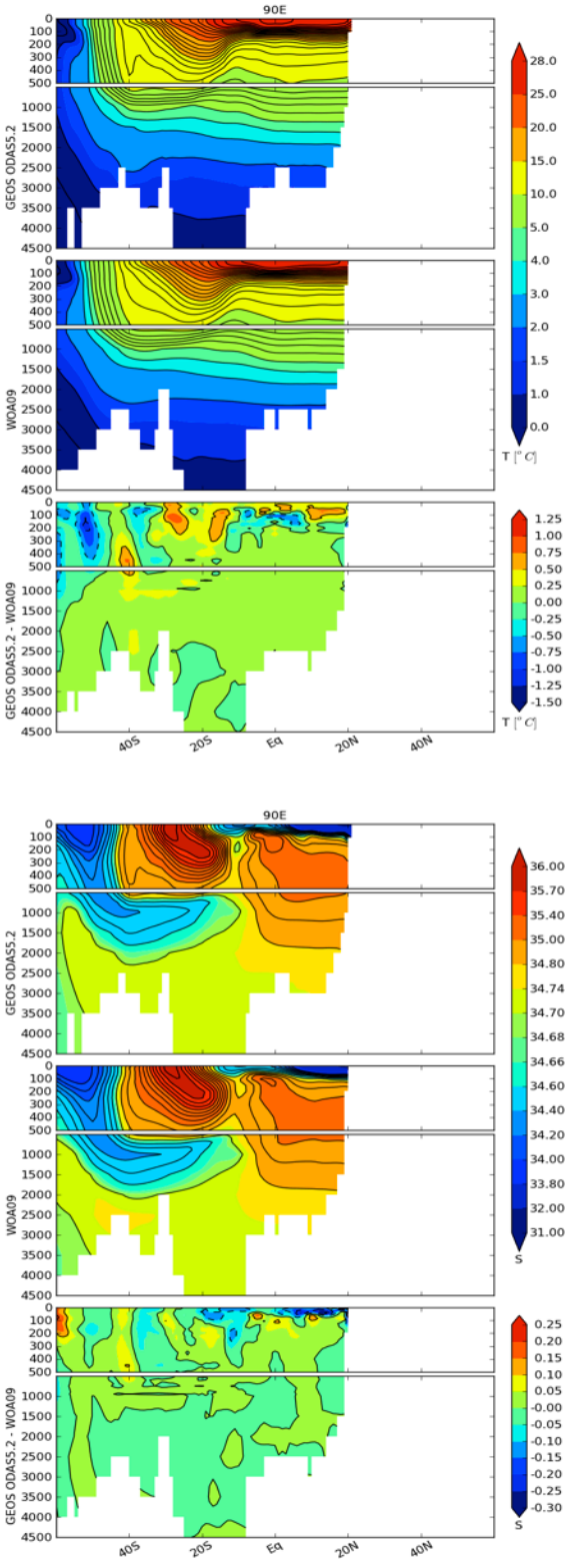

Figure 50: As for Figure 44, but for 90°E.

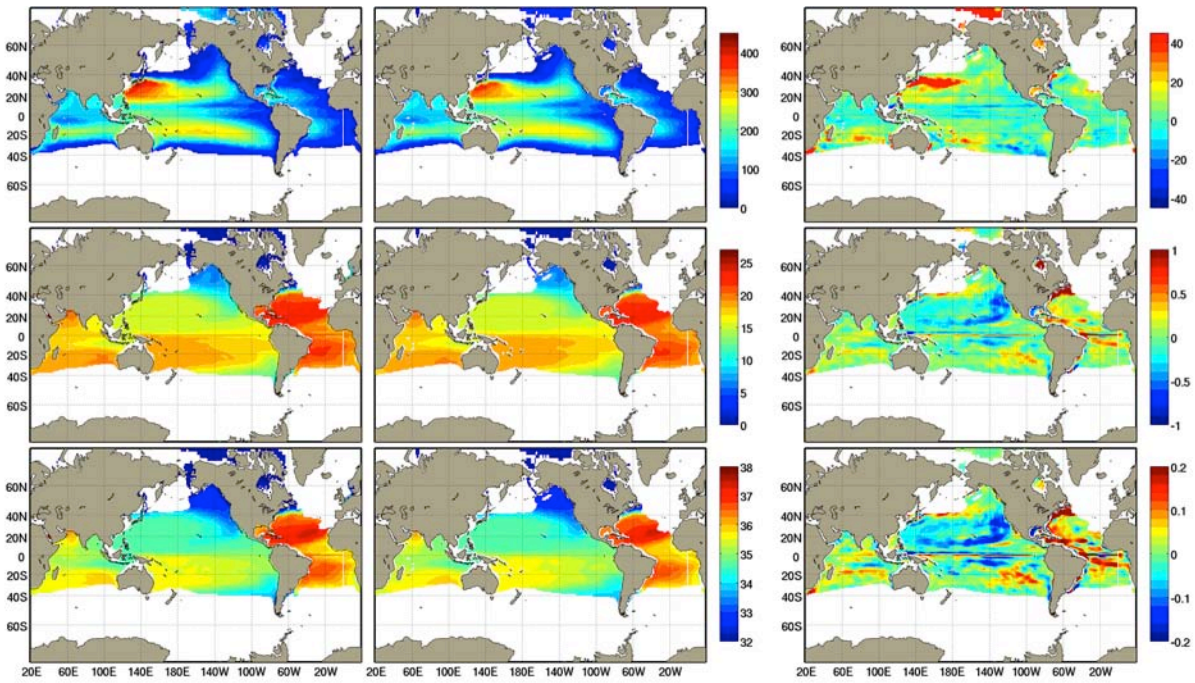

Figure 51: Depth of the σ_0=25.6 kg m^{-3} potential density surface (top row), temperature on that surface (middle row), and salinity (bottom row). The leftmost panel in each set is from the GEOS ODAS5.2 analysis; the center panel is from WOA09 and the rightmost panel shows the difference (ODAS minus WOA09).

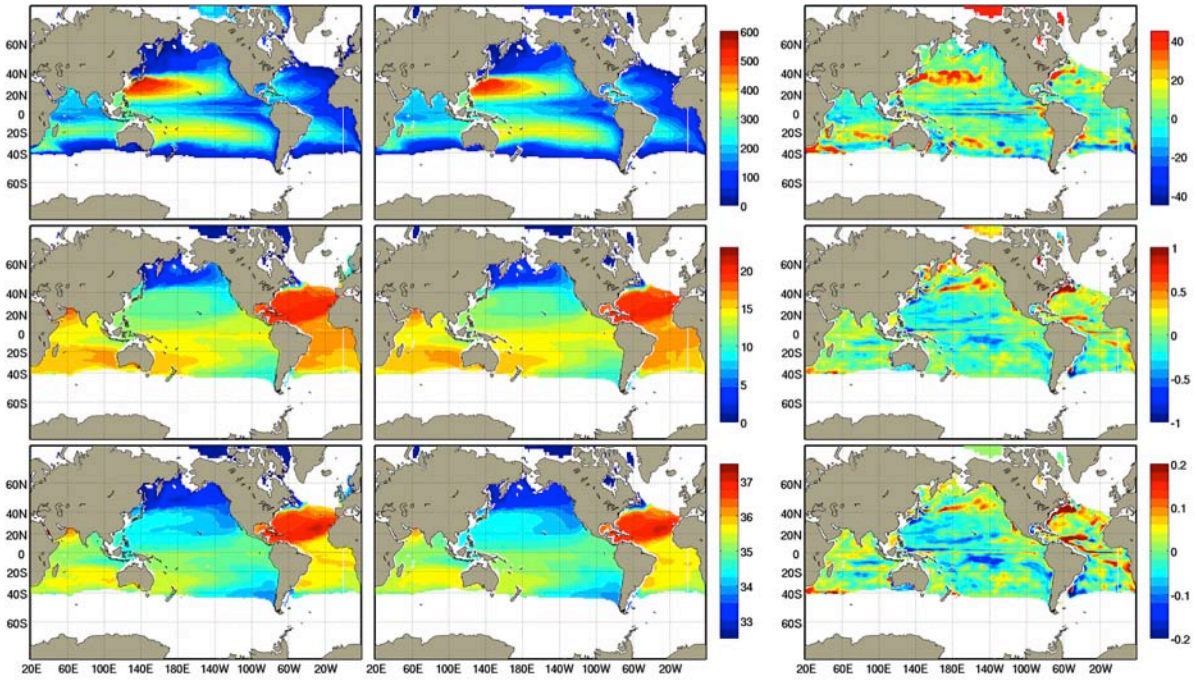

Figure 52: As for Figure 51, but for σ_0=26.2 kg m^{-3}.

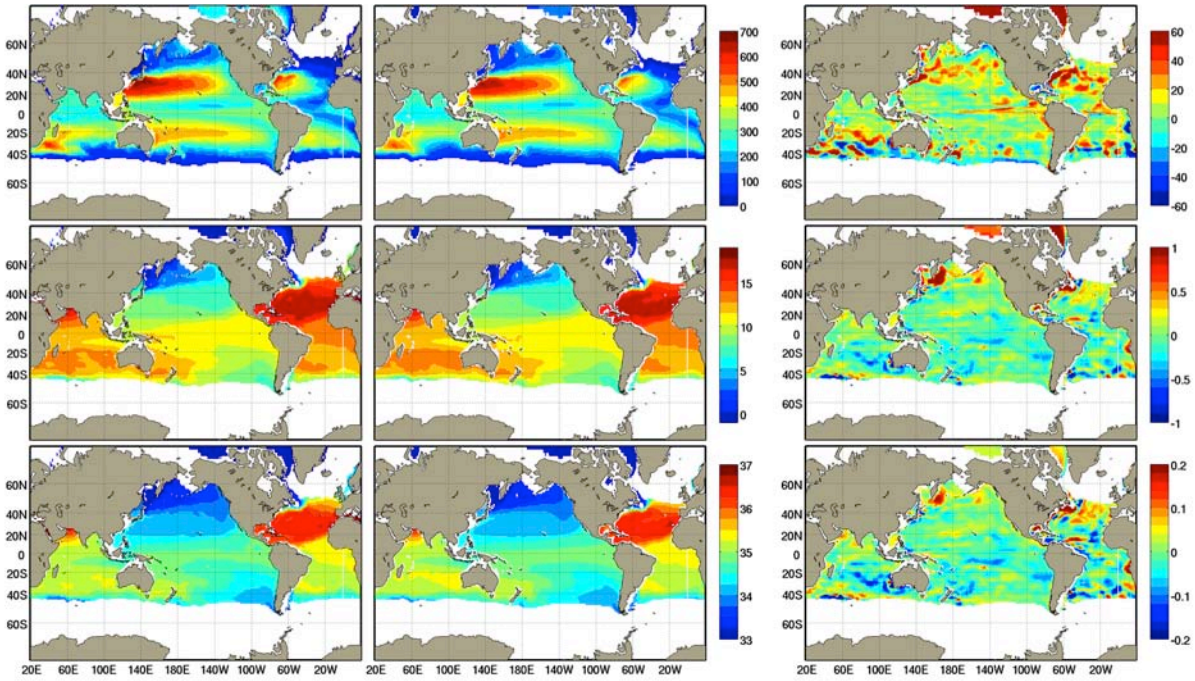

Figure 53: As for Figure 51, but for σ_0=26.6 kg m^{-3}.

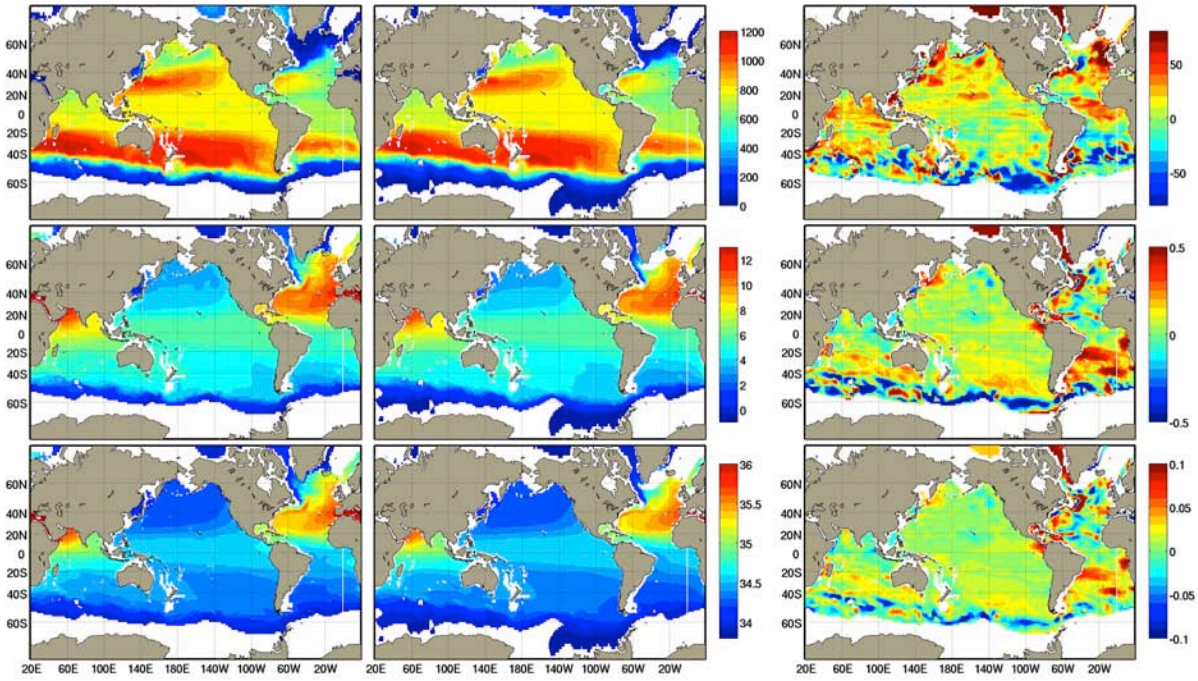

Figure 54: As for Figure 51, but for σ_0=27.25 kg m^{-3}.

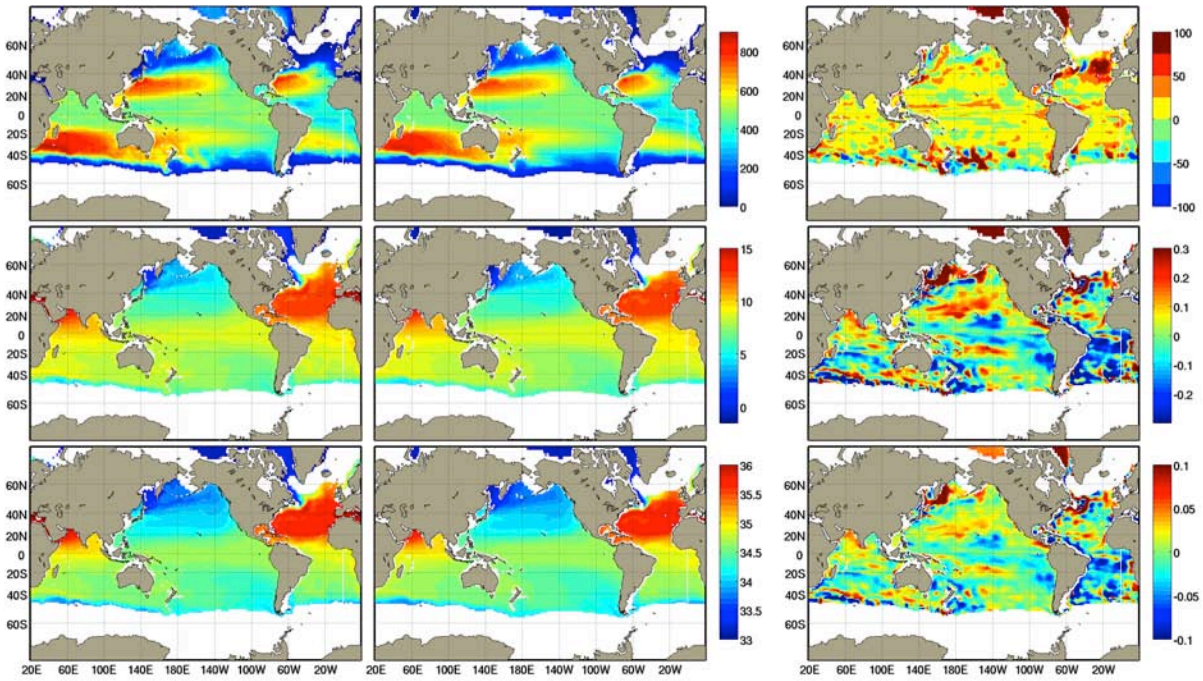

Figure 55: As for Figure 51, but for σ_1=31.398 kg m^{-3}.

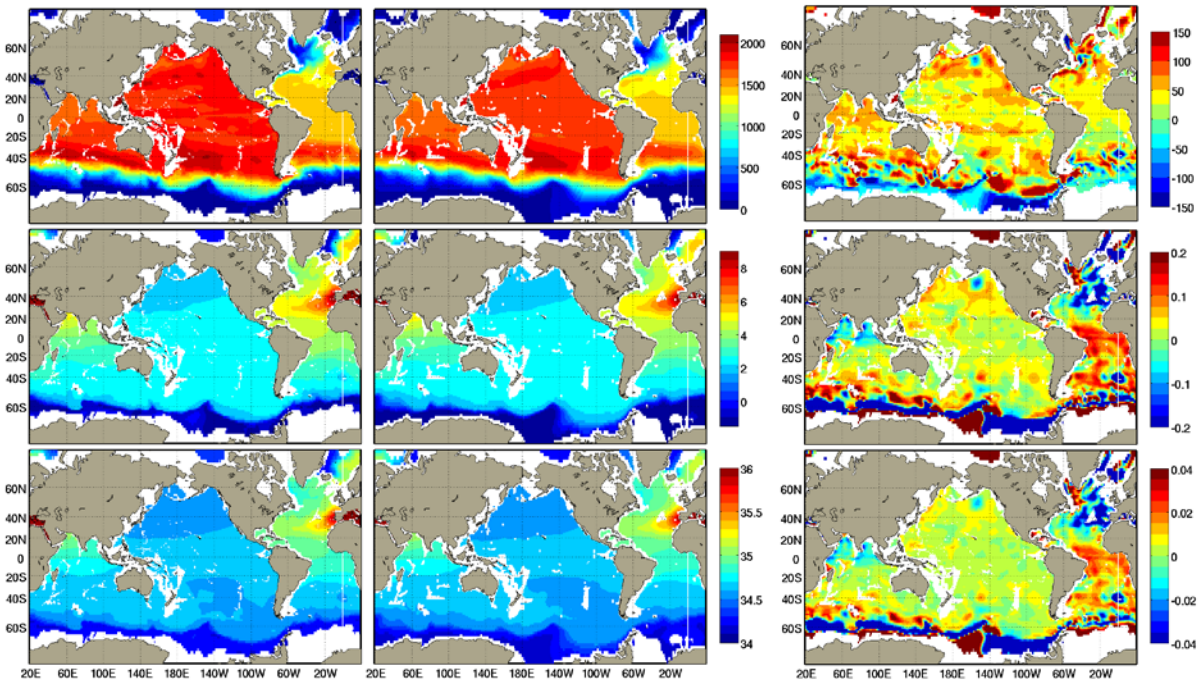

Figure 56: As for Figure 51, but for σ_1=32.274 kg m^{-3}.

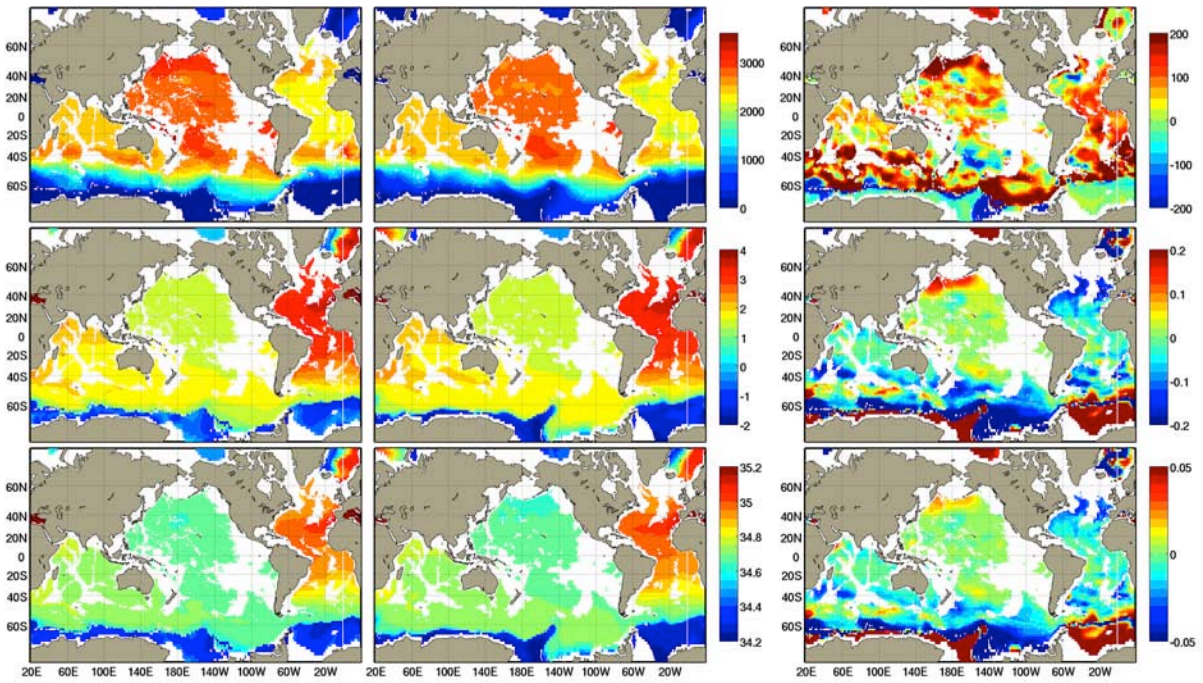

Figure 57: As for Figure 51, but for σ_2=36.98 kg m^{-3}.

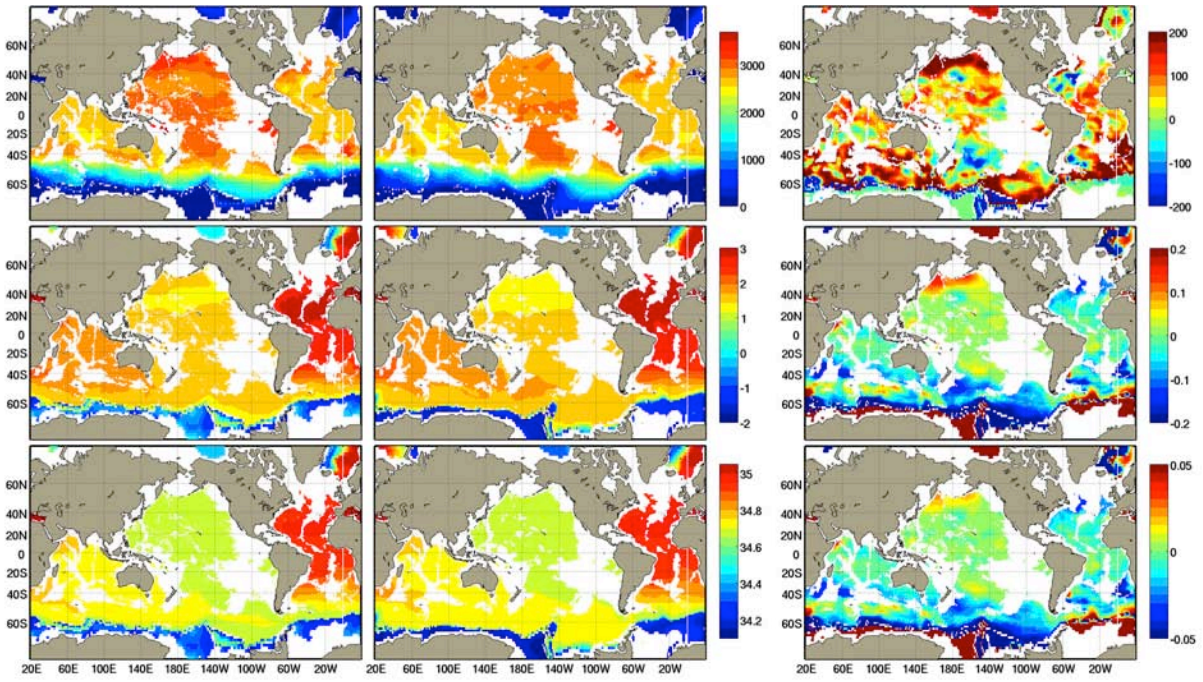

Figure 58: As for Figure 51, but for σ_2=41.44 kg m^{-3}.

Previous Volumes in This Series

Volume 1 *September 1994*	Documentation of the Goddard Earth Observing System (GEOS) general circulation model - Version 1 **L.L. Takacs, A. Molod, and T. Wang**
Volume 2 *October 1994*	Direct solution of the implicit formulation of fourth order horizontal diffusion for gridpoint models on the sphere **Y. Li, S. Moorthi, and J.R. Bates**
Volume 3 *December 1994*	An efficient thermal infrared radiation parameterization for use in general circulation models **M.-D. Chou and M.J. Suarez**
Volume 4 *January 1995*	Documentation of the Goddard Earth Observing System (GEOS) Data Assimilation System - Version 1 **James Pfaendtner, Stephen Bloom, David Lamich, Michael Seablom, Meta Sienkiewicz, James Stobie, and Arlindo da Silva**
Volume 5 *April 1995*	Documentation of the Aries-GEOS dynamical core: Version 2 **Max J. Suarez and Lawrence L. Takacs**
Volume 6 *April 1995*	A Multiyear Assimilation with the GEOS-1 System: Overview and Results **Siegfried Schubert, Chung-Kyu Park, Chung-Yu Wu, Wayne Higgins, Yelena Kondratyeva, Andrea Molod, Lawrence Takacs, Michael Seablom, and Richard Rood**
Volume 7 *September 1995*	Proceedings of the Workshop on the GEOS-1 Five-Year Assimilation **Siegfried D. Schubert and Richard B. Rood**
Volume 8 *March 1996*	Documentation of the Tangent Linear Model and Its Adjoint of the Adiabatic Version of the NASA GEOS-1 C-Grid GCM: Version 5.2 **Weiyu Yang and I. Michael Navon**
Volume 9 *March 1996*	Energy and Water Balance Calculations in the Mosaic LSM **Randal D. Koster and Max J. Suarez**
Volume 10 *April 1996*	Dynamical Aspects of Climate Simulations Using the GEOS General Circulation Model **Lawrence L. Takacs and Max J. Suarez**
Volume 11 *May 1997*	Documentation of the Tangent Linear and its Adjoint Models of the Relaxed Arakawa-Schubert Moisture Parameterization Package of the NASA GEOS-1 GCM (Version 5.2) **Weiyu Yang, I. Michael Navon, and Ricardo Todling**
Volume 12 *August 1997*	Comparison of Satellite Global Rainfall Algorithms **Alfred T.C. Chang and Long S. Chiu**
Volume 13 *December 1997*	Interannual Variability and Potential Predictability in Reanalysis Products **Wie Ming and Siegfried D. Schubert**
Volume 14 *August 1998*	A Comparison of GEOS Assimilated Data with FIFE Observations **Michael G. Bosilovich and Siegfried D. Schubert**
Volume 15	A Solar Radiation Parameterization for Atmospheric Studies

June 1999	**Ming-Dah Chou and Max J. Suarez**
Volume 16 *November 1999*	Filtering Techniques on a Stretched Grid General Circulation Model **Lawrence Takacs, William Sawyer, Max J. Suarez, and Michael S. Fox-Rabinowitz**
Volume 17 *July 2000*	Atlas of Seasonal Means Simulated by the NSIPP-1 Atmospheric GCM **Julio T. Bacmeister, Philip J. Pegion, Siegfried D. Schubert, and Max J. Suarez**
Volume 18 *December 2000*	An Assessment of the Predictability of Northern Winter Seasonal Means with the NSIPP1 AGCM **Philip J. Pegion, Siegfried D. Schubert, and Max J. Suarez**
Volume 19 *July 2001*	A Thermal Infrared Radiation Parameterization for Atmospheric Studies **Ming-Dah Chou, Max J. Suarez, Xin-Zhong, and Michael M.-H. Yan**
Volume 20 *August 2001*	The Climate of the FVCCM-3 Model **Yehui Chang, Siegfried D. Schubert, Shian-Jiann Lin, Sharon Nebuda, and Bo-Wen Shen**
Volume 21 *September 2001*	Design and Implementation of a Parallel Multivariate Ensemble Kalman Filter for the Poseidon Ocean General Circulation Model **Christian L. Keppenne and Michele M. Rienecker**
Volume 22 *August 2002*	Coupled Ocean-Atmosphere Radiative Model for Global Ocean Biogeochemical Models **Watson W. Gregg**
Volume 23 *November 2002*	Prospects for Improved Forecasts of Weather and Short-term Climate Variability on Subseasonal (2-Week to 2-Month) Time Scales **Siegfried D. Schubert, Randall Dole, Huang van den Dool, Max J. Suarez, and Duane Waliser**
Volume 24 *July 2003*	Temperature Data Assimilation with Salinity Corrections: Validation for the NSIPP Ocean Data Assimilation System in the Tropical Pacific Ocean, 1993–1998 **Alberto Troccoli, Michele M. Rienecker, Christian L. Keppenne, and Gregory C. Johnson**
Volume 25 *December 2003*	Modeling, Simulation, and Forecasting of Subseasonal Variability **Duane Waliser, Siegfried D. Schubert, Arun Kumar, Klaus Weickmann, and Randall Dole**
Volume 26 *April 2005*	Documentation and Validation of the Goddard Earth Observing System (GEOS) Data Assimilation System – Version 4 **Senior Authors: S. Bloom, A. da Silva and D. Dee** **Contributing Authors: M. Bosilovich, J-D. Chern, S. Pawson, S. Schubert, M. Sienkiewicz, I. Stajner, W-W. Tan, and M-L. Wu**
Volume 27 *December 2008*	The GEOS-5 Data Assimilation System - Documentation of Versions 5.0.1, 5.1.0, and 5.2.0. **M.M. Rienecker, M.J. Suarez, R. Todling, J. Bacmeister, L. Takacs, H.-C. Liu, W. Gu, M. Sienkiewicz, R.D. Koster, R. Gelaro, I. Stajner,**

and J.E. Nielsen

Volume 28
April 2012

The GEOS-5 Atmospheric General Circulation Model: Mean Climate and Development from MERRA to Fortuna
Andrea Molod, Lawrence Takacs, Max Suarez, Julio Bacmeister, In-Sun Song, and Andrew Eichmann

Volume 29
May 2012

Atmospheric Reanalyses – Recent Progress and Prospects for the Future. A Report from a Technical Workshop, April 2010
Michele M. Rienecker, Dick Dee, Jack Woollen, Gilbert P. Compo, Kazutoshi Onogi, Ron Gelaro, Michael G. Bosilovich, Arlindo da Silva, Steven Pawson, Siegfried Schubert, Max Suarez, Dale Barker, Hirotaka Kamahori, Robert Kistler, and Suranjana Saha